3-26-2015

Characterizing Multiple Wireless Sensor Networks for Large-Scale Radio Tomography

Tan Van

CHARACTERIZING MULTIPLE WIRELESS SENSOR NETWORKS FOR

LARGE-SCALE RADIO TOMOGRAPHY

THESIS

Tan Van, Captain, USAF

AFIT-ENG-MS-15-M-057

DEPARTMENT OF THE AIR FORCE
AIR UNIVERSITY

AIR FORCE INSTITUTE OF TECHNOLOGY

Wright-Patterson Air Force Base, Ohio

CHARACTERIZING MULTIPLE WIRELESS SENSOR NETWORKS FOR

LARGE-SCALE RADIO TOMOGRAPHY

THESIS

Presented to the Faculty

Department of Electrical and Computer Engineering

Graduate School of Engineering and Management

Air Force Institute of Technology

Air University

Air Education and Training Command

in Partial Fulfillment of the Requirements for the

Degree of Master of Science in Electrical Engineering

Tan Van, B.S.

Captain, USAF

March 2015

AFIT-ENG-MS-15-M-057

CHARACTERIZING MULTIPLE WIRELESS SENSOR NETWORKS FOR

LARGE-SCALE RADIO TOMOGRAPHY

THESIS

Tan Van, B.S.
Captain, USAF

Committee Membership:

Richard K. Martin, PhD
Chair

Colonel Matthew D. Sambora, PhD
Member

Jason R. Pennington, PhD
Member

AFIT-ENG-MS-15-M-057

Abstract

Radio Tomographic Imaging (RTI) is an emerging Device-Free Passive Localization (DFPL) technology that uses a collection of cheap wireless transceivers to form a Wireless Sensor Network (WSN). Unlike device-based active localization, DFPL does not require a target of interest to be wearing any kind of device. The basic concept of RTI utilizes the changes in Received Signal Strength (RSS) between the links of each transceiver to create an attenuation image of the area. This image can then be used for target detection, tracking, and localization. Each transceiver in the WSN must transmit sequentially to prevent collisions. This is not a problem when the number of transceivers in the WSN are small. However, large-scale RTI with a large number of transceivers suffer from high computational complexity, low frame rates, and physical distance limitations on the range of the transceivers.

The goal of this research is to determine the applicability and characterize the feasibility of using multiple WSNs to address the limitations with a large-scale RTI network. The concept to this new variant of RTI, called Multiple-Networks RTI (mnRTI), is to divide the transceivers into multiple WSNs as opposed to using one WSN. Analytical, simulated, and experimental data are computed, collected, and compared between a RTI network with one WSN to a mnRTI network with two WSNs. The WSN(s) comprise a total of 70 wireless transceivers covering an area of no more than 19 ft $\times$ 16 ft. Simulated and experimental results are presented from a series of stationary and moving target data collection. Preliminary results demonstrate multiple WSNs can potentially provide similar or better results than the traditional RTI method with one WSN. Multiple WSNs have higher frame rates and lower computational complexity. Also, position estimation accuracy are comparable, if not better, than the traditional RTI method with one WSN.

Acknowledgments

I want to thank my advisor, Dr. Richard K. Martin, for his guidance, support, and patience throughout these past 18 months. I also want to thank my committee members, Colonel Matthew Sambora and Dr. Jason Pennington, for their support and aid in helping me better understand the TelosB motes. Furthermore, I want to thank my family and friends for all their support. In particular, even though she abandoned us before the end, I want to thank Alyssa for her friendship and help throughout our coursework. I will never look at Einstein the same way again. I want to thank Ron for being so far ahead of his research that he had time to help me with my experiments. I also want to thank Thomas for helping me with my experiments. Finally, I want to thank Chris and Kate for making sure I was not homeless and did not starve to death while I was temporarily blind. Lastly, I want to thank the sponsors.

Tan Van

Table of Contents

List of Figures

List of Tables

List of Symbols

Symbol	Definition
$\mathbf{0}$	Vector or Matrix of Zeros
A	Area
α	Tunable Regularization Parameter
$\mathbf{C}$	Covariance Matrix
c	Speed of Light
ch	Channel
$\mathbf{D}$	Difference Operator Matrix
$\mathbf{D}_2$	Second-Order Difference Operator Matrix
Δ	Change or Difference
Δ_p	Pixel Length
δ_c	Correlation Parameter
d	Distance
ϵ	Euclidean Distance Error
F	Fading Loss Caused by Interference in a Multipath Environment
f	Frequency
f_c	Carrier Frequency
$\mathbf{G}$	Gaussian Kernel Filter

Symbol	Definition
$\mathbf{h}$	Histogram
K	Number of Wireless Transceivers
$\mathbf{K}$	Kernel Matrix
L	Static Losses
l	Link
$\boldsymbol{\Lambda}$	Diagonal Matrix
λ	Width of Weighting Ellipse
M	Number of Unique Two-way Links
m	Number of Channels
N	Number of Pixels
n	Noise
$\mathbf{n}$	Vector of Noise
O	Order of Magnitude
$\boldsymbol{\Omega}$	Signal Attenuation Weight Assigned to Pixel
P	Signal Power
p	Pixel
$\boldsymbol{\Pi}$	Linear Transformation Matrix
$\mathbf{Q}$	Tikhonov Regularization Matrix Operator

Symbol	Definition
R	Radius for Cylindrical Human Model
S	Shadowing Loss Due to Objects that Attenuate the Signal
$\mathbf{S}$	Binary Selection Matrix of Affected Pixels
σ^2	Variance
σ	Standard Deviation
SL	Segment Length
t	Time
θ	Diagonal elements of $\mathbf{\Lambda}$
$\mathbf{U}$	Unitary Matrix
V	Number of RSS Samples Within Time Period
$\mathbf{V}$	Unitary Matrix
w	Weight
$\mathbf{W}$	Weight Matrix of Pixel Signal Attenuation
$\hat{\mathbf{x}}$	Attenuation Image Estimate
x	Pixel Signal Attenuation
(x, y)	2-D Cartesian Coordinates
$\mathbf{x}$	Vector of Pixel Signal Attenuation
y	RSS Measurement

Symbol	Definition
y	Vector of RSS Link Measurements
z	Number of Wireless Sensor Networks
$\sum$	Sum
$(\bar{\bullet})$	Ensemble or Sample Mean of the Argument
$f(\bullet)$	Objective Cost Function of the Argument
$(\hat{\bullet})$	Estimate of the Argument
$\| \bullet \|$	Norm of the Argument
$Var(\bullet)$	Variance of the Argument
$(\bullet)^{-1}$	Matrix or Vector Inverse of the Argument
$(\bullet)^{T}$	Matrix or Vector Transpose of the Argument
$\mathcal{N}(\bullet, \bullet)$	*Gaussian Distribution*
I	Identity Vector or Matrix
$p_X(x)$	Probability Density/Mass Function
$p_Y(y\|x)$	Conditional Probability Density/Mass Function
$\sim$	Distributed As

Symbol	Definition
	Subscripts
$1s$	Pixel Solely Within Network 1
$2s$	Pixel Solely Within Network 2
c	Calibration
Cov	Covariance Matrix
dev	Device
e	Environment
f	Frame
F	Free Space Path Loss
$FOTIK$	First-Order Tikhonov Regularization
G	Gaussian Kernel Filter
H	Horizontal Direction
k	Pixel Within Both Networks
$KRTI$	Kernel Distance-Based RTI
l	Link
λ	Width of Ellipse
LBP	Linear Back Projection
LS	Least Squares Solution
lt	Long-Term
M	Number of Unique Links
m	Measurement
N	Number of Wireless Transceivers
n	Noise
nT	Not Human Target
p	Pixel

Symbol	Definition
pcenter	Center of Pixel *p*
r	Receiver
SOTIK	Second-Order Tikhonov Regularization
st	Short-Term
T	Truth Human Target
t	time
TIK	Tikhonov Regularization
tr	Transmitter
TSVD	Truncated Singular Value Decomposition
V	Vertical Direction
VRTI	Variance-Based RTI
w	Time Window
x	Pixel Signal Attenuation
z	WSN Number
zt	Total Number of Links or Pixels in *z* WSNs

Superscripts

Ellipse	Ellipse Model
Exp	Exponential Decay Model
InvArea	Inverse Area Model
Line	Line Model
NeSh	Network Shadowing Normalized Ellipse Model
NeShLine	Network Shadowing Line Model
T	matrix transpose
−1	matrix inverse

List of Acronyms

Acronym	Definition
1-D	One-Dimensional
3-D	Three-Dimensional
AFIT	Air Force Institute of Technology
AFRL	Air Force Research Laboratory
AWGN	Additive White Gaussian Noise
cdRTI	Channel Diversity RTI
dB	Decibels
dBm	Decibel Milliwatts
DFPL	Device-Free Passive Localization
dRTI	Directional RTI
FSPL	Free Space Path Loss
GHz	Gigahertz
GPS	Global Positioning System
GUI	Graphical User Interface
ICD	Informed Consent Document
IEEE	Institute of Electrical and Electronics Engineers
IID	Independent and Identically Distributed
Inc.	Incorporated
IR	Infrared
IRB	Institutional Review Board
kB	Kilobyte
kbps	Kilobits Per Second
KRTI	Kernel Distance-Based RTI

Acronym	Definition
LOS	Line-of-Sight
m	Meters
MHz	Megahertz
mnRTI	Multiple-Networks RTI
MSE	Mean Squared Error
NeSh	Network Shadowing
NLOS	Non-Line-of-Sight
PVC	Polyvinyl Chloride
PRR	Packet Reception Rate
PSNR	Peak Signal-to-Noise Ratio
RAM	Random Access Memory
RF	Radio Frequency
RFIC	Radio Frequency Integrated Circuit
RMSE	Root Mean Squared Error
RTI	Radio Tomographic Imaging
RSS	Received Signal Strength
SNR	Signal-to-Noise Ratio
SOCHE	Southwestern Ohio Council for Higher Education
SPAN	Sensing and Processing Across Networks
SVD	Singular Value Decomposition
TSVD	Truncated Singular Value Decomposition
USB	Universal Serial Bus
VRTI	Variance-Based RTI
WPAN	Wireless Personal Area Network
WSN	Wireless Sensor Network

CHARACTERIZING MULTIPLE WIRELESS SENSOR NETWORKS FOR

LARGE-SCALE RADIO TOMOGRAPHY

I.   Introduction

THIS chapter presents a brief introduction to Wireless Sensor Networks (WSNs) and Radio Tomographic Imaging (RTI). It discusses the potential applications of RTI, as well as a limitation which this research attempts to solve. This chapter also defines the research goal and outlines the structure of this document.

1.1   Research Motivation and Background

As technology continues to advance in creating cheap wireless communication devices, there is a growing interest in using WSNs for various applications. A WSN is a collection of sensors populated over an area, each with a radio transceiver capable of transmitting and receiving information with other transceivers over a wireless frequency. A base station transceiver collects the information and processes the information into something useful [1].

Most position tracking research has been focused on device-based active localization, where a target is carrying an active transmitter of some sort [2]. However, there is an emerging interest in a different concept called Device-Free Passive Localization (DFPL) [3]. Unlike device-based active localization, DFPL does not require a target of interest to be wearing any kind of device. The concept of DFPL uses the fact that changes in the environment affects Radio Frequency (RF) signals in a wireless network, and these changes can be used for tracking and localization [3]. DFPL has significant benefits, especially in situations where an individual may be uncomfortable or does not wish to wear a device.

RTI is an emerging DFPL technology that uses a collection of cheap wireless transceivers to form a WSN. The WSN is then used to detect and track objects of interest within the network [4], [5], [6]. At any given time, a transceiver transmits a RF signal. All other transceivers within the network are listening, storing the resultant Received Signal Strength (RSS), and associating this value to the communication link with the transmitting transceiver. Each synchronized transceiver transmits in sequential order to prevent another transceiver from reading the wrong RSS. There is a unique communication link between each pair of transceivers within the WSN. This communication link can be either Line-of-Sight (LOS) or Non-Line-of-Sight (NLOS), passing through walls, furniture, or most other obstructions in between the two links [4]. A base station transceiver is connected to a processing computer to collect the RSS of each unique communication link within the WSN. The area within the network is divided into a grid of multiple sections, or pixels. The size of each pixel is defined by the user. A weighting matrix determines how much weight the RSS on a link affects each pixel within the area. This matrix can be divided into two parts, a selection matrix and a scalar magnitude matrix [7]. The selection matrix determines which pixels are affected by a particular link. The scalar magnitude matrix defines a scalar value to apply to each pixel for that particular link. Whenever a person or object moves in between two transceivers, they interfere and attenuate the RSS of that link. The basic concept of RTI is to use the changes in attenuation from the communication links between transceivers within a WSN to create an image of attenuation changes of the network area.

There are numerous benefits with RTI. Since RTI is a form of DFPL, any person or object moving through the network is not required to wear any kind of active device or even actively participate [8]. Also, RF signals can pass through obstructions, such as walls and smoke, where other technology like Infrared (IR) or optical cameras cannot [4]. Technologies like Global Positioning System (GPS) also use RF signals, but require the

target to have an active device [3]. Another benefit with RTI is that it can potentially operate over almost any kind of weather or lighting conditions, whereas technology like an optical camera system requires a well-lit environment. There is also less of a privacy concern with RTI since an attenuation image does not provide any personal identifiable information about the person or object that is interfering with the RSS [4].

One potential application with RTI is for residential monitoring in elderly care and assisted-living homes. By monitoring the movement and position patterns of a patient, healthcare officials can recognize physical and mental health conditions when patients do something out of the norm [9]. RTI can also potentially detect when a person has fallen, alerting medical officials without the victim having to actively request for help [10]. RTI can also potentially detect and track the breathing rate of a person, whether for security, health care, or search and rescue [11]. Smart homes can also benefit from RTI. By knowing which rooms are currently being occupied, lighting and climate control can autonomously be adjusted to meet the needs of the resident [12]. Finally, RTI can also be applied to security and emergency situations. RTI can be deployed for roadside surveillance, either for border control or at restricted areas where security officials can determine a potential threat while at a safe stand-off distance [5]. For a hostage or terrorist situation where special operation forces have to enter a hostile building, RTI can be a quick and cheap method for security officials to deploy and determine the location of potential hostiles prior to entering the building [13].

However, there are a few limitations to the current RTI method. Most research with RTI uses transceivers that must transmit their signal sequentially to prevent collisions [4]. This is not a problem when the number of transceivers in the WSN is fairly small. However, for a large-scale WSN with a substantial number of transceivers, it may take too long for all transceivers to transmit a signal and obtain one image frame for real-time applications. Also, the computational complexity in converting the RSS to an attenuation

3

image is dependent on the number of unique links between all transceivers in the network and the number of pixels within the image. The number of unique links within a network increases quadratically with the number of transceivers [4]. Limited memory space on the hardware of the transceivers and finite memory space on a processing computer become a problem for a network with too many transceivers. Transceivers also have limited power, so there is a physical limit on how far apart transceivers can be placed from one another before the transmitted RF signal becomes too noisy or weak that another transceiver will not be able to read the RSS accurately.

For example, if RTI is utilized for intrusion detection of a hangar bay, hundreds of transceivers may be required to adequately cover the entire bay. There are a few limitations that the traditional RTI method with one WSN may run into. The number of transceivers required to cover the entire area may be too large for the available memory space on the transceivers. The matrix and calculations required to produce an estimated attenuation image may also be too large for a regular processing computer to handle. Finally, the transmission range of the transceiver may not be far enough to reach the other end of the hangar bay. The same limitations can occur if RTI is used for a long narrow pathway, such as a restricted road, a tunnel, or a hallway. The width of the pathway is short, but the length may be longer than the maximum transmission range of the transceivers.

In summary, there are three main potential limitations to a large-scale RTI network.

1. Frame Rate: The more transceivers there are in a WSN, the longer it will take to obtain one frame of data, leading to attenuation images that are less accurate and updated less frequently.

2. Finite Memory and Computational Complexity: As the number of K transceivers increases, the number of unique links increases quadratically and the computational complexity can increase by $O(K^6)$ [14]. Finite memory space on the transceivers

and processing computer become a limitation when the number of transceivers is too great.

3. Transmission Range: All transceivers have a limited transmission range, depending on their power and type of environment. The largest RTI area possible is defined by the maximum transmission range for the transceivers furthest away from each other.

1.2 Research Goal

The goal of this research is to determine the applicability and characterize the capabilities of using multiple WSNs to address the three main limitations with a large-scale RTI network. The concept to this new variant of RTI, called Multiple-Networks RTI (mnRTI), is to divide the transceivers into multiple WSNs as opposed to using the traditional one WSN. There are numerous potential benefits of using multiple WSNs as opposed to one. Dividing the number of transceivers will decrease the time required for all transceivers to transmit their RF signal since each network can operate in parallel, as long as each network operate under different frequencies. This will decrease the time required to generate an image frame and increase the frame rate. Less transceivers per network will also decrease the computational complexity since there are less unique communication links. However, less unique links between transceivers result in less information available to create an accurate attenuation image. A poor attenuation image quality may make the RTI process useless. Finally, dividing a wide area into multiple sections will make the area of each individual network smaller, allowing for transceivers to be placed further apart. This opens the possibility for a bigger total coverage area than the traditional one WSN.

1.3 Thesis Organization

The remainder of this thesis is organized as follows. Chapter II presents background information and research related to the field of RTI. The general concept and system model

for RTI is discussed, along with various methods that have been suggested in literature to improve the accuracy and image quality of the attenuation images.

Chapter III discusses the methodology and tools used to characterize the capabilities of using multiple WSNs for RTI. First, the RTI parameters and assumptions made in this research are stated. Frame rate, computational complexity, and image quality are the three metrics used to characterize the quality of each network. Image quality is examined objectively by comparing the Signal-to-Noise Ratio (SNR) and accuracy of position estimates of each network. An analytical section then looks at the theoretical comparison between a network with one WSN and a network with multiple WSNs. Afterwards, the process for generating simulations in MATLAB$^{®}$ is discussed, followed by methods for conducting experiments in a lab environment at the Air Force Institute of Technology (AFIT).

Chapter IV presents the simulated and experimental results from following the methodology discussed in Chapter III. The results of a stationary target and moving target within one or two WSNs are presented as a function of the pattern they move within the network and the speed at which they move throughout the network. Network configurations with two WSNs are compared with each other and to a network configuration using the traditional one WSN.

Finally, Chapter V summarizes the results and provides a conclusion to the capabilities of using multiple WSNs for RTI. Potential areas for future research are also suggested.

II.   Related Work

THIS chapter presents background information and research related to RTI. Section 2.1 first introduces the history and concept of DFPL. Section 2.2 presents the concept and system model of RTI. Section 2.3 discusses the various methods of interpreting RSS data from the transceivers throughout the network. Then, Section 2.4 presents a few weight matrix models that map RSS from each link to a pixel within the attenuation image that have been suggested in the literature. Section 2.5 presents different noise models that have been suggested for RTI. Afterwards, Section 2.6 discusses the actual process of converting RSS data to an attenuation image and Section 2.7 discusses different regularization techniques proposed in the literature to apply to the image reconstruction process. Section 2.8 presents different variations of RTI that have been suggested in the literature. Finally, Section 2.9 presents a model to simulate truth data for a target.

2.1   Device Free Localization

Woyach, Puccinelli, and Haenggi first introduced the idea of using a wireless network as transceivers to detect motion without the target carrying any kind of active device in [8]. Shadowing and fading effects experienced from the transceivers are used to detect motion and estimate velocities. Then, research in [15] expanded on this concept by using RF signals in a WSN to track position. Youssef, Mah, and Agrawala then introduced the terminology of DFPL in [3]. DFPL uses the concept that signals in a wireless network are affected by the changes in the environment. These changes are used to detect the presence of an object or obstruction.

DFPL has significant benefits. Unlike device-based active localization, DFPL does not require the target of interest to be wearing any kind of device [3]. This is critical in situations where an individual may be uncomfortable or unwilling to wear a device. Also,

for situations like intrusion detection, it is unreasonable to expect an intruder or hostile to wear any kind of tracking device. Other tracking systems such as video, infrared, pressure, and ultrasound, do exist and are widely used [15]. However, they typically have a large footprint, a high cost of installation, infrastructure, and maintenance, or have environmental requirements such as lighting. DFPL is relatively inexpensive and can leverage preexisting wireless networks. Advances in Radio Frequency Integrated Circuits (RFICs) have also resulted in the ability to manufacture low-cost and portable wireless transceivers [4].

However, there are disadvantages to DFPL as well. RF signals are typically subjected to a strong multipath environment for indoor scenarios [16]. RF signals diffract, reflect, attenuate, and scatter as they pass through the environment. This multipath environment can create very noisy signals that any type of tracking or localization method must account for in its algorithm [3].

2.2   Received Signal Strength Tomography

RTI is an emerging DFPL technology that uses a collection of cheap wireless transceivers to form a WSN [4]. Each transceiver is capable of transmitting and receiving RSS from each other. As a target of interest walks through this network area, it obstructs the links between transceivers. The RSS of the links attenuate and experience a shadow loss. The basic concept of RTI uses the changes in attenuation between these links to create an attenuation image map of the area. This image can then be applied to target localization and track movement.

Wilson and Patwari laid the foundation for setting up a system model for RTI in [4]. There are K wireless transceivers surrounding a particular area to form a WSN. This area is divided into N number of pixels of size $\Delta_p \times \Delta_p$. For K number of transceivers, there are $M = \frac{K(K-1)}{2}$ unique two-way links. Fig. 2.1 shows an example of all the unique two-way links for a given number of transceivers. Each transceiver transmits a RF signal that passes through the physical environment of the network, absorbing, diffracting, reflecting, and

8
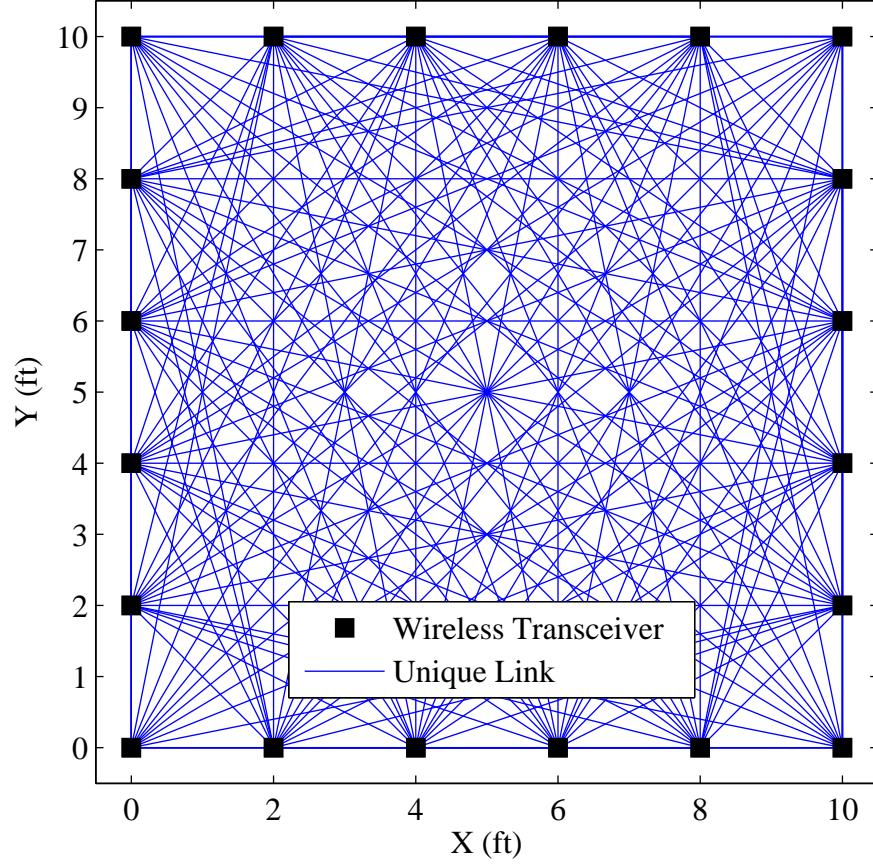
Figure 2.1: Example of unique links within a RTI network with 20 wireless transceivers [4].

scattering some of the transmitted signal. Other transceivers around the network collects the resultant signal strength after it has passed through obstructions from the environment in and around the network.

The RSS in Decibels (dB) on any particular link, l, at a specific time, t, can be modeled as [4]

$$y_l(t) = P_{tr} - L_{F,l} - L_{dev,l} - S_l(t) - F_l(t) - n_{tr,l}(t) - n_{r,l}(t) - n_{e,l}(t) - n_{m,l}(t), \qquad (2.1)$$

where [4]

- P_{tr}: transmitted power,
- $L_{F,l}$: static losses due to distance, also referred to as Free Space Path Loss (FSPL) [17],
- $L_{dev,l}$: static losses from hardware inconsistencies, antenna patterns, etc.,
- $S_l(t)$: shadowing loss from obstructions attenuating the signal,
- $F_l(t)$: fading loss caused by interference (constructive and destructive) in a multipath environment,
- $n_{tr,l}(t)$: noise created by the transmitter,
- $n_{r,l}(t)$: noise created by the receiver,
- $n_{e,l}(t)$: noise created by the environment,
- $n_{m,l}(t)$: measurement noise.

The equation for FSPL for link l between two transceivers at a distance d apart is [17], [18]

$$\bar{L}_{F,l} = \left(\frac{4\pi d f}{c} \right)^2, \tag{2.2}$$

where d is the distance between the transmitter and receiver, f is the operating frequency of the transceivers, and c is the speed of light. RSS is normally measured in dB [19], [20], or $10 \log 10$ of the power. Therefore, (2.2) is rewritten in dB as

$$
\begin{aligned}
L_{F,l} &= 10 \log_{10} \left(\frac{4\pi d f}{c} \right)^2, \\
&= 2 \cdot 10 \log_{10} \left(\frac{4\pi d f}{c} \right), \\
&= 20 \log_{10}(d) + 20 \log_{10}(f) + 20 \log_{10} \left(\frac{4\pi}{c} \right). \tag{2.3}
\end{aligned}
$$

Equation (2.1) is rewritten as

$$y_l(t, d, f) = P_{tr} - L_{F,l}(d, f) - L_{dev,l} - S_l(t) - F_l(t) - n_{tr,l}(t) - n_{r,l}(t) - n_{e,l}(t) - n_{m,l}(t). \tag{2.4}$$

2.3 Measurement Models

2.3.1 Shadowing-Based RSS.

One of the most common measurement technique in RTI is to use a linear system model and look at only the changes in attenuation at a particular time compared to a baseline calibration time [4]. This measurement method is called shadowing-based RTI.

A baseline calibration is defined as a set of RSS data collected within the WSN without any targets present [4]. This may include any static objects (furniture, trees, walls, etc.) that is typical to the environment. Calibration data consists of collecting RSS for a period of time to obtain a baseline average RSS for each link. Let $\mathbf{y}_c \in \mathcal{R}^{M \times 1}$ be the vector of calibration RSS data. This calibration data provides a baseline set of RSS within an environment free of any targets of interest.

By measuring the change in RSS, all static variables cancel out, greatly simplifying the problem. Let Δy_l be the change in RSS for a particular time, t, against the baseline calibration time, t_c. Finding Δy_l using (2.4) yields [4]

$$\Delta y_l = y_{l,t_c} - y_{l,t}, \tag{2.5}$$

$$\begin{aligned} = S_l(t) - S_l(t_c) + F_l(t) - F_l(t_c) + n_{tr,l}(t) - n_{tr,l}(t_c) + n_{r,l}(t) - n_{r,l}(t_c) \\ + n_{e,l}(t) - n_{e,l}(t_c) + n_{m,l}(t) - n_{m,l}(t_c). \end{aligned} \tag{2.6}$$

Since RTI utilizes the shadowing loss from RSS to create an attenuation image of the area, fading loss, noise created from the transmitter, noise created from the receiver, noise created by the environment, and measurement noise can all be grouped together as

$$n_l(t) = F_l(t) - F_l(t_c) + n_{tr,l}(t) - n_{tr,l}(t_c) + n_{r,l}(t) - n_{r,l}(t_c) + n_{e,l}(t) - n_{e,l}(t_c) + n_{m,l}(t) - n_{m,l}(t_c). \tag{2.7}$$

Equation (2.6) is updated to

$$\Delta y_l = S_l(t) - S_l(t_c) + n_l(t). \tag{2.8}$$

Let $\mathbf{x} \in \mathcal{R}^{N \times 1}$ be the vector of pixels within an area. A weight matrix converts the changes in RSS between each transceiver to changes in attenuation per pixel. Let

11

$\mathbf{W} \in \mathcal{R}^{M \times N}$ be the weight matrix that defines the relationship on how much each pixel is affected by a particular link. Shadowing loss can be written as approximately the sum in RSS experienced at each pixel, p, [4]

$$S_l(t) = \sum_{p=1}^{N} w_{l,p} x_p(t), \tag{2.9}$$

where $w_{l,p}$ is the weight on pixel p affected by link l and $x_p(t)$ is the attenuation on pixel p at time t. Applying (2.9) to (2.8) yields

$$\Delta y_l = \sum_{p=1}^{N} w_{l,p} x_p(t) - \sum_{p=1}^{N} w_{l,p} x_p(t_c) + n_l(t), \tag{2.10}$$

$$= \sum_{p=1}^{N} w_{l,p} \Delta x_p + n_l(t), \tag{2.11}$$

where $\Delta x_p \in \mathcal{R}^{N \times 1}$ is the vector of changes in attenuation at each pixel between the current time, t, and calibration time, t_c.

Finally, the system model for RTI is written in matrix form as [4], [16], [21]

$$\mathbf{y} = \mathbf{W}\mathbf{x} + \mathbf{n}, \tag{2.12}$$

where

$$\begin{aligned}
\mathbf{y} &= [\Delta y_1, \Delta y_2, \cdots, \Delta y_M]^T, \\
[\mathbf{W}]_{l,p} &= w_{l,p}, \\
\mathbf{x} &= [\Delta x_1, \Delta x_2, \cdots, \Delta x_N]^T, \\
\mathbf{n} &= [n_1, n_2, \cdots, n_M]^T.
\end{aligned} \tag{2.13}$$

2.3.2 Variance-Based RSS.

Instead of measuring the change in RSS between a baseline calibration period and current RSS, [22] suggested taking the variance in RSS as a more accurate approach for through-wall and NLOS RTI scenarios. In a strong multipath environment without LOS transceivers, a target does not have as profound of an effect on obstructing a link as with

LOS transceivers. The variance in RSS increases, even though the mean RSS does not change much [23]. As opposed to taking the change in RSS in (2.8), Variance-Based RTI (VRTI) takes the variance in RSS over a discretized time window period with V samples as [24]

$$y_l = \frac{1}{V-1} \sum_{w=0}^{V-1} (\bar{y}_l[t] - y_l[t-w])^2,$$ (2.14)

$$\bar{y}_l[t] = \frac{1}{V} \sum_{w=0}^{V-1} y_l[t-w].$$ (2.15)

The vector of RSS links, $\mathbf{y}$, in (2.13) is updated to

$$\mathbf{y}_{VRTI} = [y_1, y_2, \cdots, y_M]^T.$$ (2.16)

The experiments in [22] showed VRTI was capable of identifying areas of motion in through-wall scenarios where shadowing-based RTI was not as effective. VRTI also does not require a calibration time to collect RSS without any targets of interest in the network, making it more applicable for real-world situations. The limitation with VRTI, however, is that it is less accurate for targets with little or no motion.

2.3.3 Kernel Distance RSS.

Another measurement model in [23], called Kernel Distance-Based RTI (KRTI), suggested a hybrid of shadowing-based RTI and VRTI by taking the histogram of RSS for each link. KRTI takes a long-term histogram, $\mathbf{h}_{lt}$, and short-term histogram, $\mathbf{h}_{st}$, of RSS values to determine which links have been obstructed by a target. The histograms are a collection of RSS values for a certain period of time with a user-defined weight indicating the length of the time window to store previous RSS values. The kernel difference between the two histograms for link l is calculated using the equation [23]

$$\Delta(\mathbf{h}_{l,st}, \mathbf{h}_{l,lt}) = \mathbf{h}_{l,st}^T \mathbf{K} \mathbf{h}_{l,st} + \mathbf{h}_{l,lt}^T \mathbf{K} \mathbf{h}_{l,lt} - 2\mathbf{h}_{l,st}^T \mathbf{K} \mathbf{h}_{l,lt},$$ (2.17)

13

where $\mathbf{K}$ is a Gaussian or Epanechnikov kernel matrix. The vector of RSS links $\mathbf{y}$ in (2.13) is updated to

$$\mathbf{y}_{KRTI} = \left[\Delta(\mathbf{h}_{1,st}, \mathbf{h}_{1,lt}), \Delta(\mathbf{h}_{2,st}, \mathbf{h}_{2,lt}), \cdots, \Delta(\mathbf{h}_{M,st}, \mathbf{h}_{M,lt})\right]^T. \qquad (2.18)$$

The experiments in [23] showed that KRTI was able to effectively detect both stationary and moving targets without the need of an offline calibration time period, making it more robust than shadowing-based RTI and VRTI. The limitation with KRTI is that a stationary target will eventually fade away if it stays in one position for longer than the long-term histogram.

2.4   Weight Models

The weight matrix, $\mathbf{W}$, can be broken down into two parts as [5], [7]

$$\mathbf{W} = \boldsymbol{\Omega} \odot \mathbf{S}, \qquad (2.19)$$

where $\boldsymbol{\Omega}$ is a matrix of scalar magnitudes indicating how much weight a link affects each pixel, $\odot$ is the element-wise Hadamard multiplication, and $\mathbf{S}$ is a binary selection matrix to determine which pixels are affected by a particular link [7]. There are a number of proposed weight models to determine how much weight a link has on each pixel in the literature. The remainder of this section describes a few of them.

2.4.1   NeSh Normalized Ellipse Model.

The Network Shadowing (NeSh) Normalized Ellipse model was the initial weight model suggested for RTI in [4] and is currently the most commonly used weight model in the literature. It was used in [4], [9], [16], [21], [22], [23], [25], [26], [27], [28]. The NeSh model suggests that the weight from a link to a pixel is inversely proportional to the square root of the distance between the link. The shorter the link, the more accurate the data is and the more weight applies to each affected pixel. The NeSh model uses a magnitude matrix, $\boldsymbol{\Omega}^{NeSh}$, of [7]

$$\boldsymbol{\Omega}_{l,p}^{NeSh} = \frac{1}{\sqrt{d_l}}, \qquad (2.20)$$

14

where d_l is the distance between the two transceivers for link l. The selection matrix, $\mathbf{S}^{Ellipse}$, uses an ellipse with a foci around each transceiver to determine which pixels are selected [4]. This model suggests that pixels on and close to the path of a link are affected by the changes in attenuation experienced by that link. $\mathbf{S}^{Ellipse}$ can mathematically be shown as [7]

$$\mathbf{S}_{l,p}^{Ellipse} = \begin{cases} 1, & \text{if } d_{l,pcenter}(1) + d_{l,pcenter}(2) < d_l + \lambda \\ 0, & \text{otherwise} \end{cases}, \qquad (2.21)$$

where $d_{l,pcenter}$ is the distance between the transceiver and the center of pixel p and λ is a tunable parameter that defines the width of the ellipse. Fig. 2.2 shows an example of the pixels selected according to the $\mathbf{S}^{Ellipse}$ selection matrix for a particular ellipse width [4]. The final equation for the NeSh model is represented as [4]

$$\mathbf{W}_{l,p}^{NeSh} = \frac{1}{\sqrt{d_l}} \begin{cases} 1, & \text{if } d_{l,pcenter}(1) + d_{l,pcenter}(2) < d_l + \lambda \\ 0, & \text{otherwise} \end{cases}. \qquad (2.22)$$

2.4.2   Line Model.

The Line model was another weight model discussed and used in [5], [6], [29]. This model is computationally cheap to implement [5]. The Line model suggests the weight from a link to a pixel is the segment length of the link that passes through the pixel. To determine which pixels are affected, this model suggests that only the pixels that the link actually traverses through are affected by the link. This model has a magnitude matrix, $\mathbf{\Omega}^{Line}$, of [6]

$$\mathbf{\Omega}_{l,p}^{Line} = S L_{l,p}, \qquad (2.23)$$
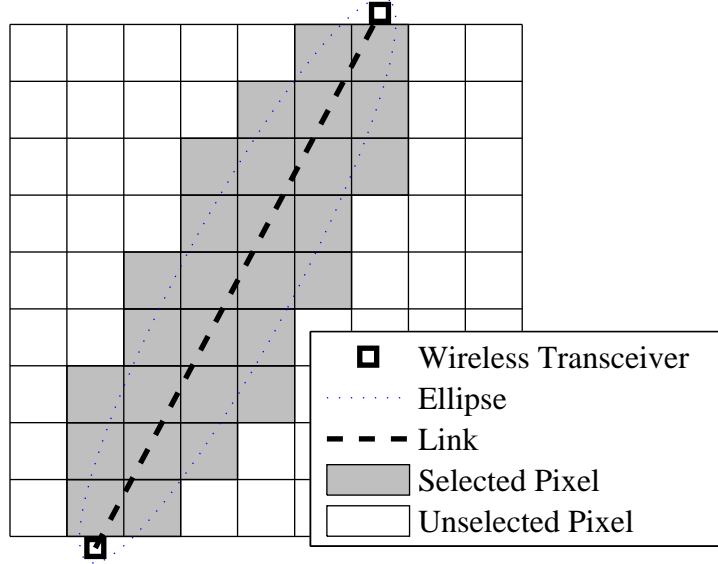
Figure 2.2: Example of pixels selected for a particular link between two transceivers for the $\mathbf{S}^{Ellipse}$ selection matrix [4].

where $SL_{l,p}$ is the segment length of the link l that traverses through pixel p. The selection matrix, $\mathbf{S}^{Line}$, for this model is [6]

$$\mathbf{S}^{Line}_{l,p} = \begin{cases} 1, & \text{if link } l \text{ traverses through pixel } p \\ 0, & \text{otherwise} \end{cases}. \qquad (2.24)$$

Fig. 2.3 shows an example of the pixels selected according to the $\mathbf{S}^{Line}$ selection matrix. The final equation for the Line model is represented as

$$\mathbf{W}^{Line}_{l,p} = SL_{l,p} \begin{cases} 1, & \text{if link } l \text{ traverses through pixel } p \\ 0, & \text{otherwise} \end{cases}. \qquad (2.25)$$

2.4.3 NeSh Line Model.

The NeSh Line model is a hybrid of the two weight models mentioned in Section 2.4.1 and Section 2.4.2, using a mix of the two magnitude matrices and the line selection matrix,

16
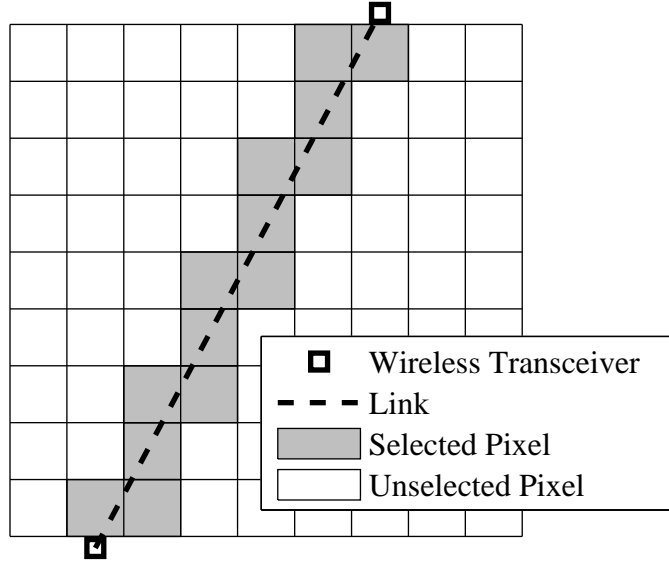
Figure 2.3: Example of pixels selected for a particular link between two nodes for the $\mathbf{S}^{Line}$ selection matrix [4].

$\mathbf{S}^{Line}$. This model was used in [30], [31] and is represented as

$$\mathbf{W}_{l,p}^{NeShLine} = \frac{SL_{l,p}}{\sqrt{d_l}} \begin{cases} 1, & \text{if link } l \text{ traverses through pixel } p \\ 0, & \text{otherwise} \end{cases}. \qquad (2.26)$$

2.4.4 Exponential Decay Model.

The Exponential Decay model was introduced and used in [32]. It suggested an ellipse width that changes with respect to the distance between an obstruction and that link. This model is represented as [29]

$$\mathbf{W}_{l,p}^{Exp} = e^{-\frac{\lambda_{l,p}}{2\sigma_\lambda}} \begin{cases} 1, & \text{if } \lambda_{l,p} \geq 0 \\ 0, & \text{otherwise} \end{cases}, \qquad (2.27)$$

where σ_λ is a tunable parameter that controls the decay rate of attenuation with respect to λ.

17

2.4.5 *Inverse Area Model.*

The Inverse Area model is similar to the Exponential Decay model, but suggests that some areas within the ellipse are affected more by the link than other areas [33]. RF signals along the edge of the ellipse travel a further distance than when they travel directly LOS through the center of the ellipse and should have less of a weight. Therefore, the weight on each pixel is affected by the inverse area of the ellipse [33]. The Inverse Area model was used in [34], [35], [36] and is represented as

$$
\mathbf{W}_{l,p}^{InvArea} = \frac{1}{A_l}
\begin{cases}
1, & \text{if } d_{l,pcenter}(1) + d_{l,pcenter}(2) < d_l + \lambda \\
0, & \text{otherwise}
\end{cases},
\tag{2.28}
$$

where A_l is the area of the ellipse defined by d_l and λ.

2.5 Noise Model

The central limit theorem states that the sum of an infinite number of Independent and Identically Distributed (IID) random variables will converge to a random variable that is Gaussian in distribution [18], [37]. Furthermore, [37] states that the random variables does not necessarily have to be identically distributed, as long as one term does not dominate the sum. For a large, but finite number of random variables, the sum is approximately Gaussian in distribution.

Fading loss caused by deep fade and anti-fade in a multipath environment is difficult to measure and considered a nuisance parameter. All other noise parameters are assumed to have a Gaussian distribution. Applying the central limit theorem to (2.7), the sum of these random variables can be modeled as a single Gaussian distribution for $n_l(t)$ [18], [37].

Experiments were also conducted in [4], [7], [38] to model noise. Experimental data in [4] suggested a mixture of two Gaussian distributions for modeling noise. The first Gaussian distribution has a probability of 0.548 and standard deviation of $\sigma_n = 0.971$ dB. The second distribution has a probability of 0.452 and standard deviation of $\sigma_n = 3.003$

dB. However, research in [38] stated that while a skew-Laplacian noise model is a more accurate representation of the noise measured, Additive White Gaussian Noise (AWGN) was sufficient enough for RTI position tracking. AWGN is a typical distribution used to model noise [30], [32], [39]. Experimental data from [7] found that an AWGN model with a standard deviation of $\sigma_n = 4$ dB or 6 dB was a good fit for their transceivers, which are the same as those used in this thesis.

2.6   Image Estimation

A common estimation method to obtain an optimal solution is the least squares solution. The least squares solution to (2.12) is [4]

$$\hat{\mathbf{x}}_{LS} = \underset{\mathbf{x}}{\operatorname{argmin}} \|\mathbf{W}\mathbf{x} - \mathbf{y}\|_2^2. \tag{2.29}$$

Taking the gradient of (2.29) and setting it to equal zero yields [4]

$$\hat{\mathbf{x}}_{LS} = \left(\mathbf{W}^T\mathbf{W}\right)^{-1}\mathbf{W}^T\mathbf{y}. \tag{2.30}$$

The problem with the least squares solution is that it only exists if $\mathbf{W}$ is full rank, which normally is not the case for RTI. RTI is an ill-posed inverse problem where small singular values can potentially lead to large errors and meaningless estimates [21]. Regularization is a method commonly used to solve ill-posed problems [40]. Regularization is a technique applied to inverse problems that involves adding extra information to a matrix that is not full rank to make the data more useful [4].

2.7   Regularization

Numerous regularization techniques exists in the literature aimed at solving ill-posed problems [40]. However, certain regularization techniques are complicated and computationally expensive. The image reconstruction process must be fast enough to provide quick updates of estimated attenuation images for real-time RTI applications. Small computational requirements, while preserving accuracy, are important properties

when choosing an ideal regularization technique for RTI. A few simple linear regularization methods are discussed in the rest of this section.

2.7.1 Linear Back Projection.

Linear back projection was suggested in [25] as the simplest image reconstruction technique to deal with the ill-posed problem by using $\mathbf{W}^T$ as a mapping between the shadowing loss and pixels. Mathematically, this is shown as

$$\hat{\mathbf{x}}_{LBP} = \mathbf{W}^T\mathbf{y}. \tag{2.31}$$

However, [25] found that this technique did not take the profound effect of noise into account and did not produce accurate images.

2.7.2 Tikhonov.

Tikhonov regularization is a well-known regularization technique and is most commonly used in RTI [4], [21], [25]. The objective function of Tikhonov regularization is represented as [4], [21]

$$f(x) = \frac{1}{2}\|\mathbf{W}\mathbf{x} - \mathbf{y}\|^2 + \alpha\|\mathbf{Q}\mathbf{x}\|^2, \tag{2.32}$$

where α is a tunable regularization parameter and $\mathbf{Q}$ is the Tikhonov matrix. The regularization parameter, α, affects the quality of the regularization [25]. The higher the regularization parameter, the smoother the image becomes and the more actual attenuation from obstructions becomes lost. The lower the regularization parameter, the more noise is contained within the image. The regularization parameter is usually determined ad-hoc and must balance between smoothing too much of the image and an acceptable noise tolerance.

Taking the derivative of (2.32) and setting it to zero yields the regularized least squares solution as [4], [21]

$$\hat{\mathbf{x}}_{TIK} = \mathbf{\Pi}_{TIK}\mathbf{y}, \tag{2.33}$$

$$\mathbf{\Pi}_{TIK} = \left(\mathbf{W}^T\mathbf{W} + \alpha\mathbf{Q}^T\mathbf{Q}\right)^{-1}\mathbf{W}^T. \tag{2.34}$$

There are a couple methods explored in the literature to compute Tikhonov regularization.

First-Order Tikhonov. The First-Order Tikhonov regularization is a commonly used Tikhonov regularization technique in RTI and was used in [4], [5], [21], [22], [7], [25], [29], [41]. The gradient of the image is penalized in First-Order Tikhonov regularization. By penalizing the energy found in each first derivative, noise spikes are suppressed and a relatively flat image is produced [42]. In RTI, a difference matrix is typically used to approximate the first derivative of the Tikhonov matrix. The First-Order Tikhonov matrix is represented as [14]

$$\mathbf{Q} = \mathbf{D}_H^T \mathbf{D}_H + \mathbf{D}_V^T \mathbf{D}_V, \tag{2.35}$$

where $\mathbf{D}_H$ is the difference operator in the horizontal direction and $\mathbf{D}_V$ is the difference operator in the vertical direction. Incorporating (2.35) to (2.34) yields the least squares solution using First-Order Tikhonov regularization as

$$\hat{\mathbf{x}}_{FOTIK} = \mathbf{\Pi}_{FOTIK}\mathbf{y}, \tag{2.36}$$

$$\mathbf{\Pi}_{FOTIK} = \left(\mathbf{W}^T\mathbf{W} + \alpha\left(\mathbf{D}_H^T\mathbf{D}_H + \mathbf{D}_V^T\mathbf{D}_V\right)\right)^{-1}\mathbf{W}^T. \tag{2.37}$$

Second-Order Tikhonov. Similar to First-Order Tikhonov regularization, the Second-Order Tikhonov regularization penalizes the second derivative of the image. Penalizing the energy found in the second derivative suppresses the noise and produces a relatively smooth image [42]. Again, a difference matrix can be used to approximate the second derivative. The Second-Order Tikhonov matrix is represented as

$$\mathbf{Q} = \mathbf{D}_{2H}^T \mathbf{D}_{2H} + \mathbf{D}_{2V}^T \mathbf{D}_{2V}, \tag{2.38}$$

where $\mathbf{D}_{2H}$ is the second-order difference operator in the horizontal direction and $\mathbf{D}_{2V}$ is the second-order difference operator in the vertical direction. The least squares solution using Second-Order Tikhonov regularization is

$$\hat{\mathbf{x}}_{SOTIK} = \mathbf{\Pi}_{SOTIK}\mathbf{y}, \tag{2.39}$$

$$\mathbf{\Pi}_{SOTIK} = \left(\mathbf{W}^T\mathbf{W} + \alpha\left(\mathbf{D}_{2H}^T\mathbf{D}_{2H} + \mathbf{D}_{2V}^T\mathbf{D}_{2V}\right)\right)^{-1}\mathbf{W}^T. \tag{2.40}$$

2.7.3 Covariance Matrix.

Another common regularization method uses the *a priori* covariance matrix, $\mathbf{C}_x$, and the variance in the noise, σ_n^2. The covariance matrix was used in [9], [16], [23], [27], [28], [34], [35], [36]. $\mathbf{C}_x$ is computed by using an approximation of the Poisson process, which is common for estimating random placement of objects [4]. $\mathbf{C}_x$ is computed as an exponential decay function [16]

$$[\mathbf{C}_x]_{p_1,p_2} = \sigma_x^2 e^{\left(-\frac{d_{p_1,p_2}}{\delta_c}\right)}, \tag{2.41}$$

where σ_x^2 is the variance of the pixel attenuation, d_{p_1,p_2} is the distance between pixel p_1 and pixel p_2, and δ_c is a tunable correlation parameter, similar to α in Tikhonov regularization [16]. The least squares solution using the covariance matrix is [9]

$$\hat{\mathbf{x}}_{Cov} = \mathbf{\Pi}_{Cov}\mathbf{y}, \tag{2.42}$$

$$\mathbf{\Pi}_{Cov} = \left(\mathbf{W}^T\mathbf{W} + \sigma_n^2\mathbf{C}_x^{-1}\right)^{-1}\mathbf{W}^T. \tag{2.43}$$

2.7.4 Truncated Singular Value Decomposition.

Truncated Singular Value Decomposition (TSVD) is a regularization technique that limits the dimensionality of the weight matrix $\mathbf{W}$ and was discussed in [21], [40]. The benefits of TSVD is that it is intuitive and easy to compute if the matrix can be broken down into its Singular Value Decomposition (SVD). However, research in [21] found that TSVD regularization technique produced much noisier images than Tikhonov regularization. In the case of RTI, $\mathbf{W}$ can be broken up into its SVD as [21]

$$\mathbf{W} = \mathbf{U}\mathbf{\Lambda}\mathbf{V}^T, \tag{2.44}$$

where $\mathbf{U}$ is a unitary matrix, $\mathbf{\Lambda}$ is the diagonal matrix containing singular values, and $\mathbf{V}$ is a unitary matrix [21]. Plugging (2.44) into (2.30) yields [21]

$$\hat{\mathbf{x}}_{TSVD} = \mathbf{V}\mathbf{\Lambda}^{-1}\mathbf{U}^T\mathbf{y} = \sum_{j=1}^{N}\frac{1}{\theta_j}\mathbf{u}_j^T\mathbf{y}\mathbf{v}_j, \tag{2.45}$$

where θ_j is the jth diagonal element of $\mathbf{\Lambda}$. In TSVD, only the largest i singular values are computed to recreate the image. Therefore, (2.45) is rewritten as [21]

$$\hat{\mathbf{x}}_{TSVD} = \mathbf{\Pi}_{TSVD}\mathbf{y}, \tag{2.46}$$

$$\mathbf{\Pi}_{TSVD} = \sum_{j=1}^{i<N} \frac{1}{\theta_j}\mathbf{u}_j^T\mathbf{v}_j = \mathbf{V}_i\mathbf{\Lambda}_i^{-1}\mathbf{U}_i^T. \tag{2.47}$$

2.8 Variations of RTI

Several variations of RTI have been suggested in the literature to improve or optimize the localization accuracy of RTI. The remainder of this section presents some of them.

2.8.1 Channel Diversity RTI.

Indoor environments typically contain a highly multipath environment due to numerous obstructions. Communication links are reflected, diffracted, scattered, and shadowed by numerous indoor objects [43]. Depending on the frequency, the link can either be in anti-fade, where phasor sum of the RSS is constructive, or deep fade, where the phasor sum of the RSS is destructive. For RTI, it is ideal for communication links to be in anti-fade to receive the strongest RSS possible for each link and obtain the most reliable attenuation values [16]. Links in deep fade can create a variance in RSS even when there are no targets interfering with the link. When a target is standing in between the link in deep fade, the RSS may not change at all or actually go up on average [22].

The research in [16] suggested using multiple frequencies or channels to improve localization accuracy. Channel Diversity RTI (cdRTI) in [16] used the shadowing-based RTI method to measure RSS in calibration mode, but measured RSS for a user-defined number of channels. Packet Reception Rate (PRR) method and fade level method were the two methods suggested to select the m number of best channels to use. In the PRR method, the m number of channels with the best PRR were selected for each link during calibration. For the fade level method, the average RSS was measured for each channel and

23

the *m* channels with the highest RSS were selected. The RSS of the *m* highest values were then averaged to obtain a vector of RSS.

The results in [16] showed much greater localization accuracy compared to the traditional single channel RTI method. The disadvantage with this method, however, was that more time was required to collect RSS since each transceiver had to transmit its signal *m* number of times for each channel.

2.8.2 *Directional RTI.*

Another variation of RTI used transceivers with electronically-switched directional antennas instead of common omnidirectional antennas [26]. The direction, angle, and frequency of the transceivers affect the link strength and cause destructive or constructive interference as mentioned in Section 2.8.1. Directional RTI (dRTI) was proposed in [26] and used electronically-switched directional antennas with six different directions. The research determined that dRTI was able to provide greater changes and variances in RSS when an obstruction was interfering with the links than omnidirectional antennas. However, this method had a greater overhead cost since the electronically-switched directional antenna required more energy and more communication links were needed to determine the best antenna directions.

2.8.3 *Dial-It-In RTI.*

Similar to dRTI, the research in [36] suggested installing RF transceivers on servo motors that could autonomously reposition the transceivers in eight different positions. The servo motors autonomously moved the transceivers to obtain the position with the greatest anti-fade link measurements during calibration time. This research was able to increase position estimation accuracy over the traditional RTI method by rotating the transceivers to a better position.

2.8.4   3-D RTI.

In almost all previous RTI research, wireless transceivers were placed at the same height in a WSN. The research in [29] created a WSN with transceivers at four different heights to create a Three-Dimensional (3-D) RTI network. Using shadowing-based RTI, this research demonstrated that RTI can be applied to not only determine the position of a target, but possibly also extract target features such as height and density [29]. Another research utilizing the 3-D RTI network had a layout of transceivers with two different height positions [10]. By imaging multiple layers within the network with respect to height, this research showed a proof-of-concept that a 3-D RTI network could detect whether a person was standing, sitting, or lying down.

2.9   Cylindrical Human Model

An actual truth attenuation image is very difficult, if not impossible, to create because the size, shape, clothing, etc., of a target and the surrounding environment will affect the estimated attenuation image. Since there is no actual truth attenuation image, a representative truth image must be created for simulations and to compare quality of estimated attenuation images. The research in [4] suggested a simple model called the uniformly attenuating cylindrical human model. Given the position of a target at (x_T, y_T), the modeled attenuated truth image is calculated as [4]

$$x_p = \begin{cases} 1, & \text{if } \|x_{pcenter} - (x_T, y_T)\| < R_T \\ 0, & \text{otherwise} \end{cases}, \tag{2.48}$$

where x_p is the pth pixel, $x_{pcenter}$ is the position at the center location of the pixel, and R_T is the radius of the human model. This model was used in [4], [6], [29].

III.   Methodology

THIS chapter discusses the methodology utilized in this research to determine the applicability and characterize the capabilities of using multiple WSNs for RTI. First, Section 3.1 and Section 3.2 present the parameters and assumptions made in this research.   Section 3.3 presents the metrics used to characterize and compare different WSN configurations in this research.   Section 3.4 discusses the analytical method for combining RSS information from multiple WSNs to create one combined attenuation image, as well as present the theoretical relationship between transceivers, links, and computational complexities.   Section 3.5 and Section 3.6 present the various network configurations, stationary positions, and moving patterns conducted in this research to obtain a representative sample of the entire network.   Section 3.7 explains the process for generating simulated RSS data for stationary and moving targets. Finally, Section 3.8 concludes the chapter by presenting the tools used to create multiple WSNs and the methodology for conducting live experiments at AFIT.

3.1   Parameters

This research uses the linear system model (2.12) in Section 2.3.1 with the shadowing-based RSS measurement model. This research also utilizes the Line weight model because it is computationally cheap to implement and does not require the input of an extra variable λ that defines the width of an ellipse. First-Order Tikhonov regularization has shown to provide good regularization for suppressing noise in RTI and has the flexibility to change the degree of suppression by altering α values. For that reason, this research uses First-Order Tikhonov regularization to find the least squares solution. For a pixel size of 0.5 ft $\times$ 0.5 ft or 1.0 ft $\times$ 1.0 ft, research in [29] discovered a regularization value of $\alpha = 75$ provided attenuation images with a good balance between suppressing noise while keeping

26

the target still clearly identifiable. Therefore, all attenuation images in this research use a regularization parameter of $\alpha = 75$ and have a pixel size of 0.5 ft $\times$ 0.5 ft. In summary, this research utilizes the following parameters [29]

- System Model: $\mathbf{y} = \mathbf{Wx} + \mathbf{n}$

- Measurement Model: $\mathbf{y} = [\Delta y_1, \Delta y_2, \cdots, \Delta y_M]^T$

- Calibration: $\mathbf{y}_c = [\bar{y}_{c,1}, \bar{y}_{c,2}, \cdots, \bar{y}_{c,M}]^T$

- Weight Model: $\mathbf{W}_{l,p}^{Line} = S L_{l,p} \begin{cases} 1, & \text{if link } l \text{ traverses through pixel } p \\ 0, & \text{otherwise} \end{cases}$

- Estimator: $\hat{\mathbf{x}}_{FOTIK} = \underset{x}{\text{argmin}} \left(\frac{1}{2}\|\mathbf{Wx} - \mathbf{y}\|^2 + \alpha\|\mathbf{Qx}\|^2 \right)$

- Tikhonov Matrix: $\mathbf{Q} = \mathbf{D}_H^T \mathbf{D}_H + \mathbf{D}_V^T \mathbf{D}_V$

- α: 75

- Pixel Size: 0.5 ft $\times$ 0.5 ft

3.2 Assumptions

The following assumptions are made in this research [29]

1. $\mathbf{n} \sim \mathcal{N}\left(\mathbf{0}, \sigma_n^2 \mathbf{I}_M\right)$.

2. $\mathbf{y}|\mathbf{x} \sim \mathcal{N}\left(\mathbf{Wx}, \sigma_n^2 \mathbf{I}_M\right)$.

3. Calibration data for the network is available.

4. Transmitted power and static losses are constant and are canceled out when computing the change in RSS.

5. There is always one target within the network.

6. Target is big and tall enough to obstruct the LOS of transceivers.

7. RSS attenuation is uniform over the area of a pixel.

8. All transceivers are designed and manufactured exactly the same way and so all transceivers function the same way.

9. Transceivers transmit in sequential order instead of simultaneously and, therefore, there is a linear relationship between the number of transceivers and time required for all transceivers to transmit their RF signal.

10. For simulations, the *BaseStation* transceiver is always within range of the transceivers in the WSN(s) and there are never any dropped RSS packets.

3.3   Metrics

Frame rate, computational complexity, and image quality are the three metrics utilized in this research to characterize each RTI network configuration. The remainder of this section describes each metric.

3.3.1   *Frame Rate.*

The time required for all transceivers to transmit their RF signal and obtain one frame of data is used as a metric to compare the capabilities of each RTI network configuration. The higher the frame rate, the quicker a set of RSS data is acquired and the more often information is updated to the user. Frame rate is critical for real-time applications of RTI where time is a factor, such as in emergency or security situations.

3.3.2   *Computational Complexity.*

In RTI, the limits of computational complexity on a computer is calculating the Π matrix. As the number of transceivers increases in the WSN, the computational complexity can increase by $O(K^6)$ [14]. Therefore, computational complexity can become a choke point in large-scale RTI networks. Any processing computer has a finite amount of memory and can only perform calculations on matrices up to a certain size. This limitation determines a maximum number of transceivers that can be deployed in the network, which affects the maximum coverage area possible for the network or the density of transceivers. Therefore, computational complexity of computing the least squares solution in (2.36) is another metric used to compare each RTI network configuration.

3.3.3 Image Quality.

Image quality is the final metric used in this research to compare each RTI network configuration. Image quality, subjectively or objectively, determines whether the estimated attenuation image is of any use. An image with too low of a resolution or too much noise does not provide any useful information for a user, making the system useless. This research takes an objective approach on determining image quality by comparing the SNR and accuracy in position estimates between each attenuation image.

3.3.3.1 Signal-to-Noise Ratios.

SNR is a common image quality comparison technique to quantify the quality of an estimated image with a truth image. However, since there is no actual truth data to compare each estimated attenuation image with, the uniformly attenuating cylindrical human model described in Section 2.9 is used to generate representative truth images. Research in [4] used the uniformly attenuating cylindrical human model with radius $R_T = 1.3$ ft.

SNR. SNR is a very common metric used to compare the quality of the intended signal to a noisy signal. Applying this metric to RTI, the truth image uses the uniformly attenuating cylindrical human model with $R_T = 1.3$ ft and the noisy image is the estimated attenuation image. Mathematically, this is shown in dB as

$$SNR = 10\log_{10}\left[\frac{Var(\mathbf{x}_{truth})}{\frac{1}{N_H N_V}\sum_{i=1}^{N_H}\sum_{j=1}^{N_V}\left(x_{truth,i,j} - x_{est,i,j}\right)^2}\right], \tag{3.1}$$

where N_V is the number of pixels in the vertical direction, N_H is the number of pixels in the horizontal direction, x_{truth} is the pixel within the truth image, and x_{est} is the pixel within the estimated attenuation image.

PSNR. Peak Signal-to-Noise Ratio (PSNR) is a well-used metric to compare image quality [44], [45]. However, since there is no truth data to compare the estimated image with, a slightly modified version of PSNR is used to characterize the estimated attenuation image. For this situation, PSNR is computed by finding the maximum intensity value

29

within a 1.3 ft radius of the true position of the target squared over the variance of the rest of the estimated attenuation image. Any attenuation values outside the 1.3 ft radius of the true position of the target is noise. This can mathematically be shown in dB as [46]

$$PSNR = 10\log_{10}\left[\frac{Max(\mathbf{x}_T)^2}{Var(\mathbf{x}_{nT})}\right],\tag{3.2}$$

where $\mathbf{x}_T \subset \mathbf{x}$ is the subset of pixels within 1.3 ft of the radius of the true position of the target and $\mathbf{x}_{nT} \subset \mathbf{x}$ is the subset of pixels that is not within 1.3 ft of the true position of the target.

3.3.3.2 RMSE.

While position estimation is not the focus of this research, it does provide an objective metric on determining the quality of the estimated attenuation image. This research compares the estimated location of the target with the actual location of the target as another metric to determine image quality. Root Mean Squared Error (RMSE) is used to determine how well each network is able to accurately estimate the position of the target. Position error is first computed by finding the Euclidean distance between the estimated position of the target and the actual position of the target as

$$\epsilon_d = \|(\hat{x}, \hat{y}) - (x_T, y_T)\|,\tag{3.3}$$

where $(\hat{x}, \hat{y})$ is the estimated position of the target and (x_T, y_T) is the true position of the target. The Mean Squared Error (MSE) is calculated by summing the squared position error, ϵ_d^2, for each data frame and dividing by the total number of position estimates. This is mathematically shown as

$$MSE = \frac{1}{N_f}\sum_{f=1}^{N_f}\epsilon_{d,f}^2,\tag{3.4}$$

where N_f is the total number of frames for the experiment and $\epsilon_{d,f}$ is the position error for frame f. The RMSE is then simply the square root of (3.4) as

$$RMSE = \sqrt{MSE}.\tag{3.5}$$

This research uses three simple position estimation techniques to compare with the true position.

Maximum Value. A simple position estimation technique is to find the pixel with the maximum intensity value within the estimated attenuation image and use the center of that pixel as the position of the target. This method was used in [16], [29] and can be shown as [23]

$$p_{center} = \underset{p}{\operatorname{argmax}} \, \mathbf{x}_p. \tag{3.6}$$

1-D Projection. One-Dimensional (1-D) projection is a technique used to reduce the dimensionality of an image and potentially increase SNR [47], [48]. Therefore, another simple method for estimating the position of a target is to apply a 1-D projection to the estimated attenuation image in the vertical and horizontal directions. This is accomplished by summing all the rows of an estimated attenuation image and taking the maximum intensity pixel as the estimated $\hat{x}$ position. Similarly, the columns of the estimated attenuation image are summed to find the maximum intensity pixel as the estimated $\hat{y}$ position.

Gaussian Kernel. A Gaussian kernel smoothing filter is typically applied to blur an image and suppress any noise spikes [49]. This method was also used in [34] to denoise an estimated attenuation image. Mathematically, the Gaussian kernel is shown as [34]

$$\mathbf{G}(x, y) = \frac{1}{2\pi\sigma_G^2} e^{-\frac{x^2+y^2}{2\sigma_G^2}}, \tag{3.7}$$

where σ_G^2 is the variance of the Gaussian kernel. For this research, a symmetric Gaussian kernel filter is used to help smooth the noisy estimated attenuation image prior to finding the maximum intensity value as the position estimate. Each attenuation image is filtered by a $[5 \times 5]$ Gaussian kernel filter matrix. From prior experiments, $\sigma_G = 2$ for the Gaussian kernel provided an ideal balance between reduction in noise without smoothing too much

of the target. The values for the Gaussian kernel filter matrix is

$$
\mathbf{G}(x, y) = \begin{bmatrix}
0.0232 & 0.0338 & 0.0383 & 0.0338 & 0.0232 \\
0.0338 & 0.0492 & 0.0558 & 0.0492 & 0.0338 \\
0.0383 & 0.0558 & 0.0632 & 0.0558 & 0.0383 \\
0.0338 & 0.0492 & 0.0558 & 0.0492 & 0.0338 \\
0.0232 & 0.0338 & 0.0383 & 0.0338 & 0.0232
\end{bmatrix}. \tag{3.8}
$$

3.4 Analytical

3.4.1 Updated System Model.

As mentioned in Section 2.3.1, for a traditional RTI scenario with one WSN, $\mathbf{y} \in \mathcal{R}^{M \times 1}$ represents the vector of RSS. $\mathbf{W} \in \mathcal{R}^{M \times N}$ is the weight matrix and $\mathbf{x} \in \mathcal{R}^{N \times 1}$ is the vector of pixels within the WSN.

The traditional RTI system model needs to be updated for a scenario where there are more than one WSN. For two WSNs, let $\mathbf{y}_1 \in \mathcal{R}^{M_1 \times 1}$ be the vector of RSS link measurements of the first network where M_1 is the total number of unique links within the first network. Also, let $\mathbf{W}_1 \in \mathcal{R}^{M_1 \times N_1}$ be the weight matrix and $\mathbf{x}_1 \in \mathcal{R}^{N_1 \times 1}$ be the vector of pixels of the first network where N_1 is the total number of pixels within the first network. Similarly, let $\mathbf{y}_2 \in \mathcal{R}^{M_2 \times 1}$ be the vector of RSS link measurements, $\mathbf{W}_2 \in \mathcal{R}^{M_2 \times N_2}$ be the weight matrix, and $\mathbf{x}_2 \in \mathcal{R}^{N_2 \times 1}$ be the vector of pixels for the second network where M_2 is the total number of unique links and N_2 is total number of pixels within the second network. All pixels within this combined network area is in either $\mathbf{x}_1$, $\mathbf{x}_2$, or both depending on if the two WSNs are overlapping each other. $\mathbf{x}_1$ can be split into $\mathbf{x}_{1s}$ and $\mathbf{x}_{1k}$, where $\mathbf{x}_{1s} \in \mathcal{R}^{N_{1s} \times 1}$ represents the vector of pixels that are solely within the first WSN and $\mathbf{x}_{1k} \in \mathcal{R}^{N_{1k} \times 1}$ represents the vector of pixels that are present in both networks. Similarly, $\mathbf{x}_2$ can be split into $\mathbf{x}_{2k}$ and $\mathbf{x}_{2s}$, where $\mathbf{x}_{2k} \in \mathcal{R}^{N_{2k} \times 1}$ represents the vector of pixels that are present in both networks and $\mathbf{x}_{2s} \in \mathcal{R}^{N_{2s} \times 1}$ represents the vector of pixels that are solely within the second network. Since $\mathbf{x}_{1k}$ and $\mathbf{x}_{2k}$ contain the same pixels, let $\mathbf{x}_{1k} = \mathbf{x}_{2k} =$

$\mathbf{x}_k \in \mathcal{R}^{N_k \times 1}$ represent the vector of pixels that are present in both networks. Fig. 3.1 shows an example of the three different pixel regions within an area with two WSNs.

The weight matrix for each network can also be divided into two regions, corresponding with the pixel regions. $\mathbf{W}_1$ can be split into $\mathbf{W}_1 = [\mathbf{W}_{1s}|\mathbf{W}_{1k}]$ and $\mathbf{W}_2$ can be split into $\mathbf{W}_2 = [\mathbf{W}_{2k}|\mathbf{W}_{2s}]$, where $\mathbf{W}_{1k}$ and $\mathbf{W}_{2k}$ represent a subset of their entire weight matrix, respectively, that contains the pixels, $\mathbf{x}_k$, that overlap in both networks. The new linear model that incorporates two WSNs is shown as

$$
\begin{bmatrix} \mathbf{y}_1 \\ \mathbf{y}_2 \end{bmatrix} = \begin{bmatrix} \mathbf{W}_{1s} & \mathbf{W}_{1k} & \mathbf{0} \\ \mathbf{0} & \mathbf{W}_{2k} & \mathbf{W}_{2s} \end{bmatrix} \begin{bmatrix} \mathbf{x}_{1s} \\ \mathbf{x}_k \\ \mathbf{x}_{2s} \end{bmatrix} + \mathbf{n}, \tag{3.9}
$$

$$
\mathbf{y} = \mathbf{W}\mathbf{x} + \mathbf{n}, \tag{3.10}
$$

where $\mathbf{y} \in \mathcal{R}^{(M_1+M_2)\times 1}$ are the RSS link measurements of both networks, $\mathbf{W} \in \mathcal{R}^{(M_1+M_2)\times(N_{1s}+N_k+N_{2s})}$ is the combined weight matrix, $\mathbf{x} \in \mathcal{R}^{(N_{1s}+N_k+N_{2s})\times 1}$ is the combined image to be estimated, and $\mathbf{n} \in \mathcal{R}^{(M_1+M_2)\times 1}$ is AWGN. This updated model can be used to find the least squares solution for an attenuation image with two WSNs in the same way as the traditional RTI model.

3.4.2   *Unique Links.*

For the traditional RTI method with one WSN, there are $M = \frac{K(K-1)}{2}$ unique links where K is the number of transceivers within the WSN. If the total number of transceivers in one WSN is divided evenly for two WSNs, then each WSN will have $\frac{K}{2}$ transceivers. The total number of unique links for each network is

$$
M_1 = M_2 = \frac{\frac{K}{2}\left(\frac{K}{2} - 1\right)}{2}, \tag{3.11}
$$

where M_1 and M_2 is the number of unique links in the first network and second network, respectively. Multiplying (3.11) by two networks will give the total number of unique links
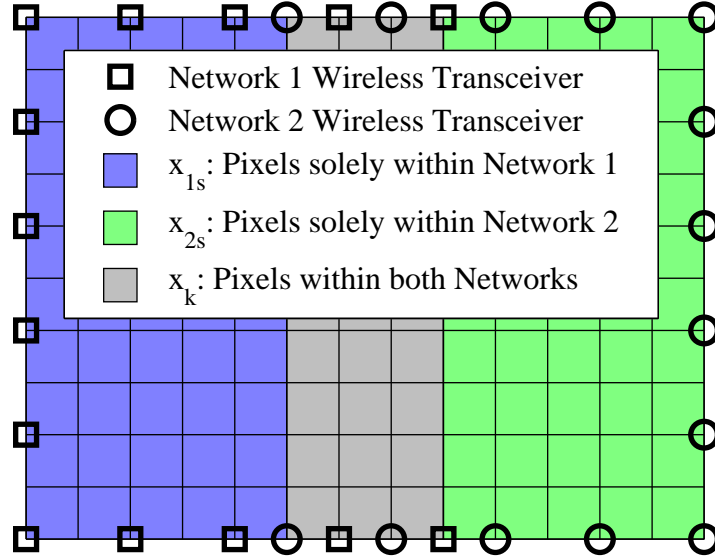
Figure 3.1: Pixel regions between 2 WSNs.

for both networks. This is mathematically shown as

$$M_1 + M_2 = 2 \frac{\frac{K}{2}\left(\frac{K}{2} - 1\right)}{2}. \tag{3.12}$$

The ratio in total number of unique links between two WSNs and one WSN is

$$\frac{M_1 + M_2}{M} = \frac{2\frac{\frac{K}{2}\left(\frac{K}{2}-1\right)}{2}}{\frac{K(K-1)}{2}} = \frac{\left(\frac{K}{2} - 1\right)}{K - 1} = \frac{\frac{1}{2}(K-2)}{K-1} = \frac{1}{2}\left(\frac{K-2}{K-1}\right). \tag{3.13}$$

The ratio in unique links between two WSNs and one WSN is $\approx \frac{1}{2}$ for $K \gg 2$. The ratio in unique links can be expanded to z number of networks. Using the same number of transceivers in one network, K, and dividing it evenly among each network, the ratio of unique links between z WSNs and one WSN is

$$\frac{M_1 + \cdots + M_z}{M} = \frac{z\frac{\frac{K}{z}\left(\frac{K}{z}-1\right)}{2}}{\frac{K(K-1)}{2}} = \frac{\left(\frac{K}{z} - 1\right)}{K - 1} = \frac{\frac{1}{z}(K-z)}{K-1} = \frac{1}{z}\left(\frac{K-z}{K-1}\right). \tag{3.14}$$

The ratio in links between having z WSNs and one WSN is approximately inversely proportional to the number of networks, or $\approx \frac{1}{z}$ for $K \gg z$.

3.4.3 Frame Rate.

The protocol in this research uses transceivers that transmit their RF signal in sequential order to prevent collisions. More information on the transceiver is discussed in Section 3.8.1. Assuming all transceivers are designed exactly the same and function the same, each transceiver should take the same amount of time to transmit a signal before moving to the next transceiver within a WSN. The size of the data package transmitted from each transceiver is also dependent on the number of transceivers within the WSN. Therefore, while there is not a direct linear relationship between the number of transceivers and the time it takes for all transceivers to transmit their RF signal, a network with twice as many transceivers will take roughly twice as long for all transceivers to transmit their RF signal. Similarly, a network with z times more transceivers will take roughly z times as long for all transceivers to transmit their RF signal.

3.4.4 Computational Complexity.

Computing an estimated attenuation image for RTI requires calculating the least squares solution with a regularization parameter. Typically, the $\mathbf{\Pi}$ matrix can be computed offline. However, there are certain situations and regularization techniques that require the calculation of the $\mathbf{\Pi}$ matrix online during real-time data collection. Using First-Order Tikhonov regularization, (2.36) and (2.37) must be computed. Table 3.1 shows the brute force computational complexity for each step in computing (2.36) and (2.37) for a network with z WSNs. N_{zt} is the total number of pixels within the combined estimated image of z WSNs and $M_1 + \cdots + M_z = M_{zt}$ is the number of unique links within z WSNs. Depending on the software and hardware of the processing computer, these steps can be optimized. However, that is not the focus of this research.

If the total number of transceivers, K, used in the network with one WSN and the network with two WSNs are the same, the ratio in computational complexity between one

Table 3.1: Theoretical computational complexity.

Step	z Network(s)
(I) Compute: $\mathbf{Q} = \mathbf{D}_H^T\mathbf{D}_H + \mathbf{D}_V^T\mathbf{D}_V$	$O(N_{zt}^2)$
(II) Multiply: $\alpha \cdot (I)$	$O(N_{zt}^2)$
(III) Compute: $\mathbf{W}^T\mathbf{W}$	$O(N_{zt}^2 \cdot zM_{zt})$
(IV) Add: $(III) + (II)$	$O(N_{zt}^2)$
(V) Invert: $(IV)^{-1}$	$O(N_{zt}^3)$
(VI) Multiply: $(V) \cdot \mathbf{W}^T$	$O(N_{zt}^2 \cdot zM_{zt})$
(VII) Multiply: $(VI) \cdot \mathbf{y}$	$O(N_{zt} \cdot zM_{zt})$
Total	$O\left(N_{zt}^3 + 2zN_{zt}^2M_{zt}\right)$

WSN and two WSNs is

$$\frac{Comp_{One}}{Comp_{Two}} = \frac{N^3 + 2N^2M}{N_{2t}^3 + 4N_{2t}^2M_{2t}}, \tag{3.15}$$

where N is the total number of pixels in the network with one WSN, M is the total number of unique links in the network with one WSN, N_{2t} is the total number of pixels in the network with two WSNs, and M_{2t} is the total number of unique links for the two WSNs. The ratio in computational complexity between one WSN and z WSNs is

$$\frac{Comp_{One}}{Comp_z} = \frac{N^3 + 2N^2M}{N_{zt}^3 + 2zN_{zt}^2M_{zt}}. \tag{3.16}$$

3.5 Network Setup

While Section 3.4 discusses the ability to use up to z WSNs, the remainder of this research focuses only on comparing the traditional RTI method with one WSN to a RTI network with two WSNs. The experiments conducted in this research use a total of 70 TelosB TPR2400 motes covering an area no greater than 19 ft × 16 ft to create one or more WSNs. Each mote is mounted approximately at a waist level height of 3 ft 4 in.

3.5.1 One Network.

For the traditional RTI method with one WSN, 70 transceivers are arranged in a rectangular grid covering an area of 19 ft × 16 ft. The transceivers are separated 1 ft apart from each other. Fig. 3.2 shows the layout of the transceivers for the traditional network.
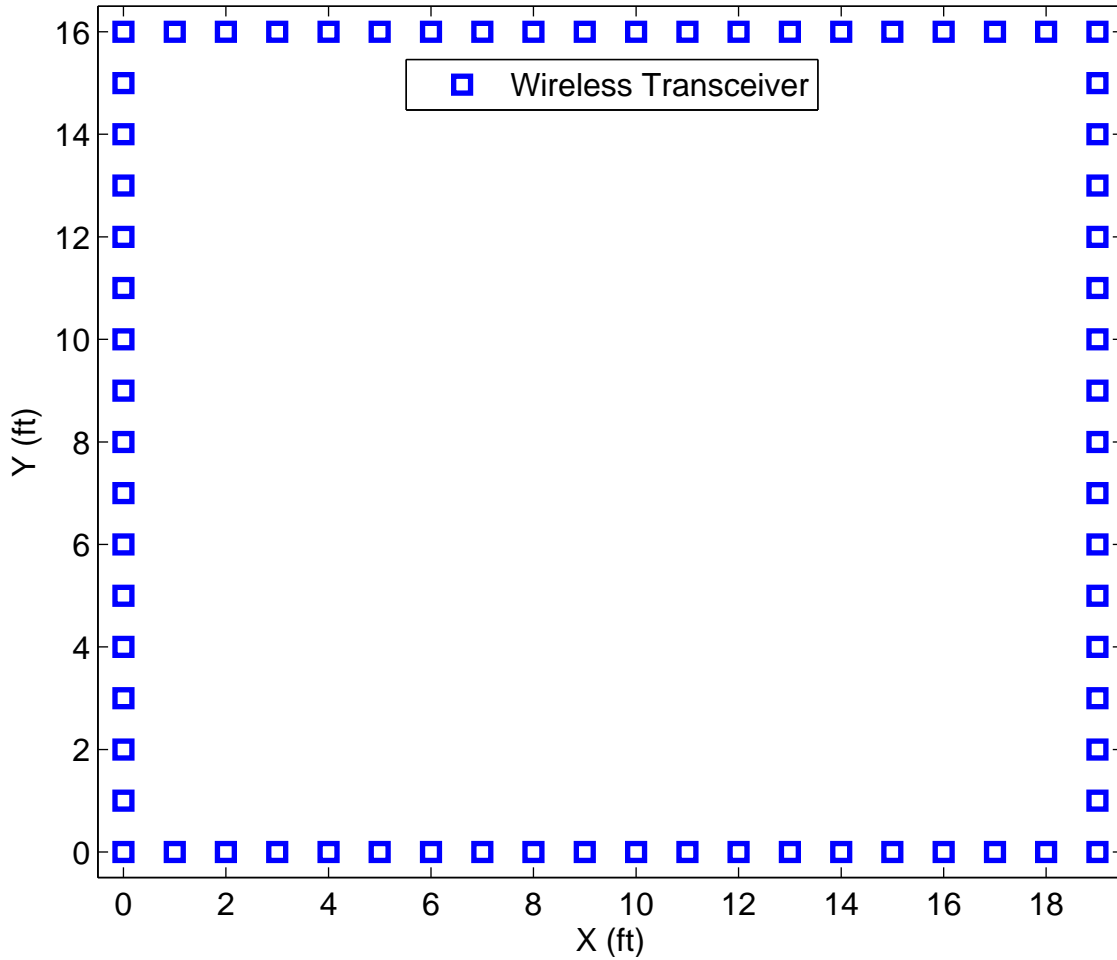
Figure 3.2: RTI network with one WSN.

3.5.2 Two Networks.

For a proper comparison between using one WSN and two WSNs, it is ideal to keep as many variables constant as possible. Unfortunately, it is impossible to keep all parameters the same and certain parameters have to be different. To create multiple WSNs that overlap each other, there are tradeoffs that can be categorized into three main areas: total number of transceivers, distance between each transceiver, and the total area covered in the WSNs.

Number of Transceivers. Changing the number of transceivers in a network affects the number of unique links across the network, changing the amount of data available

within the network. To keep the total number of transceivers the same while having two WSNs that overlap each other, the distance between each transceiver have to increase or the total network area of the network must decrease.

Transceiver Distance. Changing the distance between each transceiver will change the distance between certain links, changing the weight on each pixel per link. To keep the distance between each transceiver the same when creating two overlapping WSNs, the total number of transceivers must increase or the total area of the network must decrease.

Total Network Area. Assuming the pixel size remains constant, changing the total area of the network will change the number of pixels within the network. This will change the size of the weight matrix and computational complexity. To keep the total area the same between one WSN and two WSNs, the total number of transceivers must increase or the distance between each transceiver must increase.

Due to limited time and resources, only experiments changing the distance between each transceiver and experiments changing the total area of the network are conducted. Fig. 3.3 shows the four different network configurations with two WSNs that are used in this research. The network configurations in Fig. 3.3(a), Fig. 3.3(b), and Fig. 3.3(c) change the total area of the network while maintaining the same distance between each transceiver and same number of transceivers used as the traditional RTI network shown in Fig. 3.2. The network configuration in Fig. 3.3(d) changes the distance between each transceiver while maintaining the same total area of the network and same number of transceivers used as the traditional RTI network shown in Fig. 3.2.

For the remainder of this research, the network configuration in Fig. 3.3(a) will be referred to as the *Small* network configuration, the network configuration in Fig. 3.3(b) will be referred to as the *Medium* network configuration, the network configuration in Fig. 3.3(c) will be referred to as the *Large* network configuration, and the network configuration in Fig. 3.3(d) will be referred to as the *All* network configuration. The
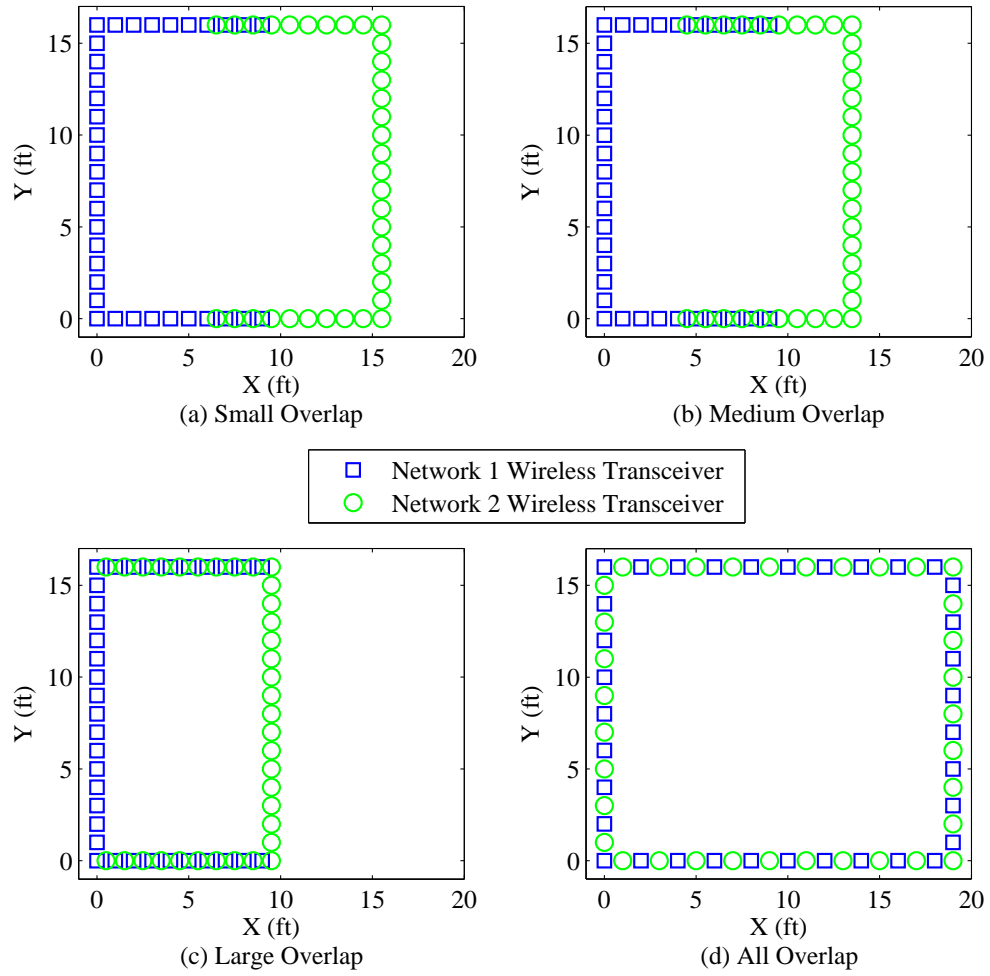
Figure 3.3: RTI network with two WSNs where wireless transceivers overlap each other. The network configurations in (a), (b), and (c) change the total area of the RTI network. Network configuration in (d) changes the distance between each transceiver.

network configuration in Fig. 3.2 will be referred to as the *One* network configuration.
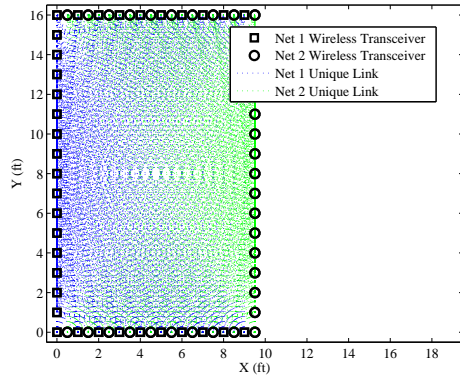
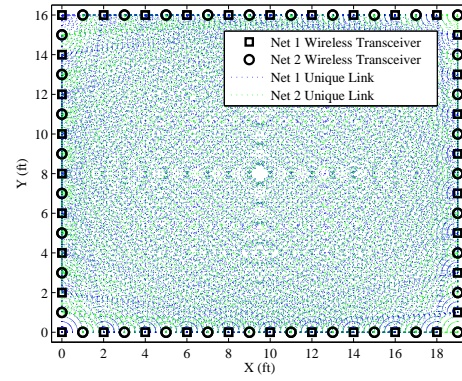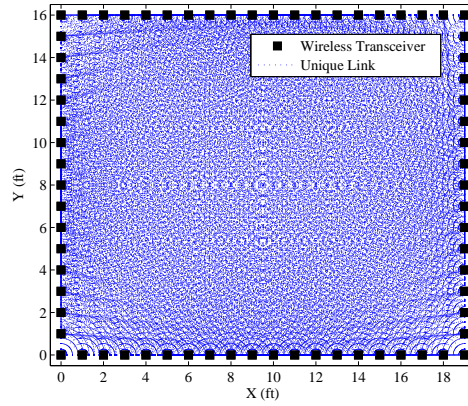Fig. 3.4 shows all the unique links for each network configuration.
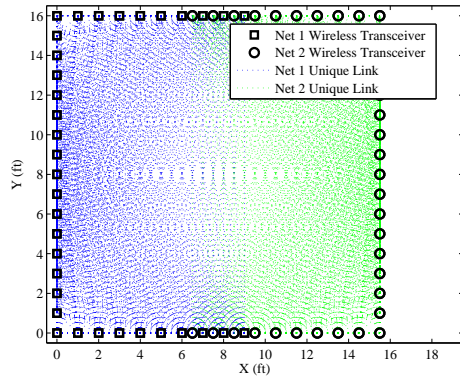
(a) *Small*
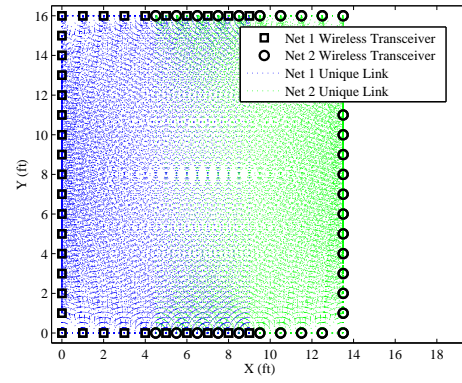
(b) *Medium*

(c) *Large*

(d) *All*

(e) *One*

Figure 3.4: Unique links per network configuration.

3.6 Target

Ultimately, the goal of RTI is to be able to detect, track, and localize targets within a network area. RTI has been shown to be capable of detecting multiple targets [34]. However, detecting multiple targets within a RTI network adds to the complexity of comparing each network configuration and is not the focus of this research. Therefore, only one target is tested within the network at any given time.

3.6.1 Stationary.

Various stationary positions are tested to cover all possible areas of interest within the total network area and provide an accurate comparison between each network configuration. A target stands at nine different positions. Fig. 3.5 shows the nine positions tested in this research. Due to symmetry of the network, only positions set in the lower left quadrant are needed.

3.6.2 Moving.

In a real-world situation, targets are not always stationary, but are likely moving around. RTI typically performs very well when a target is stationary since all transceivers can transmit their RF signal without the obstruction(s) moving to a different location. However, image quality quickly degrades when a target is moving since the transceivers are unable to all simultaneously transmit their RF signal. Various speeds and patterns are tested to characterize the effectiveness of using multiple WSNs for RTI. The true position of a target at any given time is also known by having predefined speeds and patterns.

3.6.2.1 Speed.

Various movement speeds are tested to cover a range of scenarios where a target may be moving fast or slow. This research uses three different speeds. For the remainder of this research, a movement speed of 1 foot per second is referred to as a slow pace, a speed of 2 feet per second is referred to as a normal pace, and a speed of 3 feet per second is referred to as a fast pace.

41
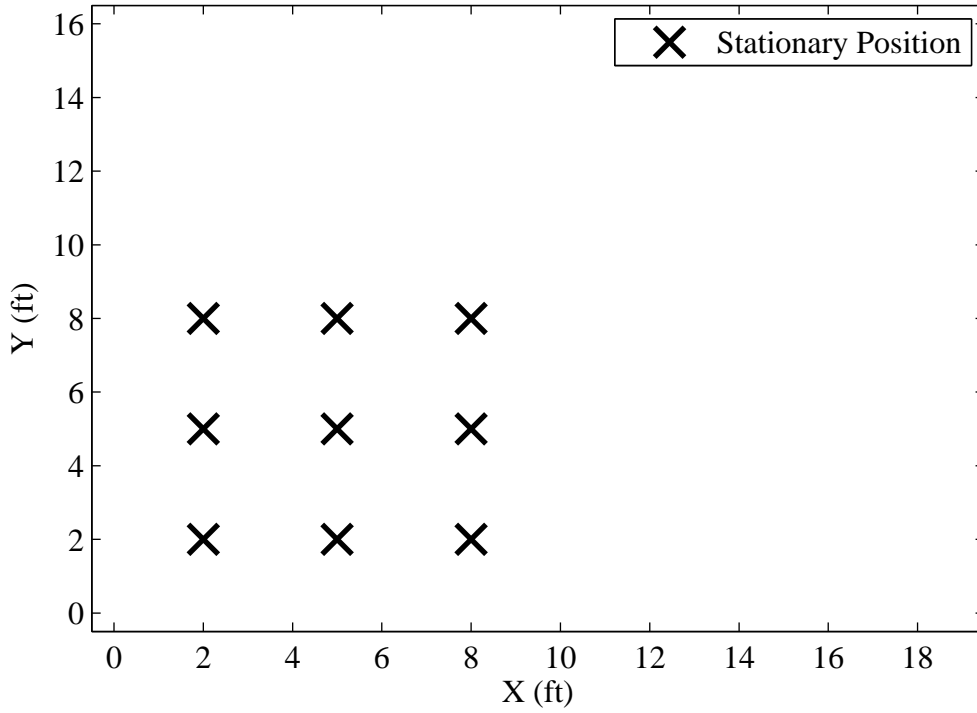
Figure 3.5: Nine different stationary positions tested within the WSN.

3.6.2.2 *Pattern.*

The target uses three different controlled patterns to move around within the WSN. This allows for proper post-analysis position estimation and comparison. Fig. 3.6, Fig. 3.7, and Fig. 3.8 show the three patterns. In each pattern, the target starts at position (2,2) ft. In the first pattern, the target walks in a rectangle, turning at (8,2) ft, (8,16) ft, (2,16) ft, and stopping back at (2,2) ft. This pattern test the ability of the network to image a target moving through the center of the network in the vertical *Y* direction. In the second pattern, the target turns at (8,2) ft, (8,8) ft, and stops at (2,8) ft. Once at (2,8) ft, the target turns around and retraces to (8,8) ft, (8,2) ft, and ending back at (2,2) ft. This pattern tests the ability of the network to image a target moving through the center of the network in both the horizontal *X* and vertical *Y* directions. The path slightly differs in the third pattern depending on the speed of the target. For a slow pace, the target walks to (2,16) ft, then
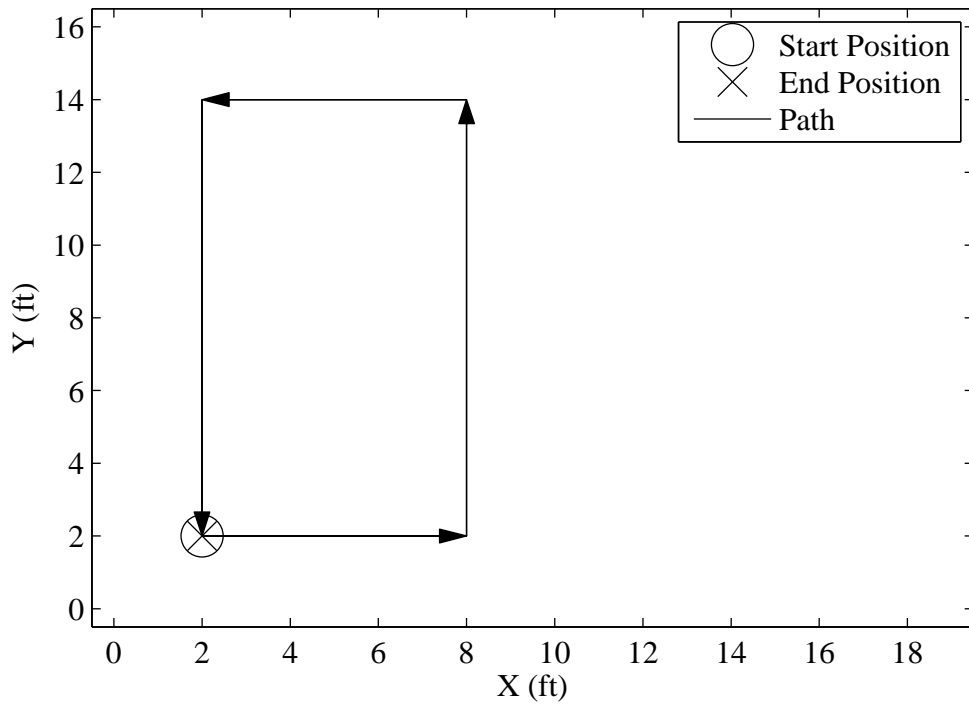
Figure 3.6: Pattern 1.

(3,16) ft, and ends at (3,2) ft. For a normal pace, the target walks to (2,16) ft, then (4,16) ft, and ends at (4,2) ft. For a fast pace, the target walks to (2,16) ft, then (5,16) ft, and ends at (5,2) ft. This pattern tests the ability of the network when a target walks mainly only along the edge of a network.
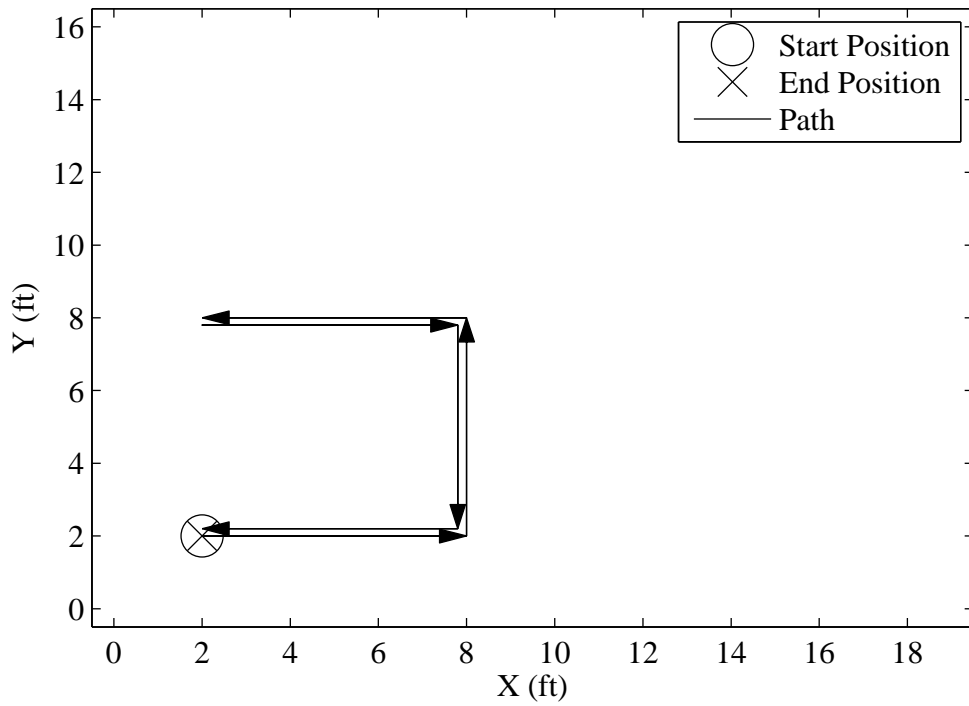
Figure 3.7: Pattern 2.
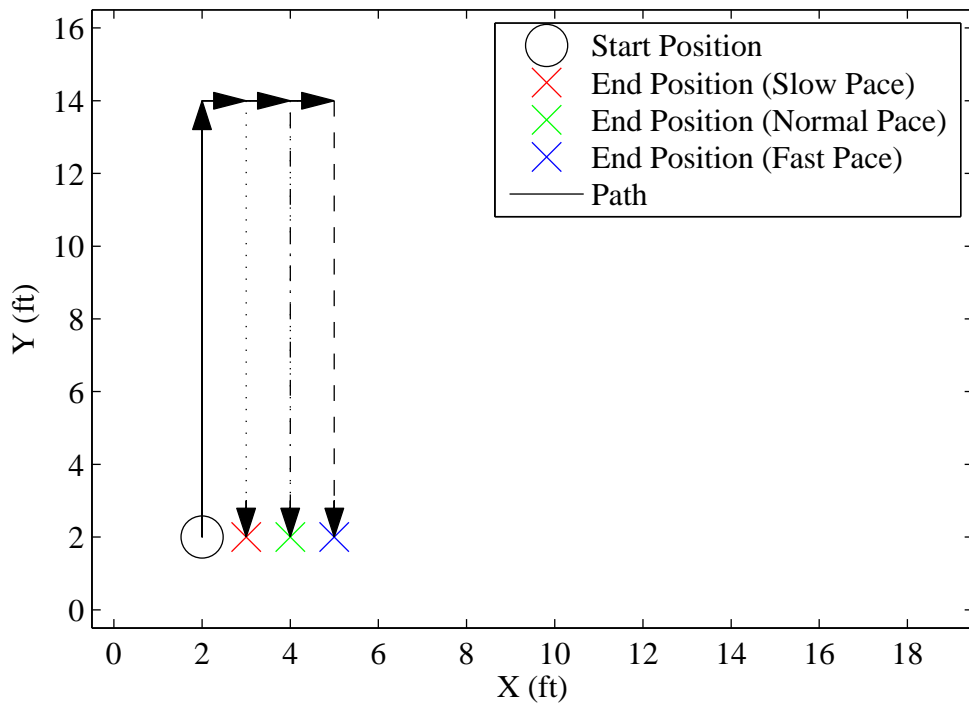
Figure 3.8: Pattern 3.

3.7 Simulations

Targets are simulated in a network using the uniformly attenuating cylindrical human model mentioned in Section 2.9. A cylindrical human model of radius $R_T \in \{$1 ft, 1.15 ft, 1.3 ft$\}$ are used to simulate various sizes of a human for each experiment. Fig. 3.9 shows an example of simulated attenuation images for different radii of the cylindrical human model without any noise. AWGN is discussed in Section 2.5 and is the model used to add noise to each simulated RSS with $\sigma_n \in \{$2 dB, 4 dB, 6 dB$\}$ for each experiment. Fig. 3.10 shows an example of attenuation images for the different σ_n. For simplicity and traceability, a WSN with 35 transceivers is set to collect data at a frame rate of 2 frames per second. A WSN with 70 transceivers is set to collect data at a frame rate of 1 frame per second. Table 3.2 shows the values used to create each simulation.

3.7.1 Stationary.

For stationary targets, 1000 realizations are generated for each position. In each realization, 30 seconds of simulated noisy RSS data is generated using AWGN and stacked together to create one averaged frame. Since there are half the number of transceivers in the network configuration with two WSNs compared to the *One* network configuration, there are approximately twice as many frames collected within 30 seconds in the network configuration with two WSNs. Therefore, 60 frames of simulated data is generated for each realization in the network configurations with two WSNs and 30 frames of simulated data is generated for each realization in the *One* network configuration. This process is repeated for each cylindrical human model radius and each σ_n of AWGN in Table 3.2 for each network configuration.

Fig. 3.11 shows an example of a simulated stationary target with $R_T = 1$ ft, where (a) is the truth image, (b) is the simulated attenuation image without any noise added to the RSS links, and (c) is the simulated attenuation image with AWGN added to the RSS links. The red circle represents the location of the target.

45
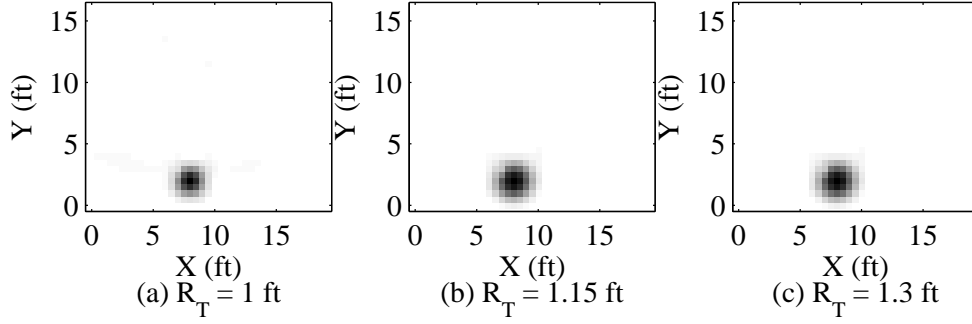
Figure 3.9: Example of attenuation images with different radii for the cylindrical human model without any AWGN added to the RSS links. Each image has a stationary target at position (8,2) ft.
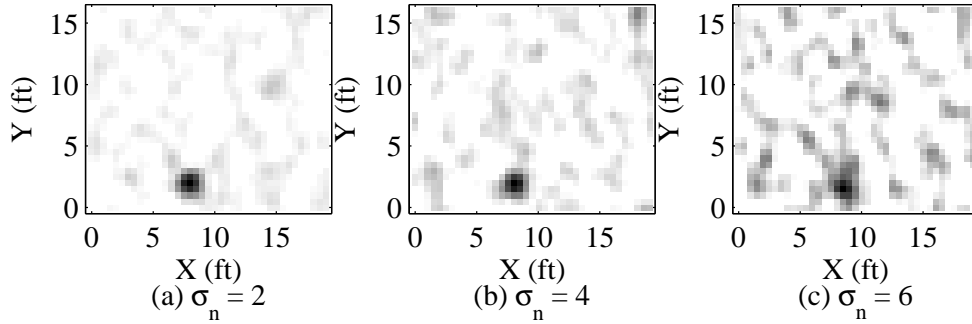

Figure 3.10: Example of attenuation images using AWGN with different σ_n. Each image uses a cylindrical human model of $R_T = 1$ ft and position at (8,2) ft.

3.7.2 Moving.

For moving targets, 100 realizations are generated for each pattern and each speed per network configuration, resulting in 900 total simulated experiments for each network configuration. The process for simulating RSS for a moving target is slightly more complicated than for a stationary target. For a WSN with K transceivers, each transceiver transmits in sequential order and a target may not be in the same position while each transceiver is transmitting. The following steps are performed to simulate RSS for a moving target.

46

Table 3.2: Default values for simulations.

Variable	Value
α	75
σ_n (dB)	2, 4, 6
R_T (ft)	1, 1.15, 1.3

(a) Truth   (b) Sim Without AWGN   (c) Sim With AWGN
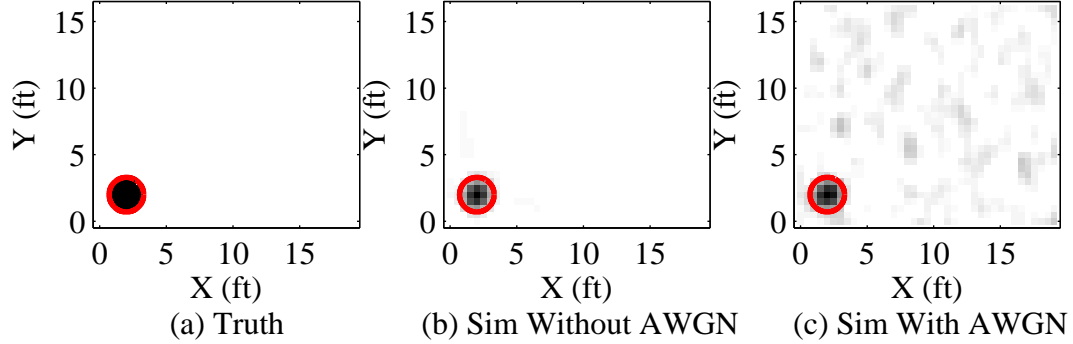
Figure 3.11: Attenuation images from a simulated stationary target. The circle indicates the position of the target at (2,2) ft. The radius of the cylindrical human model is $R_T = 1$ ft and (c) has AWGN of $\sigma_n = 2$ dB.

1. Determine how much distance is traveled between two data frames, which is dependent on number of transceivers within the network and the pace of the target.

2. Divide the distance by the number of transceivers in the network and assign each transceiver (in sequential order) to one of the divided distance.

3. Interpolate a true target position for each transceiver.

4. For each transceiver, generate a truth attenuation image, $\mathbf{x}_T$, for that position using the uniformly attenuating cylindrical human model.

5. Compute $\mathbf{y} = \mathbf{W}\mathbf{x} + \mathbf{n}$ using the appropriate weight matrix, $\mathbf{W}$, for the network configuration, $\mathbf{x}_T$ from step 4, and AWGN for $\mathbf{n}$.

6. Extract RSS, $\mathbf{y}_{tr} \subset \mathbf{y}$, for links only connected to that transceiver.
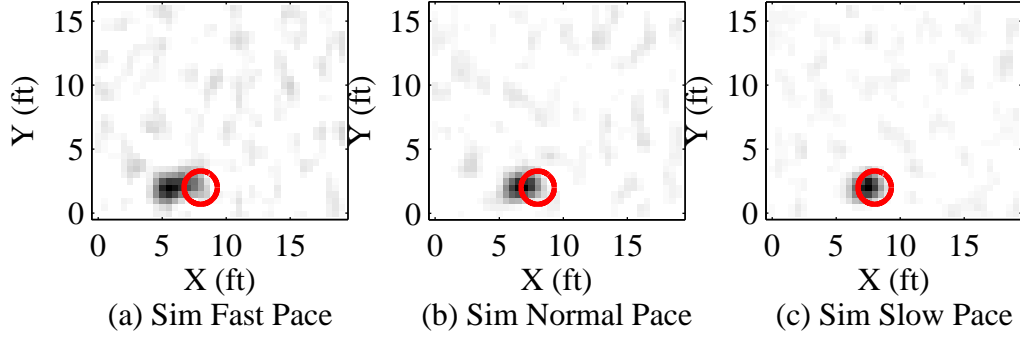
Figure 3.12: Attenuation images from a simulated moving target at various paces. The circle indicates the position of the target at the end of the data frame.

7. Repeat steps 4-6 for every transceiver with the respective true target position for that transceiver.

8. Since each transceiver transmits a RF signal and receives a RSS from another transceiver, there are two RSS for each unique link. Take the average RSS for each unique link.

9. Create a vector of RSS, **y**, for that data frame.

10. Repeat steps 1-9 for every data frame per simulation.

This entire process is repeated for each simulated human radius and each σ_n of AWGN in Table 3.2. Note: These simulations assume there are no lost RSS packets. Lost RSS packets are common with real transceivers and future iterations of this process can incorporate random lost RSS packets.

Fig. 3.12 shows an example of simulated attenuation images for a moving target where (a) is the attenuation image of a target moving at a fast pace, (b) is the attenuation image of a target moving at a normal pace, and (c) is the attenuation image of a target moving at a slow pace. In each image, the position of the target at the end of the data frame is marked by the red circle at (8,2) ft.

48

3.8   Experimental

3.8.1   Equipment and Tools.

TelosB TPR2400.   This research uses Memsic TelosB TPR2400 motes to create one or more WSNs.   The TelosB TPR2400 mote was designed by Crossbow Technology Incorporated (Inc.) and is headquartered in Milpitas, California.   The TelosB mote is an Institute of Electrical and Electronics Engineers (IEEE) 802.15.4 compliant platform with an integrated onboard inverted-F antenna, CC2420 transceiver radio chip, data rate of 250 Kilobits Per Second (kbps), and an 8 Megahertz (MHz) microcontroller with 10 Kilobyte (kB) of Random Access Memory (RAM) [50]. The RF transceiver power ranges from -24 Decibel Milliwatts (dBm) to 0 dBm and has an indoor transmission range of 20 to 30 Meters (m).   The mote is powered by two AA batteries or through the Universal Serial Bus (USB). Data collection and programming the mote are accomplished through the USB. More information regarding the inverted-F antenna can be found in [51] and more information on the TelosB TPR2400 mote can be found in [50]. Fig. 3.13 shows a picture of the TelosB TPR2400.

IEEE 802.15.4.   IEEE 802.15.4 is a standard for low-rate Wireless Personal Area Networks (WPANs). IEEE 802.15.4 based devices are focused on low cost and low power consumption to increase energy efficiency [52], [53]. With an emphasis on keeping the technology as simple as possible with low operating and maintenance costs, IEEE 802.15.4 standard devices are mainly used to create a cheap WSN. IEEE 802.15.4 operates between 2.4 Gigahertz (GHz) and 2.4835 GHz with 16 channels between 11 and 26. Each channel has a carrier frequency in 0.005 GHz increments, starting at 2.405 GHz for Channel 11 and ending at 2.48 GHz for Channel 26. The carrier frequency, f_c, for channel ch can be represented in GHz as [16]

$$f_c = 2.405 + 0.005 \cdot (ch - 11), \quad ch \in [11, 26]. \tag{3.17}$$

Figure 3.13: TelosB TPR2400.

In order to collect data from two WSNs simultaneously without interfering with each other, the transceivers in each WSN are programmed to operate on a different channel. Channel 26 is selected for motes with one WSN, while channels 15 and 20 are selected for motes with two WSNs. These channels are selected because they have the least amount of interference with other signals broadcasting in the test area.

TinyOS. The software used to program the TelosB TPR2400 is TinyOS, an open-source operating system written in NesC [54]. TinyOS started as a research project at the University of California, Berkeley.

Spin. The TelosB TPR2400 uses the *Spin* token protocol developed by the Sensing and Processing Across Networks (SPAN) lab at the University of Utah [55]. *Spin* is an open-source TinyOS program that allows only one mote to transmit at a time, preventing multiple motes in the same network from transmitting a signal at the same time and making the network more robust to lost packets. *Spin* is used to collect RSS data from each network.

RTI Link GUI. A *RTI Link GUI* was originally written in MATLAB® by Dr. Richard K. Martin (Associate Professor of Electrical Engineering at AFIT), Mr. Alex

Folkerts (Southwestern Ohio Council for Higher Education (SOCHE) Intern), and Mr. Tyler Heinl (SOCHE Intern) to collect RSS data from a WSN [29]. A *BaseStation* mote connected to a processing computer is used to collect RSS data from each transmitting transceiver. The GUI parses the data and converts the values to signed integers. Each unique link contains two RSS values for when each transceiver is transmitting a signal. If the data packet is lost in either transceiver when it is transmitting, the GUI solely uses the RSS data available from the other transceiver. If both transceivers fail to transmit a data packet, then no data is available for that unique link. If both transceivers successfully transmit RSS values, the two values are averaged. After every transceiver in the network transmits its RF signal, the GUI outputs one data frame with a vector of RSS and the corresponding time for that data frame. Experiments conducted with only one WSN utilized the *RTI Link GUI* to collect data.

RTI Link GUI v2. For experiments involving two WSNs, a modified version of the *RTI Link GUI* was developed to accommodate for collecting multiple vectors of RSS in different WSNs simultaneously. Two *BaseStation* motes are required for collecting RSS data from two WSNs, where each *BaseStation* mote is programmed to operate under the same channel as the transceivers in its corresponding WSN.

Depending on the network configuration, the combined **W** matrix is generated as outlined in (3.9). The corresponding **Π** matrix is also computed prior to real-time data collection. To generate a combined estimated attenuation image, RSS data from both WSNs must be collected. However, it is highly unlikely that both WSNs will collect one frame of data exactly in the same amount of time. It is also undesirable to force one WSN to wait for the other WSN to finish collecting one frame of data. Therefore, only the time stamps from the first WSN is used while the second WSN continuously outputs its most current vector of RSS data.

Two instances of MATLAB® are used to collect data from each WSN. In the second WSN, the most current vector of RSS data, $\mathbf{y}_2$, is continuously outputted. Whenever the first WSN finishes collecting one full vector of RSS data, the time stamp, t, and vector of RSS data, $\mathbf{y}_1$, from the first WSN is combined with the most current vector of RSS data, $\mathbf{y}_2$, from the second WSN. A third instance of MATLAB® inputs the combined RSS data and generates a combined estimated attenuation image.

Fig. 3.14 shows an example image of the updated GUI, where the top left figure shows the estimated attenuation image for the first WSN, the top right figure shows the estimated attenuation image for the second WSN, the bottom left figure shows the layout of the network configurations, and the bottom right figure shows the combined estimated attenuation image of both WSNs.

Mounting Motes. TelosB motes are attached to 1/2" Polyvinyl Chloride (PVC) pipes at approximately a waist-level height of 3 ft 4 in using double-sided tape fastener. While RSS information is collected through the *BaseStation* mote wirelessly, all motes are powered through USB cables to ensure there is no loss of power during each experiment.

3.8.2 Experiment Design.

A total of 540 experiments are conducted. Three different subjects are tested in this research and each subject conducts three separate moving trials. Each trial consists of the subject moving around the RTI network with the three different patterns and three different paces mentioned in Section 3.6.2, for a total of nine experiments per trial. Each subject also conducts one stationary trial where the subject stands stationary in each of the nine positions mentioned in Section 3.6.1. Network calibration is completed prior to each trial. For each network configuration, 36 experiments are conducted per subject for a total of 108 experiments.

Experiments are conducted in a lab at AFIT. The lab represents somewhat a realistic environment with numerous static objects that causes RF signals to scatter, reflect, and
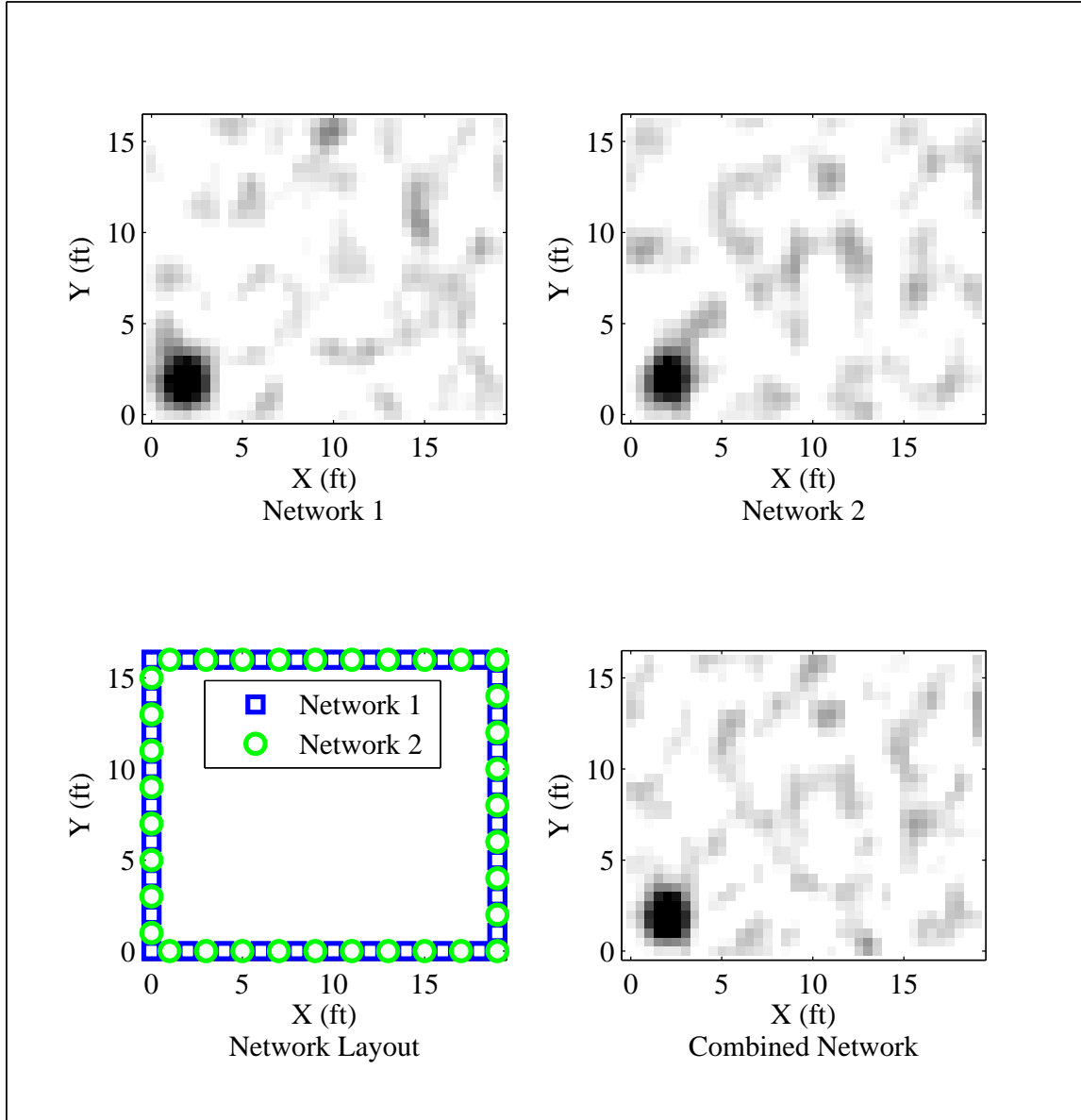
Figure 3.14: Updated *RTI Link GUI* for two WSNs.

diffract [14]. However, transceivers are set up with LOS and no static objects are placed inside the network area to provide the best possible RSS. Fig. 3.15 shows an image of the experimental network configuration for either the *One* network configuration or the *All* network configuration since the locations of the transceivers are the same for both network configurations. Fig. 3.16 shows an image of the *Large* network configuration in the lab.

Fig. 3.17 shows an image of the *Medium* network configuration in the lab. Fig. 3.18 shows an image of the *Small* network configuration in the lab.

For stationary experiments, data is collected for approximately 30 seconds while the target remains stationary at each predetermined position. Table 3.3 shows a summary of the experiments conducted for a stationary target. For experiments where the target is moving around within the network, the subject stands at the initial position of (2,2) ft for 3 seconds before proceeding to allow enough time for the *RTI Link GUI* to initialize. Depending on the pattern and pace, each experiment lasts between 15 seconds and 45 seconds. A metronome is used to ensure the subject moves at the specified pace between each experiment. Table 3.4 shows a summary of the experiments conducted for a moving target.

3.8.3 *Human Subjects.*

This research involved the use of human subjects. Required training was completed by the principal investigator and associate investigators. AFIT RTI protocol was approved by the Air Force Research Laboratory (AFRL) Institutional Review Board (IRB). All test subjects were briefed, signed an Informed Consent Document (ICD), and voluntarily agreed to participate in the experiments prior to entering an active RTI network.

(a) Corner view from (19,0) ft

(b) View from (0,8) ft

Figure 3.15: Experimental *All* and *One* network configurations lab setup.
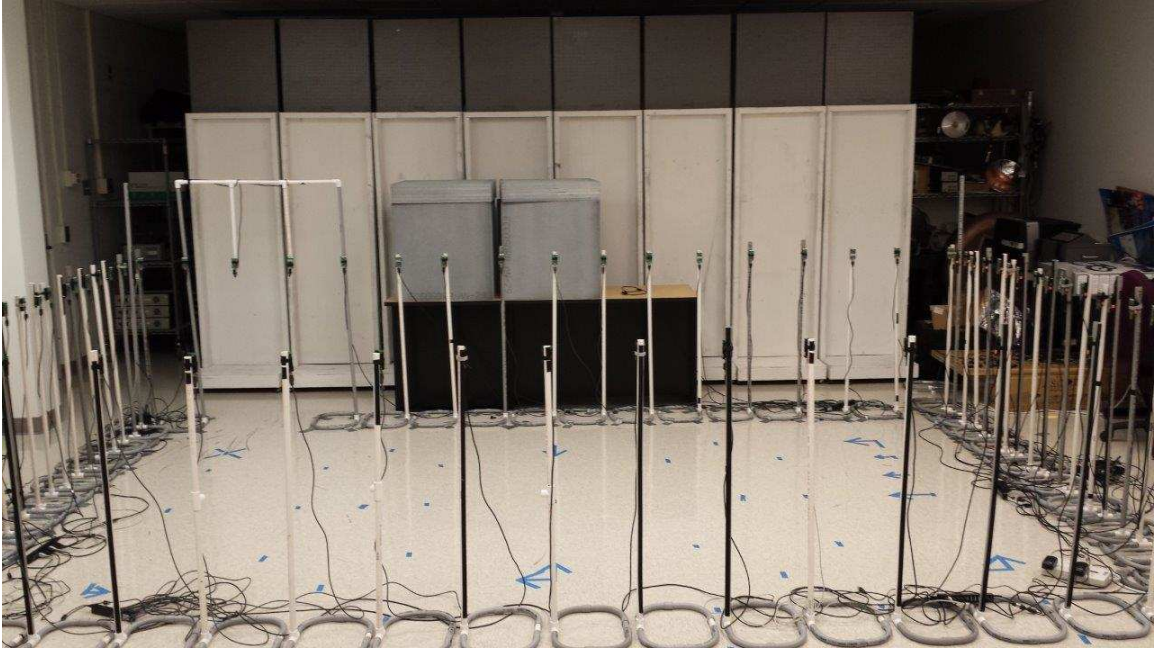
Figure 3.16: Experimental *Large* network configuration lab setup.
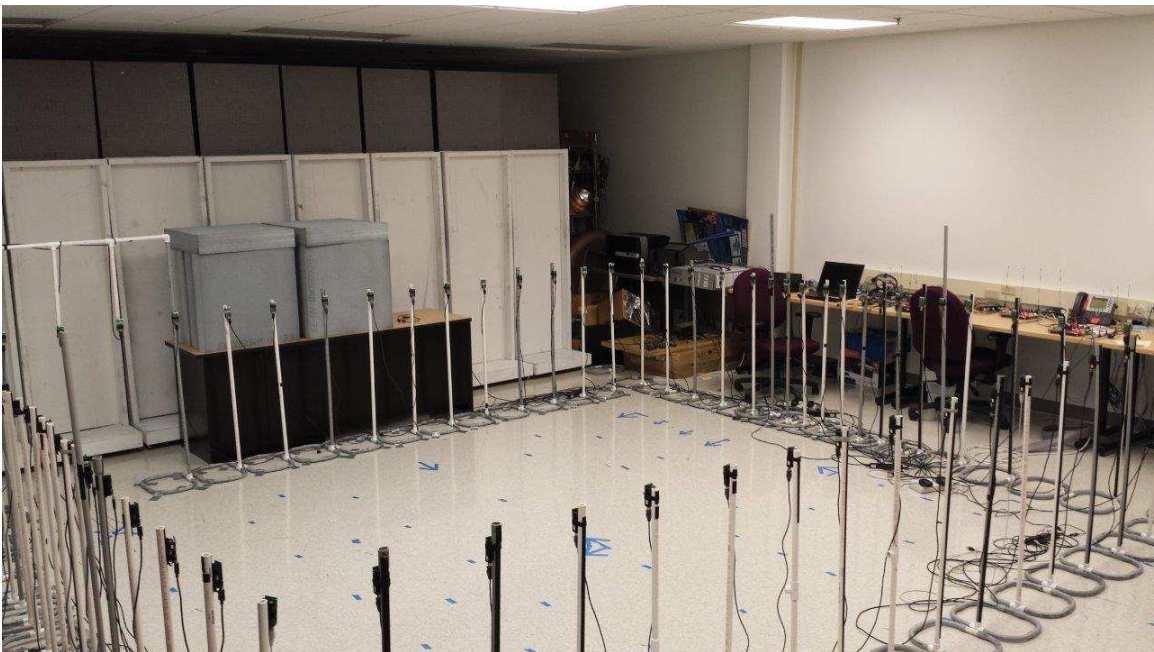
Figure 3.17: Experimental *Medium* network configuration lab setup.
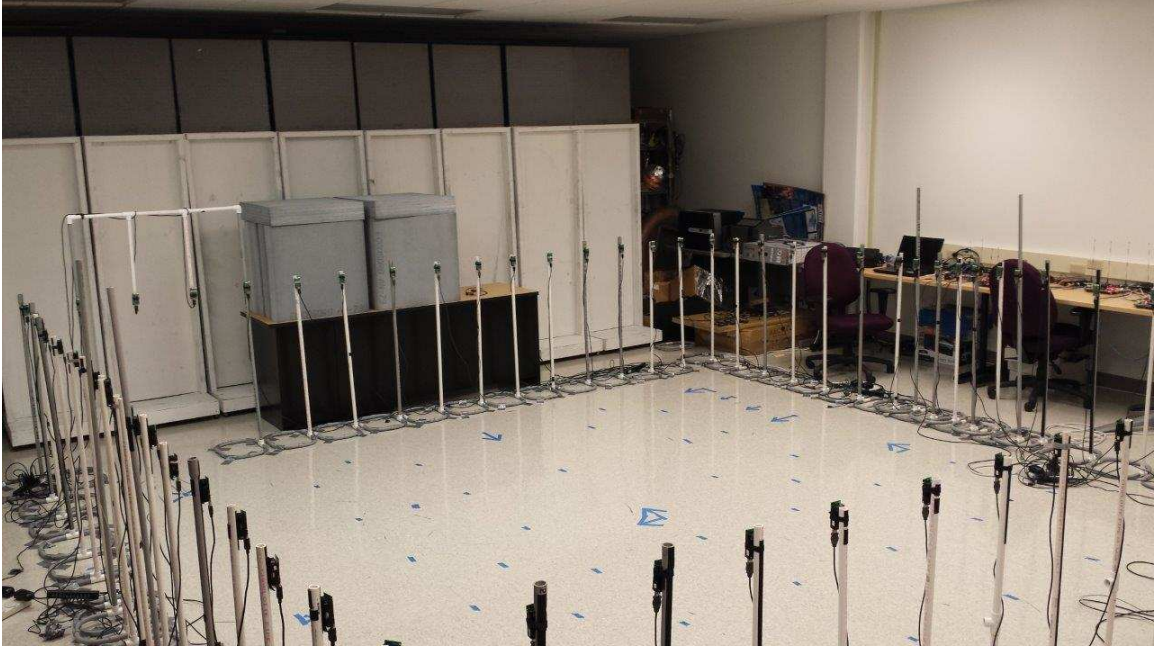
Figure 3.18: Experimental *Small* network configuration lab setup.

Table 3.3: Stationary experiments.

Total # of Experiments	# of Trials Per Target	Position (ft)
15	1	(2,2)
15	1	(2,5)
15	1	(2,8)
15	1	(5,2)
15	1	(5,5)
15	1	(5,8)
15	1	(8,2)
15	1	(8,5)
15	1	(8,8)

Table 3.4: Moving experiments.

Total # of Experiments	# of Trials Per Target	Pattern	Pace
45	3	1	Fast
45	3	1	Normal
45	3	1	Slow
45	3	2	Fast
45	3	2	Normal
45	3	2	Slow
45	3	3	Fast
45	3	3	Normal
45	3	3	Slow

IV. Results and Discussion

THIS chapter presents the results from the simulations and experiments conducted as described in Chapter 3. Stationary and moving targets are tested within each network configuration. Average frame rate, computational complexity, and image quality are used to analyze and characterize each network configuration for both simulations and experimental tests. Position estimates and SNR values are presented to quantify image quality of the attenuation images. Additional comparisons are made between different speeds and different patterns of the target within the WSN(s).

4.1 Frame Rate

Table 4.1 shows the average frame rate of all the experiments conducted for each network configuration. Using a total of 70 transceivers for any network configuration, the network configurations with two WSNs show an average frame rate of approximately 2.22 times faster compared to the network configuration with one WSN.

4.2 Computational Complexity

For each network configuration, the weight matrix and corresponding Π matrix are computed in MATLAB®. The Π matrix is then multiplied with a simulated vector of RSS data to create an estimated attenuation image. Using the *tic* and *toc* commands in MATLAB®, 1000 realizations are generated, timed, and averaged for each network configuration. Table 4.2 shows the average computational time for each network.

Table 4.3 shows the ratio between computational complexity of the *One* network configuration to each of the other network configurations with two WSNs. The theoretical ratios are computed using (3.15) and experimental ratios are computed using the values in Table 4.2.

Table 4.1: Frame Rate for All Experiments.

Network Config	Avg Frame Rate (frames/sec)	Standard Deviation	Min Frame Rate (frames/sec)	Max Frame Rate (frames/sec)
Small	2.23	0.26	0.71	4.02
Medium	2.22	0.28	0.77	4.00
Large	2.19	0.36	0.36	5.81
All	2.25	0.27	0.72	4.00
One	0.86	0.088	0.42	2.79

Table 4.2: Computational complexity results.

Network Config	Avg Comp Time Per Frame (s)	Standard Deviation (s)	# Pixels Per Network	Total # Pixels	Total # Unique Links
Small	2.72	0.036	627	1056	1190
Medium	2.70	0.035	627	924	1190
Large	2.66	0.034	627	660	1190
All	4.52	0.046	1287	1287	1190
One	8.13	0.096	1287	1287	2415

Table 4.3: Ratio of computational complexity.

Ratio with Network Config	Theoretical	Experimental
Small	1.56	2.99
Medium	2.08	3.02
Large	4.29	3.05
All	1.01	1.80

4.3   Image Quality

PSNR, SNR, and RMSE of all estimated attenuation images for each network configuration are discussed in this section. Characterization using these metrics are broken up into 3 categories: stationary, moving by pace, and moving by pattern. For any figures displaying information on RMSE, each plot represents the average RMSE and the error bars represent one standard deviation from the average value. Since PSNR and SNR are presented in dB, each plot represents the median PSNR and median SNR, respectively, and the error bars represent where 68% of the data is contained. This represents roughly one standard deviation, assuming a Gaussian distribution.

4.3.1   Stationary Target.

This section presents the results for all nine stationary positions mentioned in Section 3.6.1 for each network configuration. Fig. 4.1 shows an example of truth, simulated, and experimental attenuation images of a stationary target at the position of (2,2) ft in the *One* network configuration. Different σ_n are simulated for a target with radius R_T = 1.3 ft. Note in Fig. 4.1(f) that the noise experienced with the transceivers in the lab closely resembles the simulated data with σ_n = 4 dB or 6 dB.

4.3.1.1   Simulations.

This section presents the results from simulating a RTI network in MATLAB$^{\circledR}$ with a stationary target at the nine different predefined positions. Even though three different R_T radii and three different σ_n values are simulated as mentioned in Section 3.7, only results with $R_T \in \{1$ ft, 1.3 ft$\}$ and $\sigma_n \in \{2$ dB, 6 dB$\}$ are presented since they represent the low and high values of each variable.

Fig. 4.2 shows the attenuation images for one frame of data of a simulated stationary target at the position of (8,8) ft for each network configuration. The simulated target has R_T = 1 ft and σ_n = 2 dB. Fig. 4.3 presents the same target size of R_T = 1 ft and position at (8,8) ft, but σ_n = 6 dB. Fig. 4.4 shows the attenuation images of a simulated stationary

61

target similar to Fig. 4.3, except all 30 seconds of RSS data per simulated experiment are stacked together and averaged prior to computing an estimated attenuation image.

As can be seen between Fig. 4.2 and Fig. 4.3, the amount of noise within the RTI network can greatly affect the ability of the network to accurately determine the true position of the target. More specifically, attenuation images in networks with fewer communication links traversing through the area where the target is located, such as the *S mall* and *Medium* network configurations, may be unable to consistently discern between a target and noise. However, Fig. 4.4 shows that noise can greatly be reduced in the estimated attenuation image if it is possible to stack multiple frames of RSS data together.
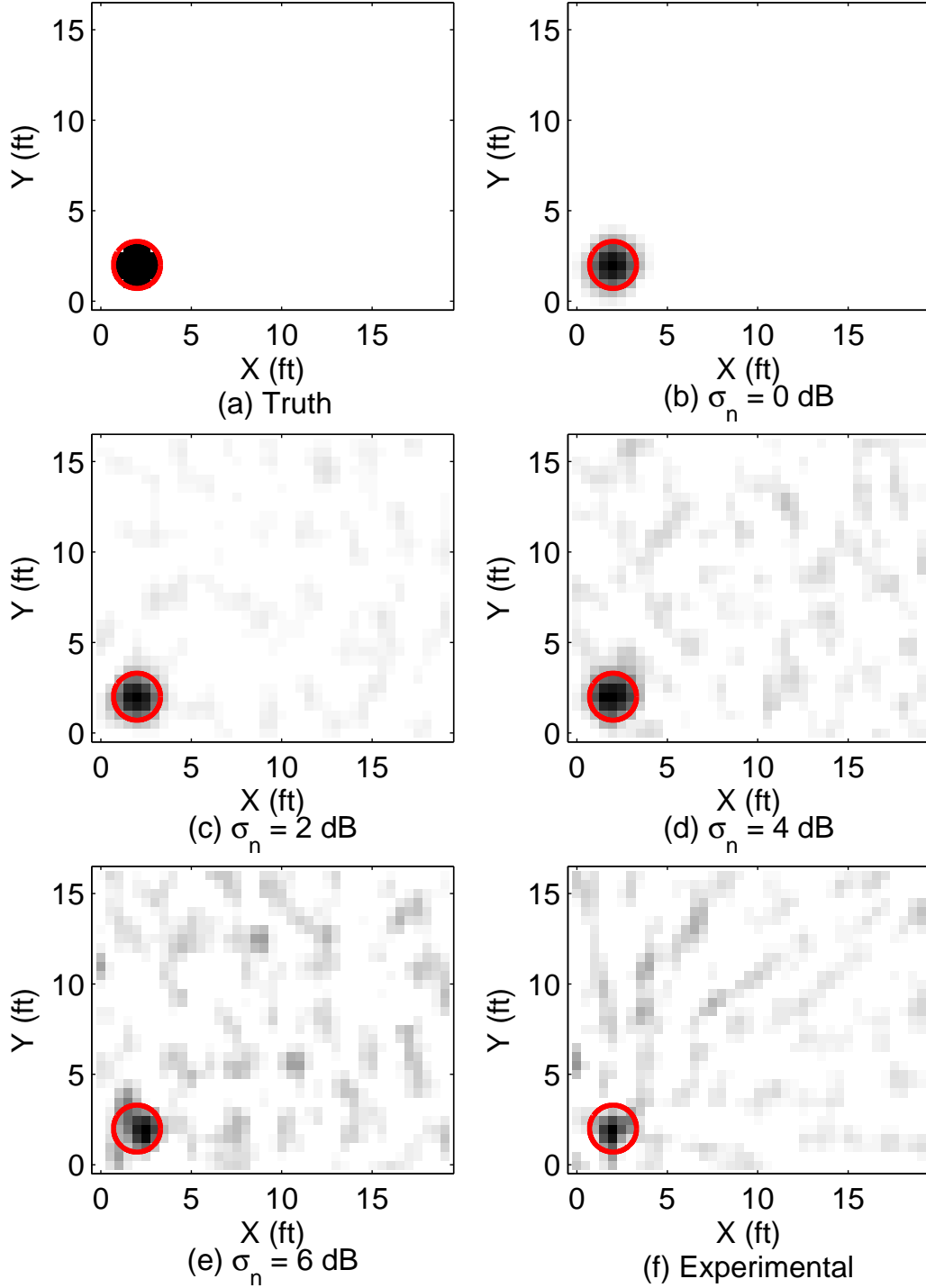
Figure 4.1: Example comparison of attenuation images for a stationary target at (2,2) ft in the *One* network configuration. The circle marks the true position of the target. Attenuation image in (a) represents the truth attenuation image with $R_T = 1.3$ ft. Attenuation images in (b), (c), (d), and (e) are simulated images with $R_T = 1.3$ ft and different σ_n. Attenuation image in (f) is from experimental data.
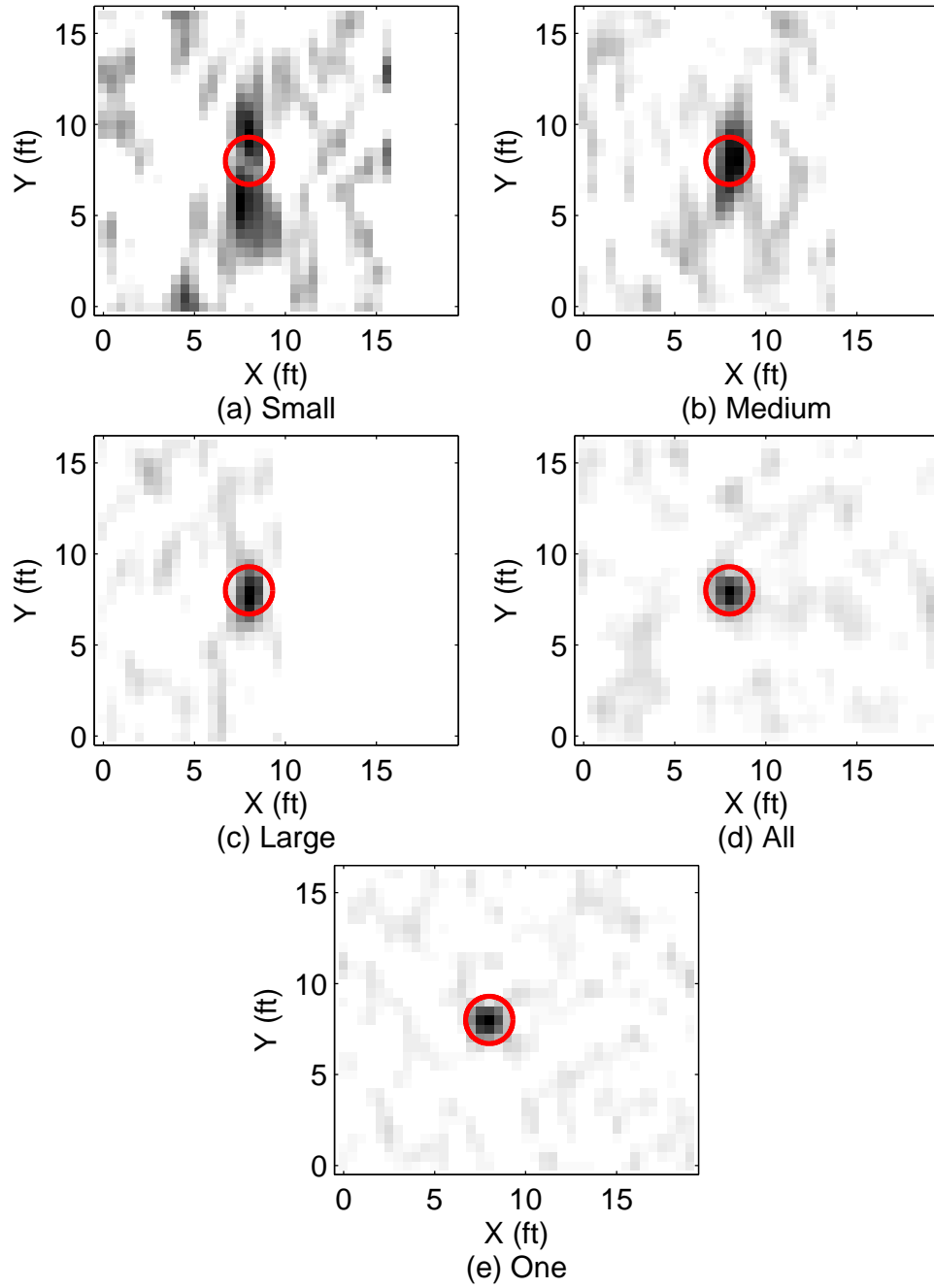
Figure 4.2: Attenuation images from one frame of data of a simulated stationary target at the position of (8,8) ft. $R_T = 1$ ft and $\sigma_n = 2$ dB. The circle marks the true position of the target.
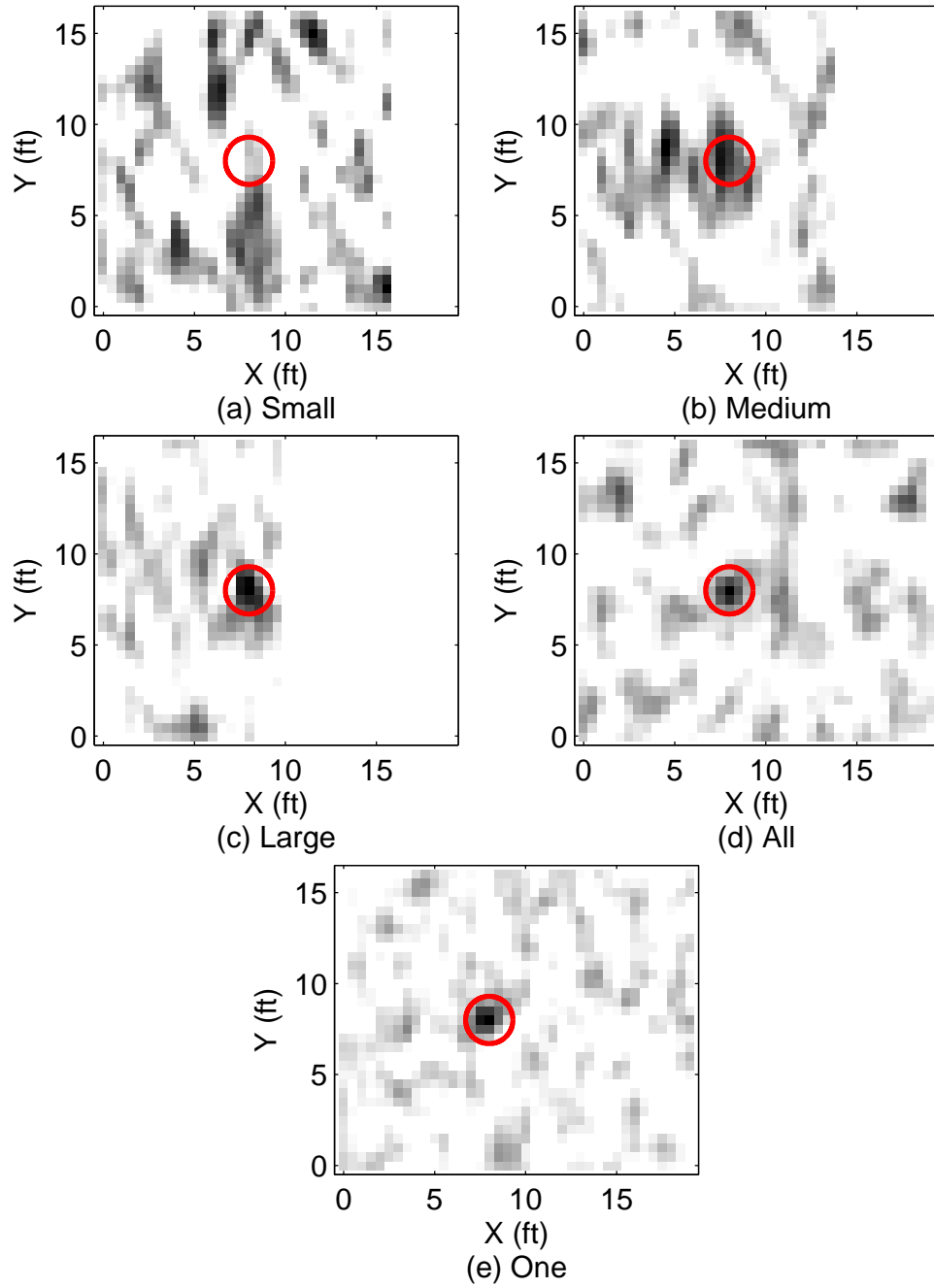
Figure 4.3: Attenuation images from one frame of data of a simulated stationary target at the position of $(8,8)$ ft. $R_T = 1$ ft and $\sigma_n = 6$ dB. The circle marks the true position of the target.
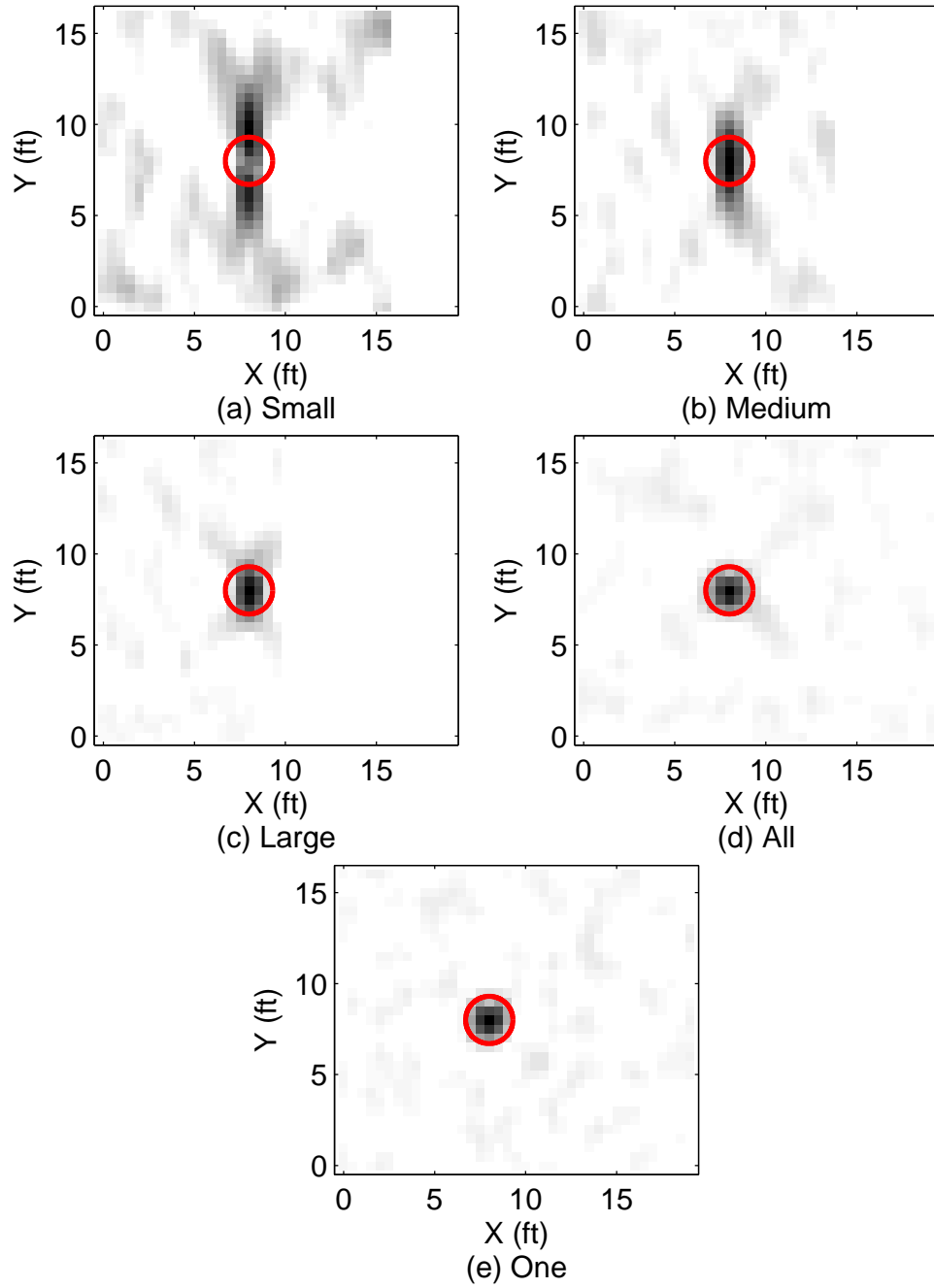
Figure 4.4: Attenuation images from a stacked data of a simulated stationary target at the position of (8,8) ft. $R_T = 1$ ft and $\sigma_n = 6$ dB. The circle marks the true position of the target.

Figs. 4.5–4.8 show the median PSNR in (a) and median SNR in (b) of a simulated stationary target for all realizations of all nine stationary positions for each network configuration. Figs. 4.9–4.12 show the average RMSE of a simulated stationary target for all realizations of all nine stationary positions for each network configuration. Position estimation using the maximum intensity value within the attenuation image is shown in (a), position estimation using 1-D projection is shown in (b), and position estimation using the Gaussian kernel to smooth the attenuation image prior to finding the maximum intensity value is shown in (c).

Looking at Figs. 4.5–4.8, the median PSNR and SNR increases as there are more overlap between two WSNs. In all network configurations with two WSNs, the median PSNR and SNR of the combined image is always higher than each individual network image. The *One* network configuration has the highest median PSNR and SNR, which is expected since the target is stationary and there are approximately twice as many unique links within the *One* network configuration over the other network configurations. Note that when $R_T = 1$ ft, PSNR and SNR decreases as σ_n increases. However, when $R_T = 1.3$ ft, there is little change in PSNR and SNR per network configuration as σ_n changes.

Looking at Figs. 4.9–4.12, the average RMSE decreases as there is more overlap between two WSNs. Average RMSE using 1-D projection estimation in the *One* network configuration is slightly greater than the *All* network configuration when $\sigma_n = 6$ dB. Aside from this, position estimation is perfect for the *All* and *One* network configurations, regardless of R_T, σ_n, and position estimation technique. The Gaussian estimation technique provides similar average RMSE as the maximum intensity value estimation technique. The 1-D projection estimation technique has the highest average RMSE compared to the other estimation techniques. Also, aside from the *Small* network configuration, the RMSE for the combined image is always lower than each individual network.
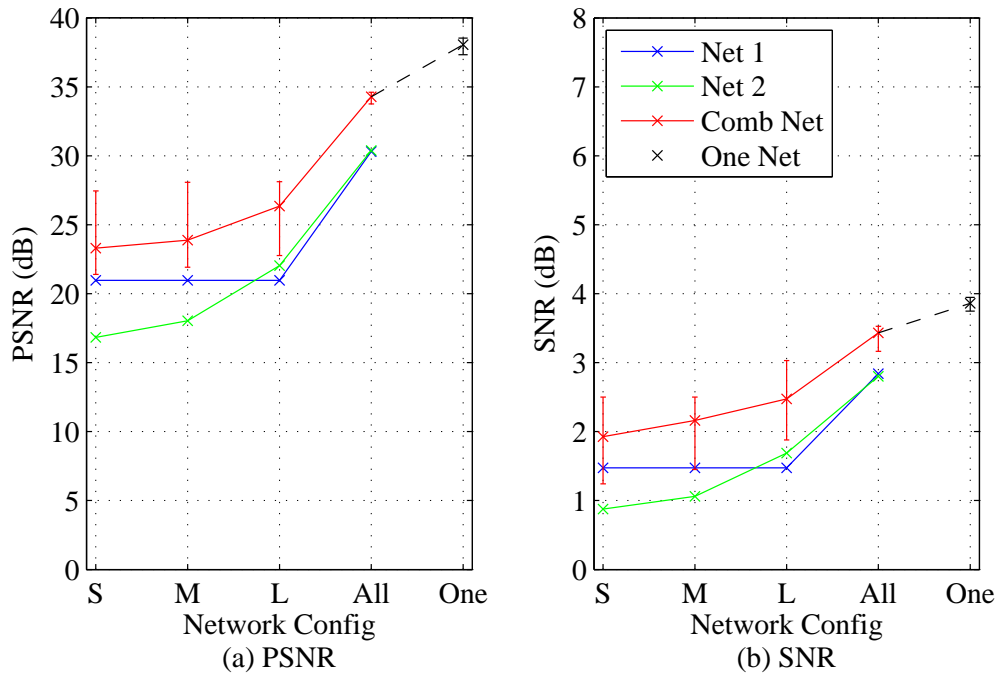
Figure 4.5: Median PSNR and SNR of simulated stationary target for each network configuration. $R_T = 1$ ft and $\sigma_n = 2$ dB.
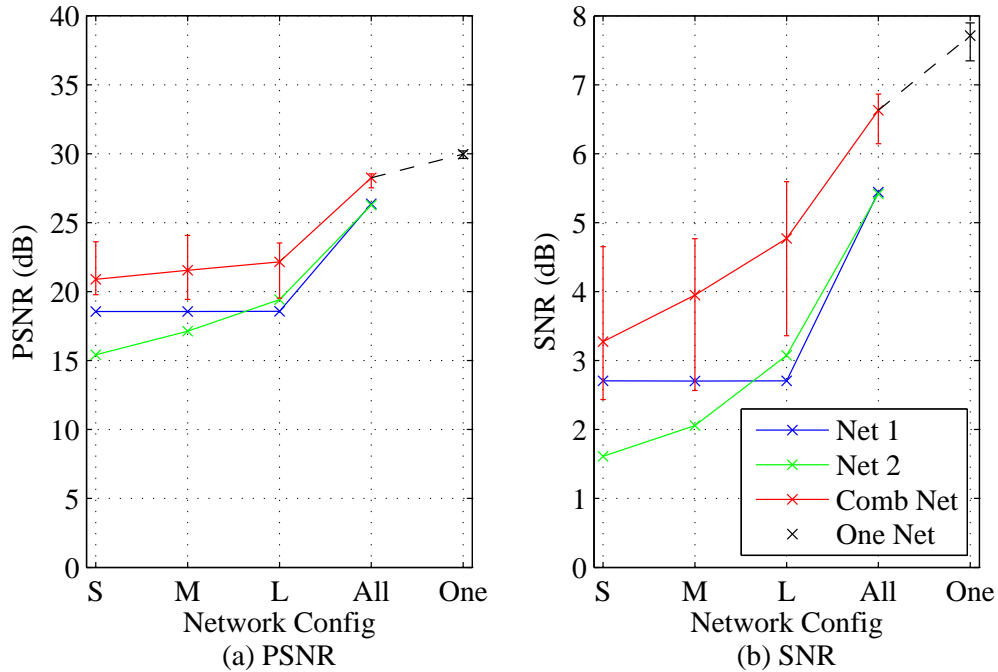
Figure 4.6: Median PSNR and SNR of simulated stationary target for each network configuration. $R_T = 1.3$ ft and $\sigma_n = 2$ dB.
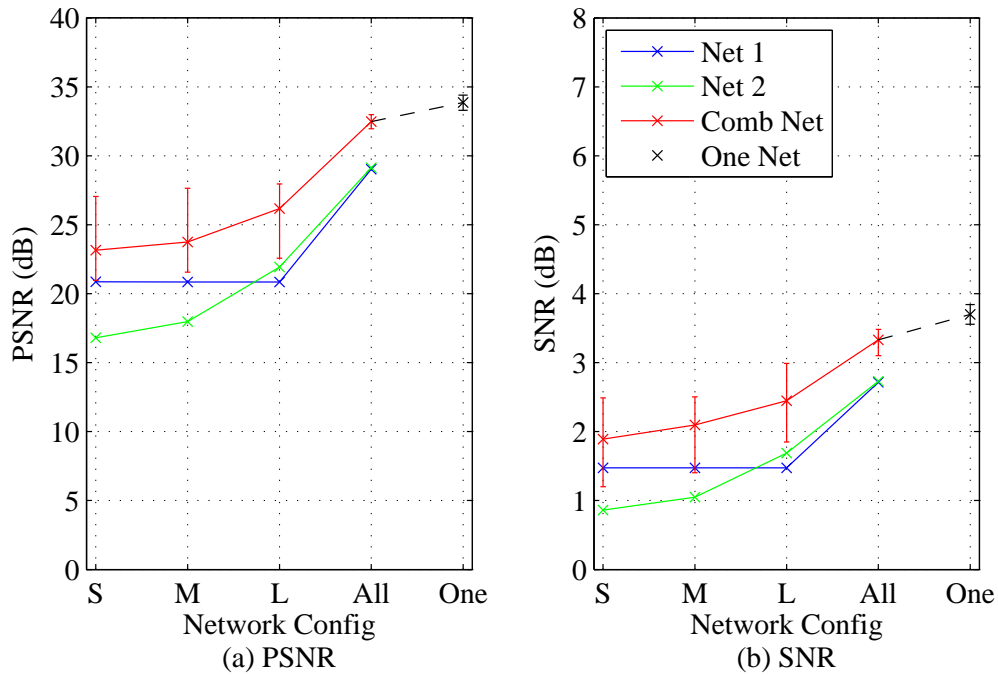
Figure 4.7: Median PSNR and SNR of simulated stationary target for each network configuration. $R_T = 1$ ft and $\sigma_n = 6$ dB.
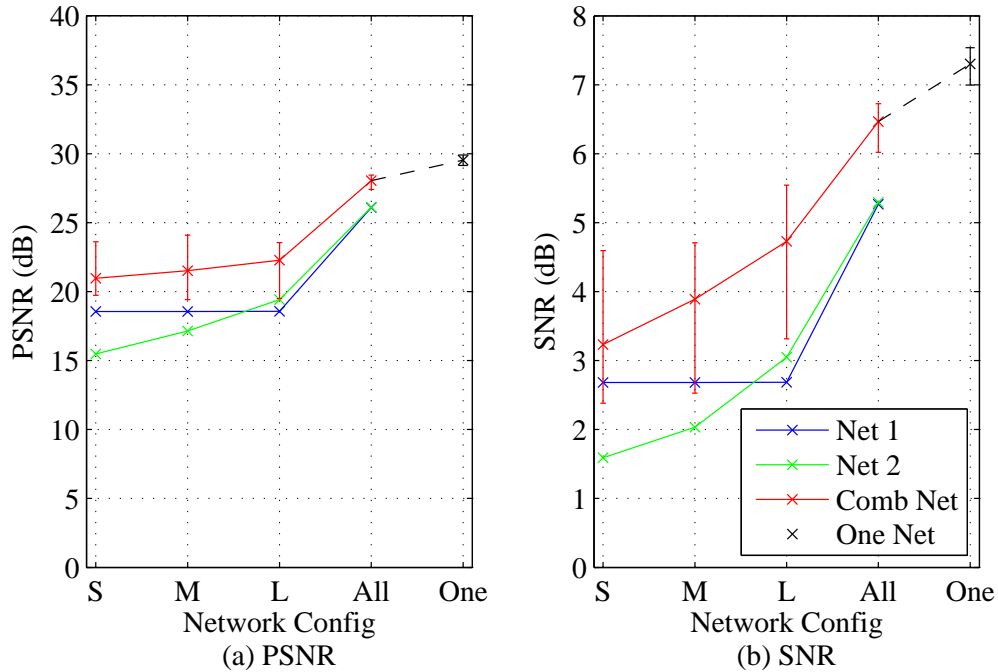
Figure 4.8: Median PSNR and SNR of simulated stationary target for each network configuration. $R_T = 1.3$ ft and $\sigma_n = 6$ dB.
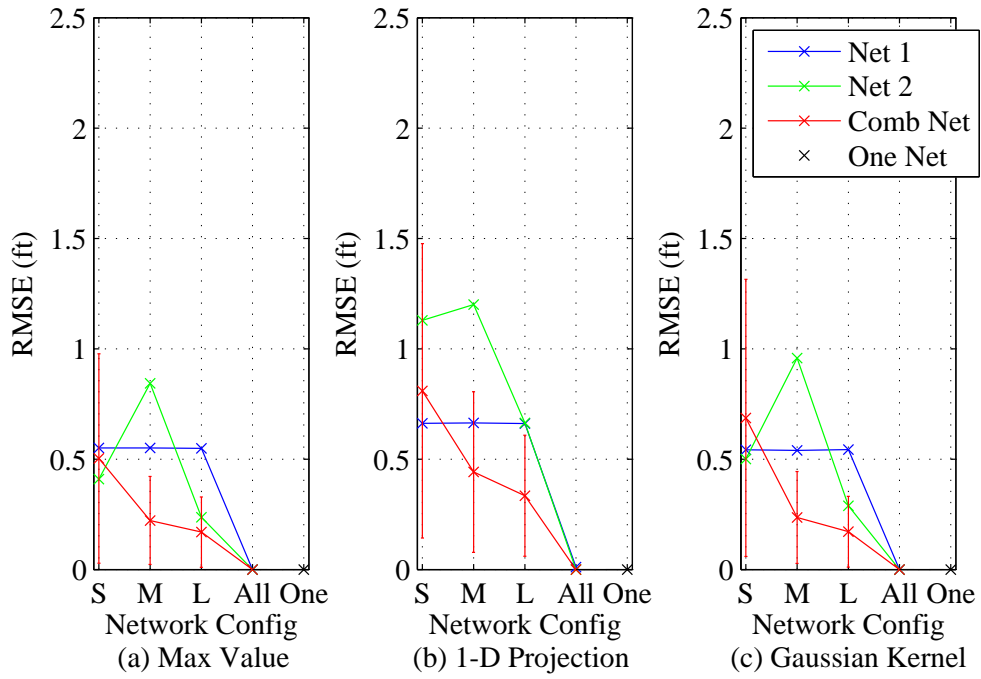
Figure 4.9: Average RMSE of simulated stationary target for each network configuration for each position estimation technique. $R_T = 1$ ft and $\sigma_n = 2$ dB.
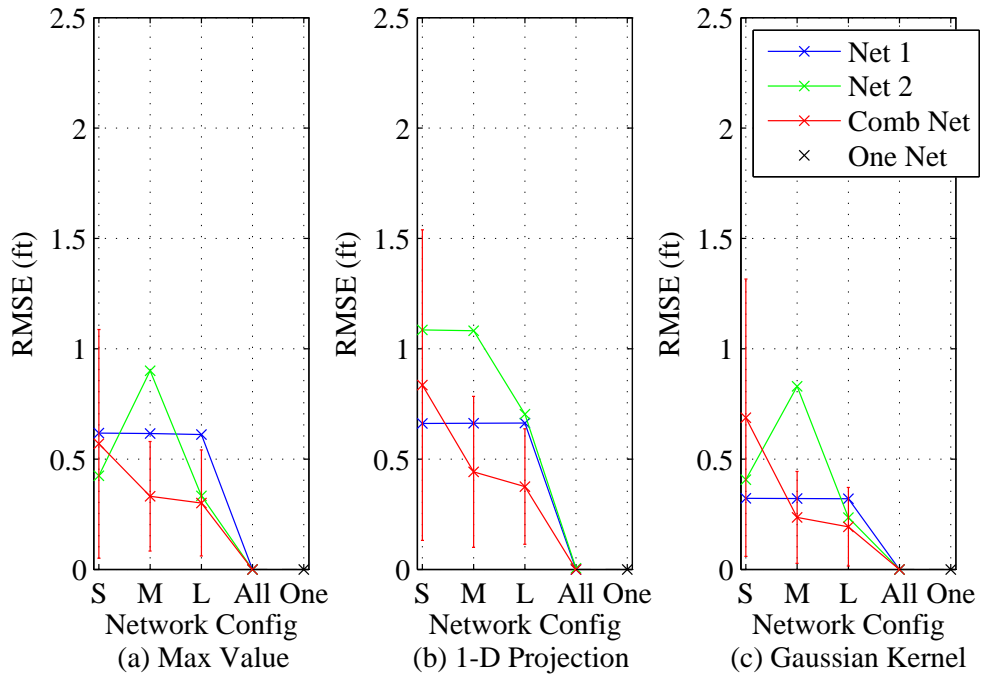
Figure 4.10: Average RMSE of simulated stationary target for each network configuration for each position estimation technique. $R_T = 1.3$ ft and $\sigma_n = 2$ dB.
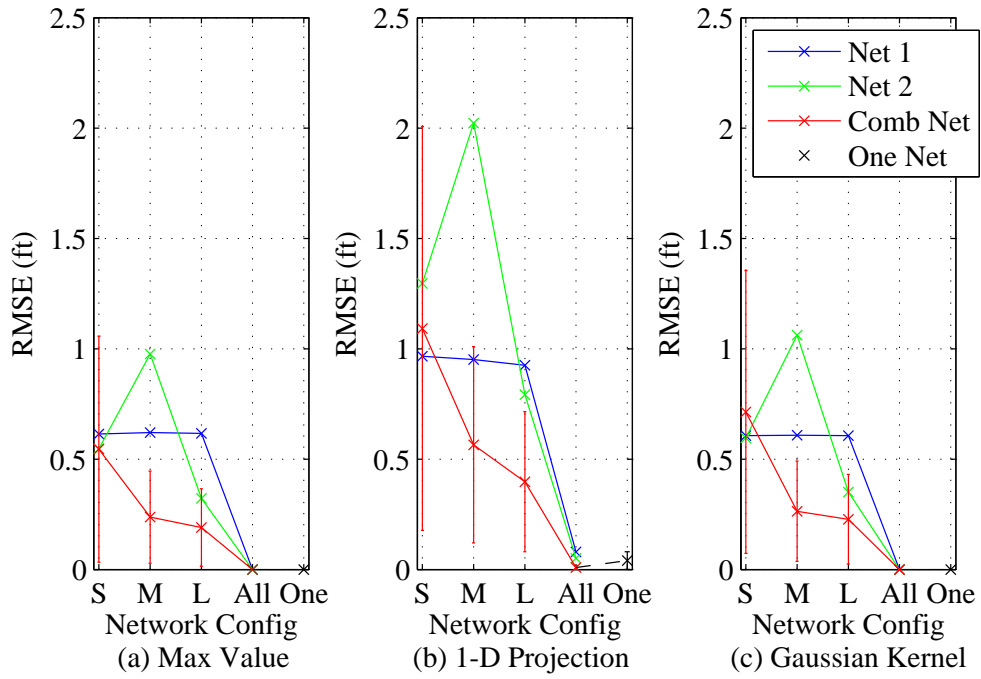
Figure 4.11: Average RMSE of simulated stationary target for each network configuration for each position estimation technique. $R_T = 1$ ft and $\sigma_n = 6$ dB.
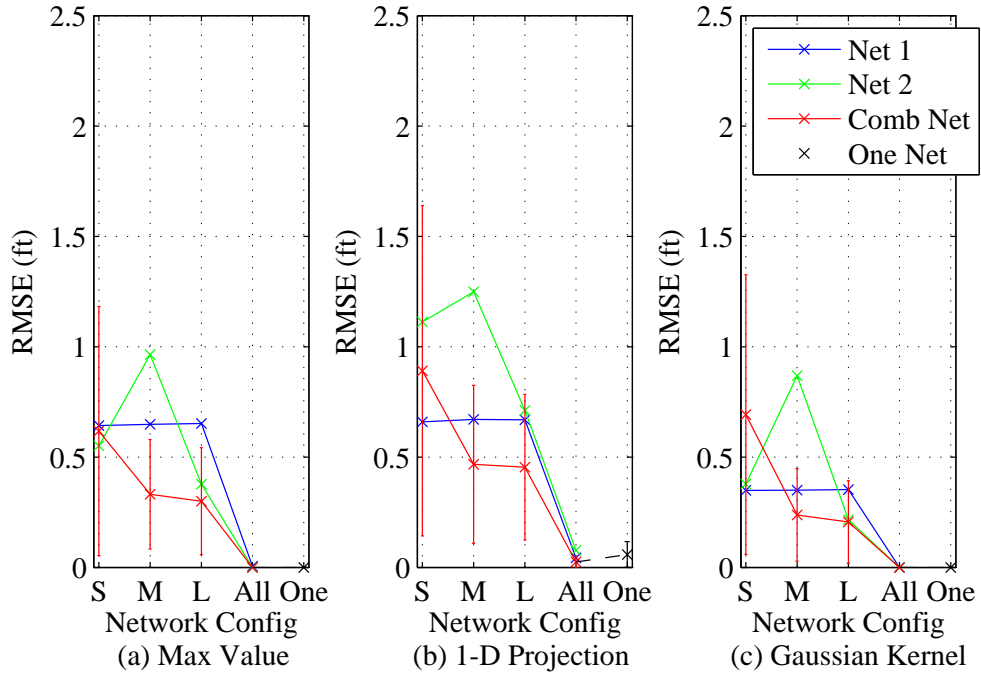
Figure 4.12: Average RMSE of simulated stationary target for each network configuration for each position estimation technique. $R_T = 1.3$ ft and $\sigma_n = 6$ dB.

4.3.1.2 Experimental.

This section present results from experimental stationary targets. Fig. 4.13 and Fig. 4.14 show examples of attenuation images from a stacked data of RSS values for a stationary target. In Fig. 4.13, the target stands by the edge of the network at (2,5) ft. In Fig. 4.14, the target stands close to the center of the area at (8,8) ft.

Fig. 4.15 shows the median PSNR in (a) and median SNR in (b) of all experimental stationary target data for all nine stationary positions for each network configuration. In all network configurations with two WSNs, the median PSNR and SNR of the combined image is always higher than each individual network image. The median PSNR follows the same trend as simulated data where the PSNR increases as there is more overlap between two WSNs. SNR also generally follows the same trend, except the difference in median SNR between each network configuration is less than 1 dB. Also, the *Large* network configuration has a slightly higher SNR than the *All* and *One* network configurations.

Fig. 4.16 shows the average RMSE of all experimental stationary target data for all positions for each network configuration. Position estimation using the maximum intensity value within the attenuation image is shown in (a), position estimation using 1-D projection is shown in (b), and position estimation using the Gaussian kernel to smooth the attenuation image prior to finding the maximum intensity value is shown in (c). Except for the 1-D projection estimation technique, the average RMSE decreases as there is more overlap between the two WSNs. The *One* network configuration has the lowest average RMSE. The RMSE using the 1-D projection estimation typically has the highest average RMSE in comparison to the other two estimation techniques. The Gaussian estimation technique provides a slightly better, if not the same, average RMSE as the maximum intensity value estimation. Finally, the average RMSE for the combined network image is always lower than that of each individual network.
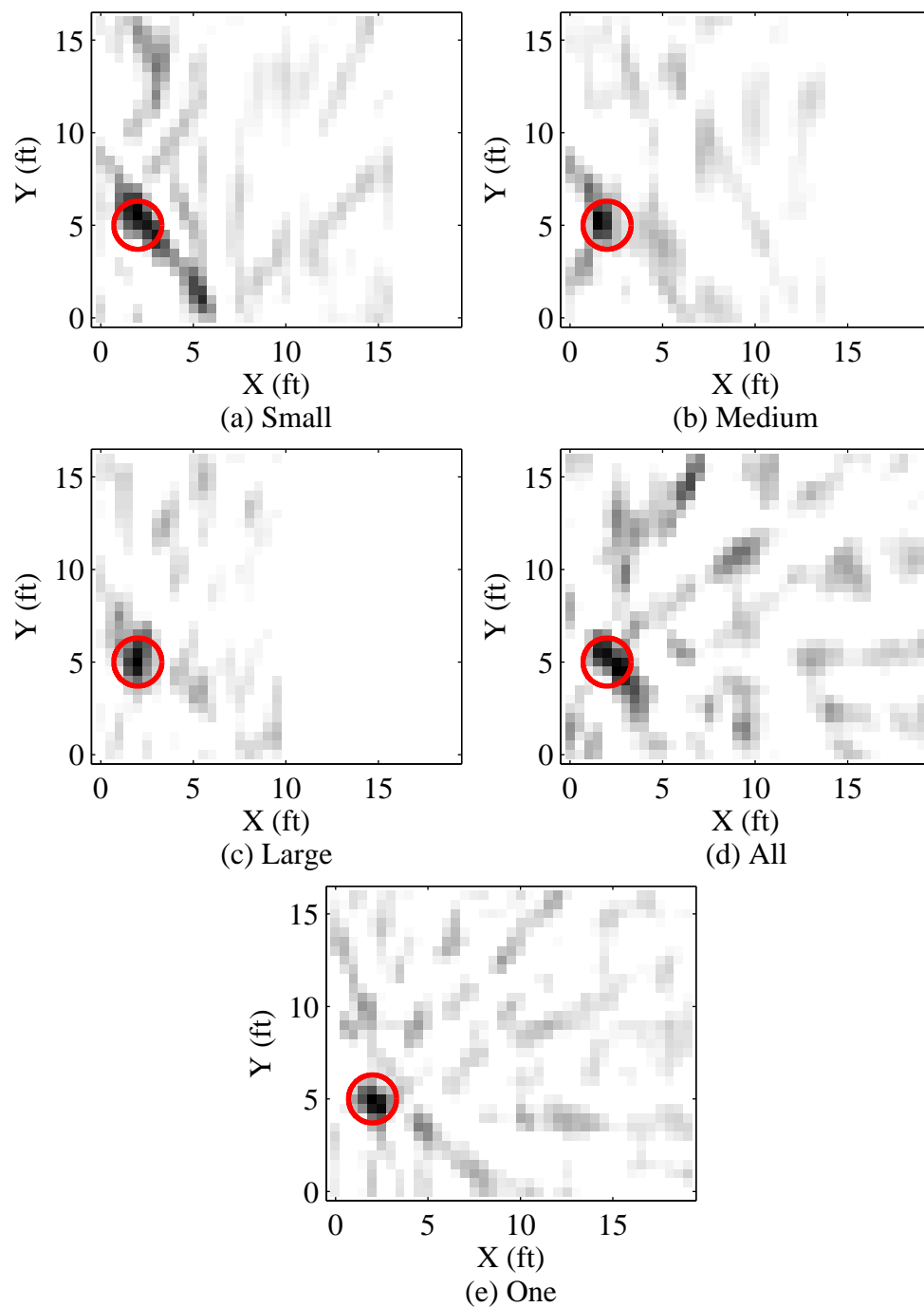
Figure 4.13: Attenuation images from a stacked data of a stationary target at the position of (2,5) ft. The circle marks the true position of the target.
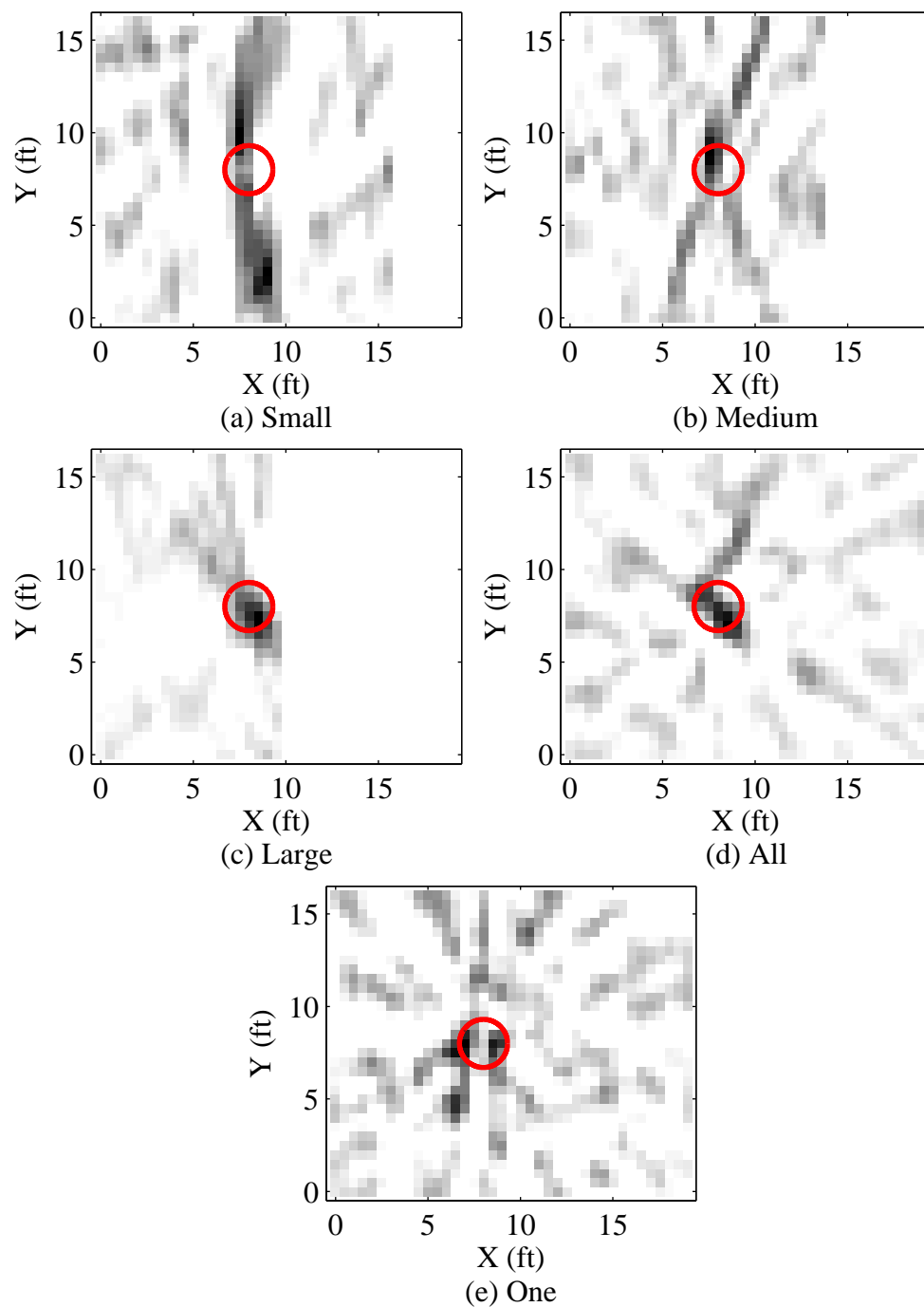
Figure 4.14: Attenuation images from a stacked data of a stationary target at the position of (8,8) ft. The circle marks the true position of the target.
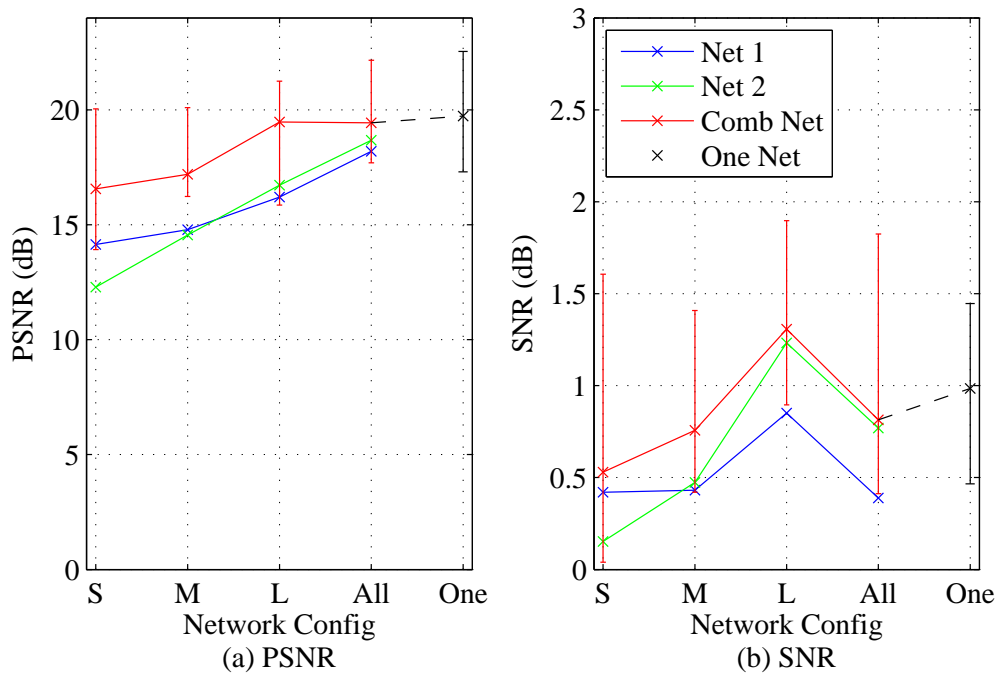
Figure 4.15: Median PSNR and SNR of all experimental stationary target data.
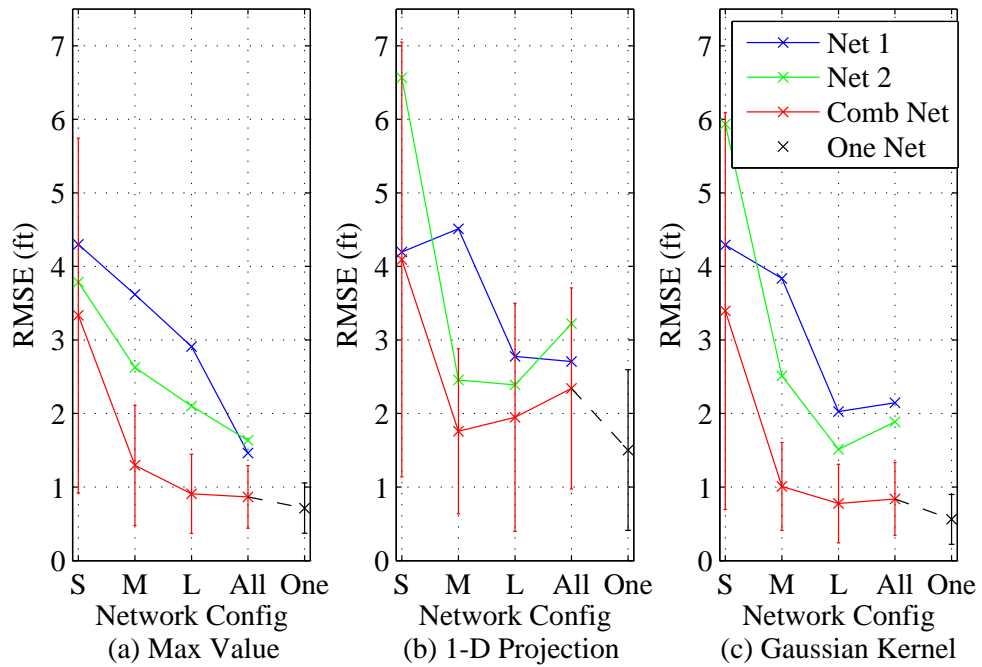
Figure 4.16: Average RMSE of all experimental stationary target data for each position estimation technique.
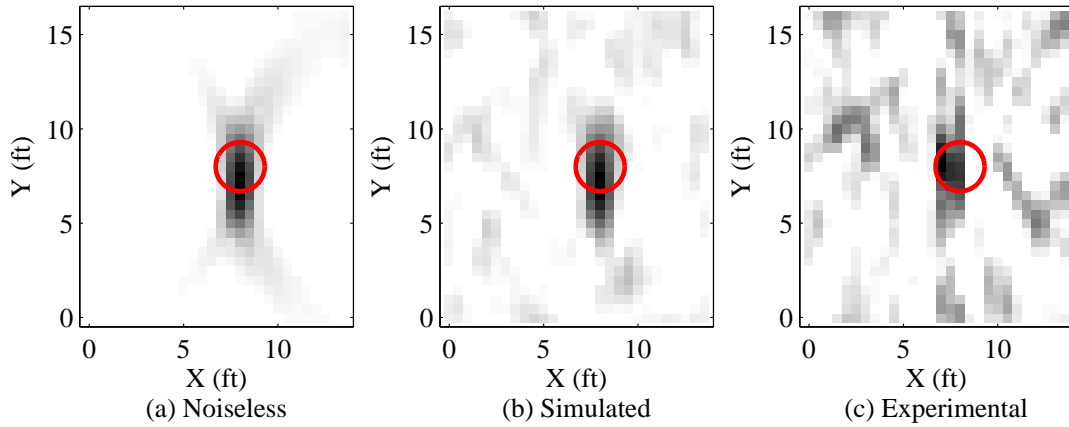
Figure 4.17: Example of (a) a noiseless attenuation image of a simulated moving target with $R_T = 1.3$ ft, (b) estimated attenuation image from simulated RSS data with $R_T = 1.3$ ft and $\sigma_n = 2$ dB, and (c) estimated attenuation image from experimental data for a target moving at a fast pace in the *Medium* network configuration. The circle marks the true position of the target.

4.3.2   *Moving by Pace.*

This section presents the results of moving target data for each of the three different paces mentioned in Section 3.6.2.1. Fig. 4.17 shows an example of a noiseless simulated attenuation image of a moving target applying the process described in Section 3.7. An estimated attenuation image from simulated data and an estimated attenuation image from experimental data of a target moving at a fast pace is shown as well in Fig. 4.17.

4.3.2.1   *Simulations.*

This section presents the results from simulating a RTI network in MATLAB® with a moving target. Fig. 4.18 shows an example of the estimated attenuation images of a simulated moving target at a fast pace for each network configuration. The position of the target is at (8,5) ft for this data frame. The simulated target has a radius of $R_T = 1$ ft and the circle marks the true position of the target. Note that instead of a dark circular spot where the target is located as in simulated stationary results, there is a dark oval-like shape. This

is a result of the target not being at the same position while each transceiver is transmitting its RF signal.

Figs. 4.19–4.22 show the median PSNR of a simulated moving target for all 900 realizations with respect to pace. Similar to stationary results, the median PSNR of the combined network image is always higher or the same than each individual network. Also, the median PSNR increases as there is more overlap between two WSNs. The median PSNR also increases as the pace of the target decreases. The *One* network configuration provides the best PSNR when the target is moving at a slow pace. However, PSNR in the *All* network configuration is either similar or higher than the *One* network configuration when the target is moving at the normal or fast pace. Finally, PSNR decreases as σ_n increases.

Figs. 4.23–4.26 show the median SNR of a simulated moving target for all 900 realizations with respect to pace. The median SNR when $\sigma_n = 2$ dB follows the same trend as stationary results and increases as there is more overlap between two WSNs. However, the median SNR is similar to each other regardless of the network configuration when $\sigma_n = 6$ dB. With respect to pace, there is no discernible trend in SNR for simulated moving data between network configurations for different R_T and σ_n.

Figs. 4.27–4.30 show the average RMSE of a simulated moving target for all 900 realizations with respect to pace using the maximum intensity value estimation technique. Figs. 4.31–4.34 show the average RMSE of a simulated moving target for all 900 realizations with respect to pace using the 1-D projection estimation technique. Figs. 4.35–4.38 show the average RMSE of a simulated moving target for all 900 realizations with respect to pace using the Gaussian kernel to smooth the attenuation image prior to finding the maximum intensity value. The average RMSE remains relatively low when $\sigma_n = 2$ dB. Regardless of the estimation technique, average RMSE is under 1.5 ft when $\sigma_n = 2$ dB, and trends downward as there is more overlap between two WSNs. Position estimation becomes more accurate as the pace of the target is slower. When $\sigma_n = 2$ dB, the *All* network

configuration generally has the best position estimates and lowest average RMSE out of all the network configurations, followed by a mix between the *Large* and *One* network configurations. Average RMSE is higher at $\sigma_n = 6$ dB than $\sigma_n = 2$ dB. However, the change in RMSE is not as profound when $R_T = 1.3$ ft. For $\sigma_n = 6$ dB, the maximum intensity value and Gaussian estimation technique provides an average RMSE of up to 3 ft when $R_T = 1$ ft and under 1.5 ft when $R_T = 1.3$ ft. The 1-D projection estimation technique provides the highest average RMSE out of the three estimation techniques. When $R_T = 1$ ft and $\sigma_n = 6$ dB, the average RMSE is over 4 ft using the 1-D projection estimation technique. While also higher, the maximum intensity value estimation technique is still able to provide estimates with an average RMSE of under 3 ft and Gaussian estimation technique with an average RMSE of under 2 ft when $R_T = 1$ ft and $\sigma_n = 6$ dB.
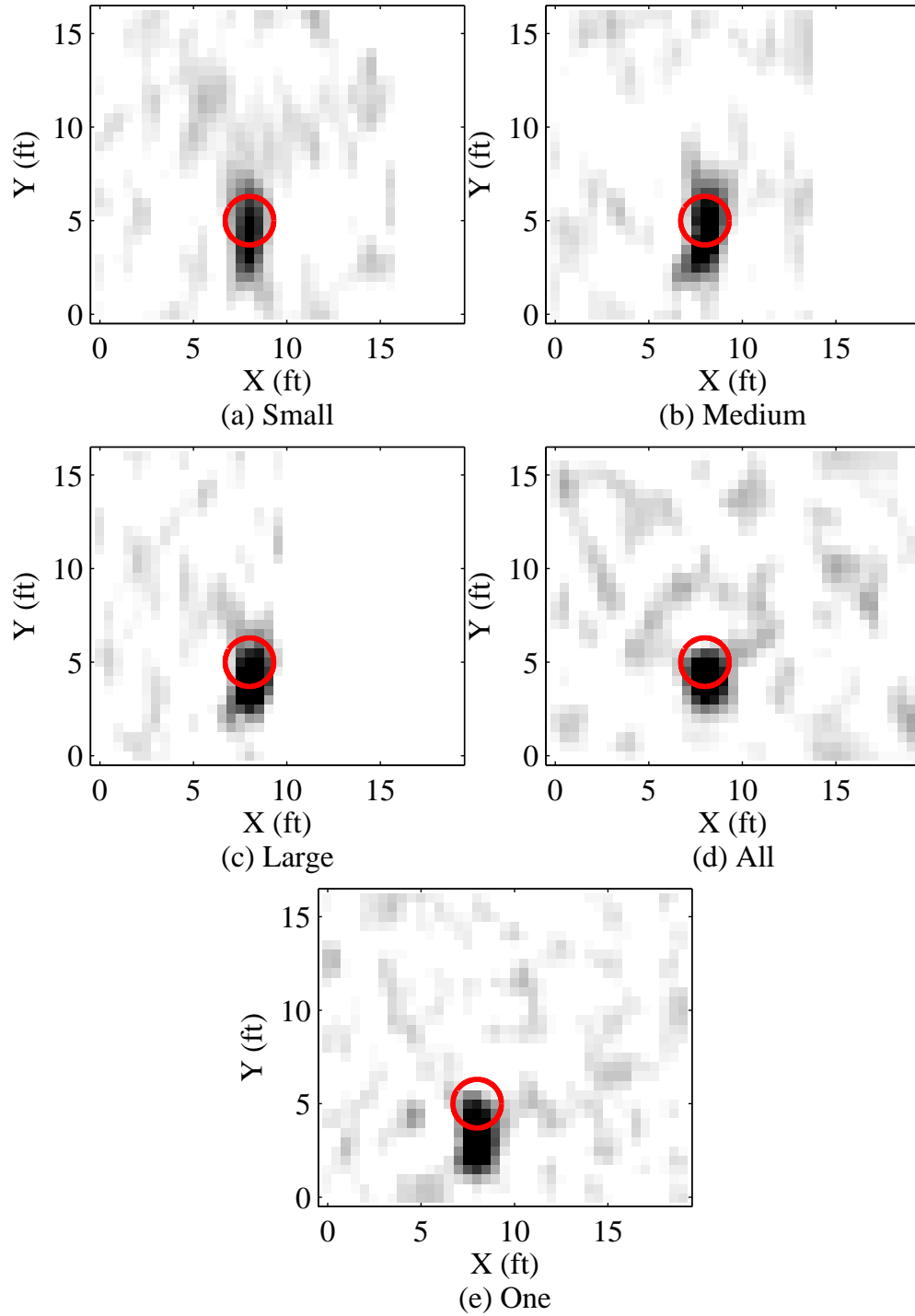
Figure 4.18: Attenuation images of a simulated moving target at a fast pace. Current position of target is (8,5) ft for this frame of data. $R_T = 1$ ft and $\sigma_n = 2$ dB. The circle marks the true position of the target.
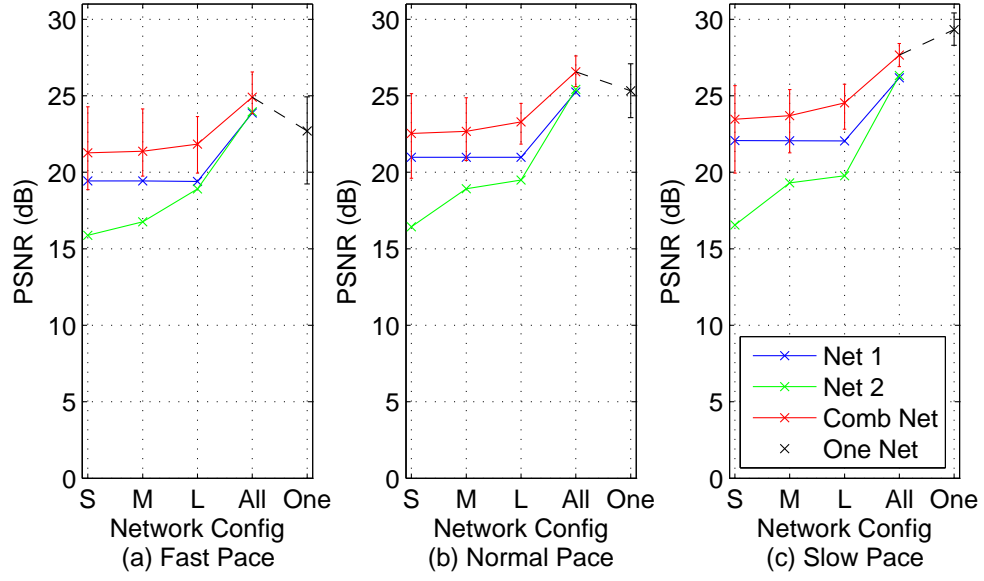
Figure 4.19: Median PSNR of simulated moving target by pace. $R_T = 1$ ft and $\sigma_n = 2$ dB.
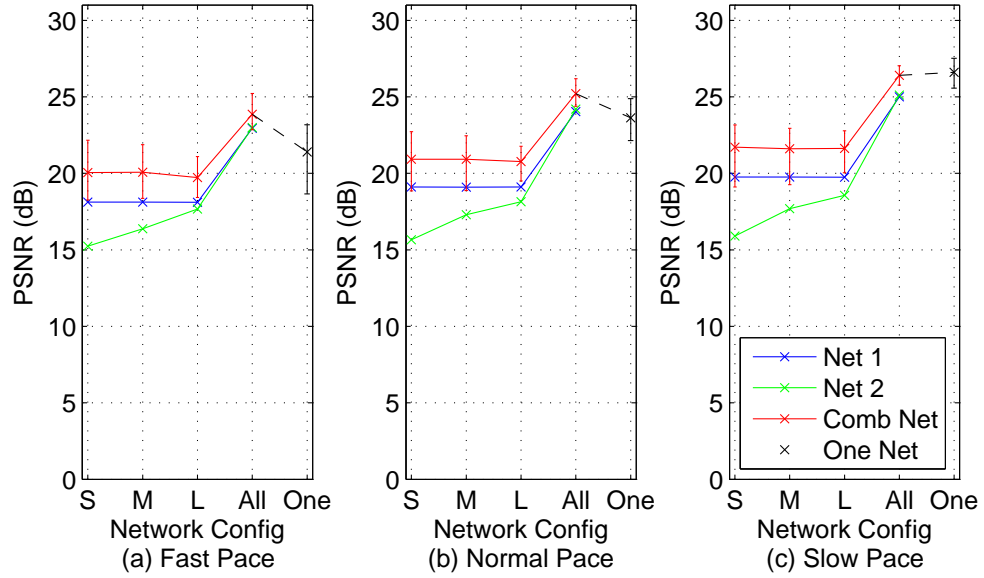
Figure 4.20: Median PSNR of simulated moving target by pace. $R_T = 1.3$ ft and $\sigma_n = 2$ dB.
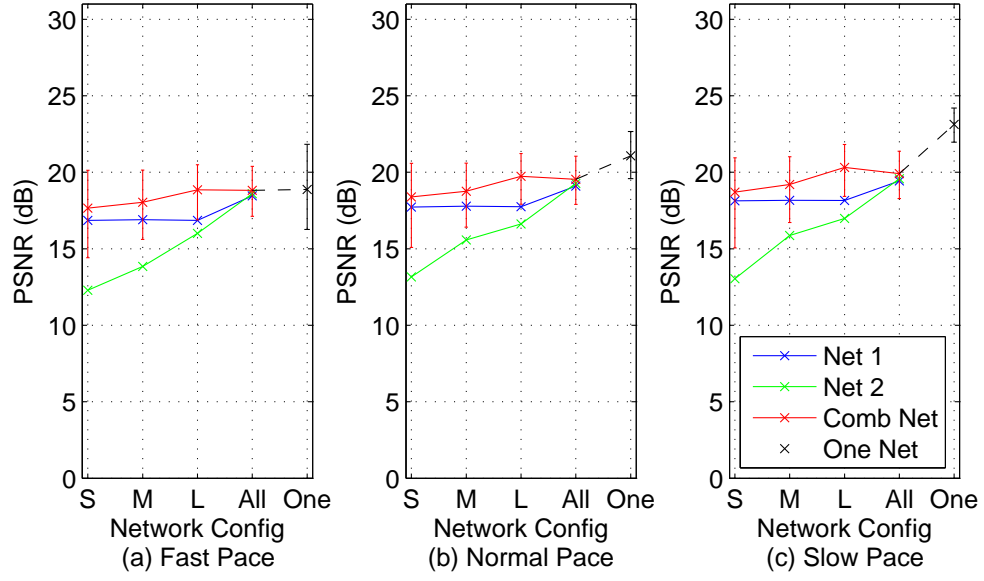
Figure 4.21: Median PSNR of simulated moving target by pace. $R_T = 1$ ft and $\sigma_n = 6$ dB.
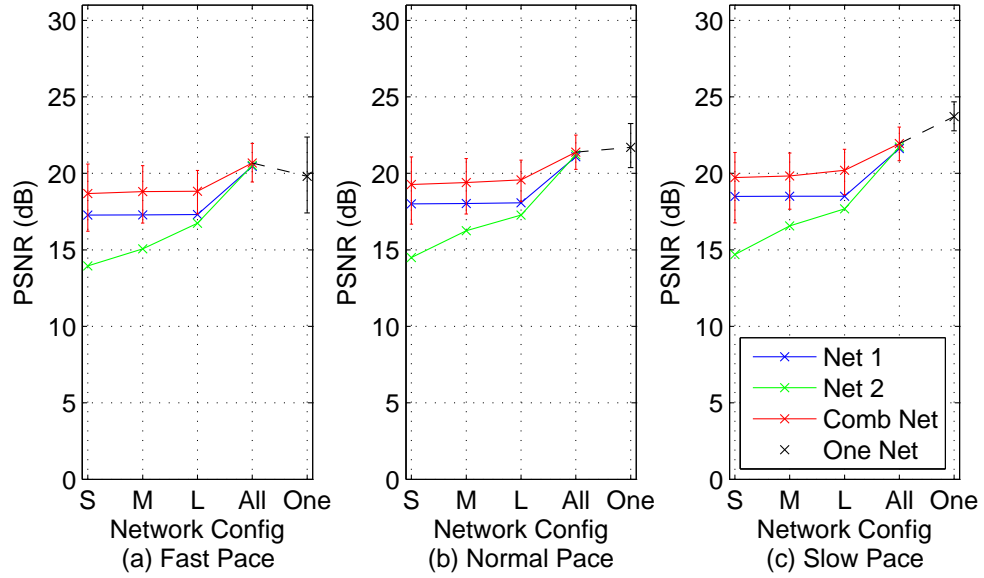
Figure 4.22: Median PSNR of simulated moving target by pace. $R_T = 1.3$ ft and $\sigma_n = 6$ dB.
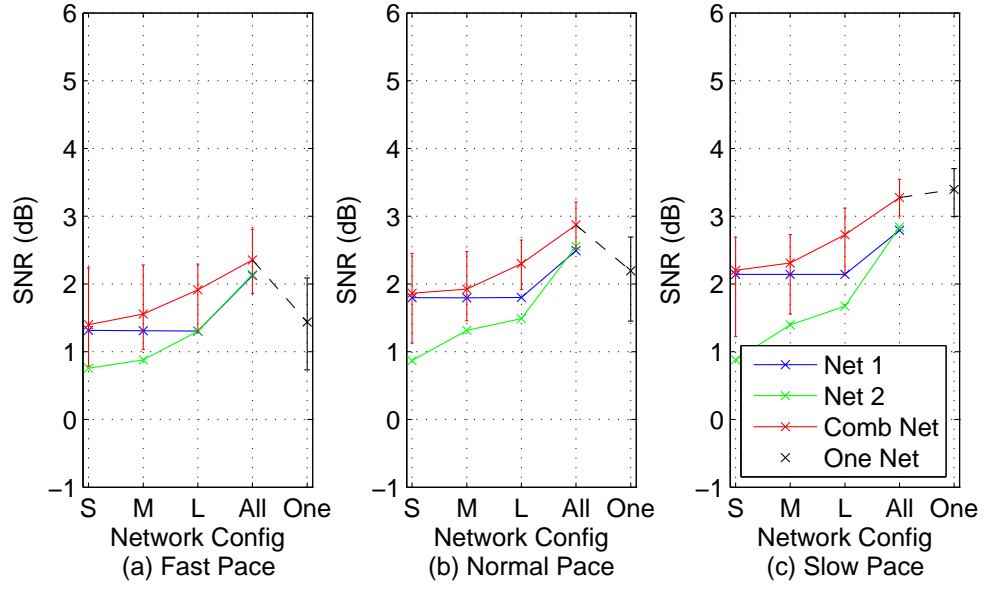
Figure 4.23: Median SNR of simulated moving target by pace. $R_T = 1$ ft and $\sigma_n = 2$ dB.
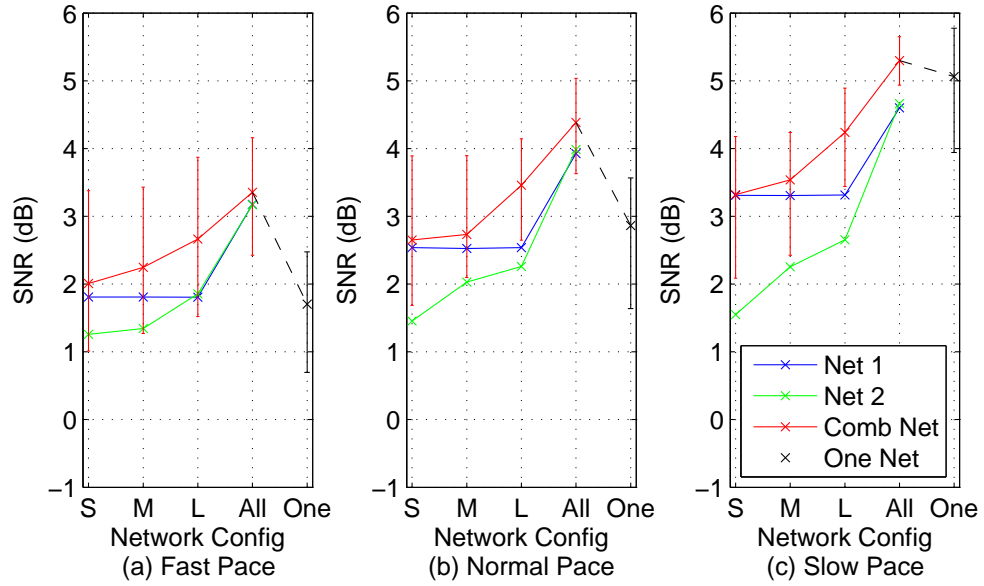
Figure 4.24: Median SNR of simulated moving target by pace. $R_T = 1.3$ ft and $\sigma_n = 2$ dB.
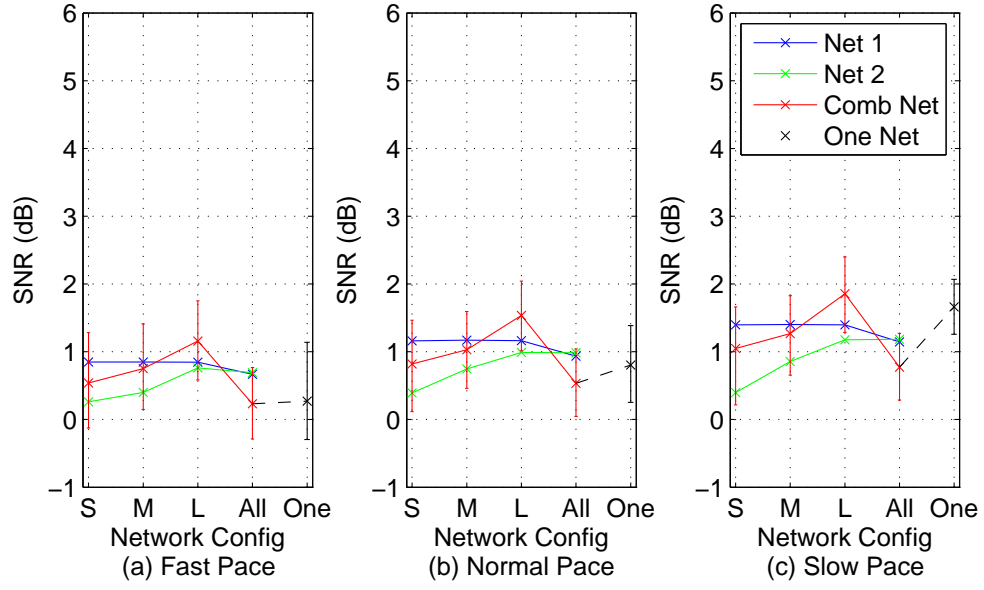
Figure 4.25: Median SNR of simulated moving target by pace. $R_T = 1$ ft and $\sigma_n = 6$ dB.
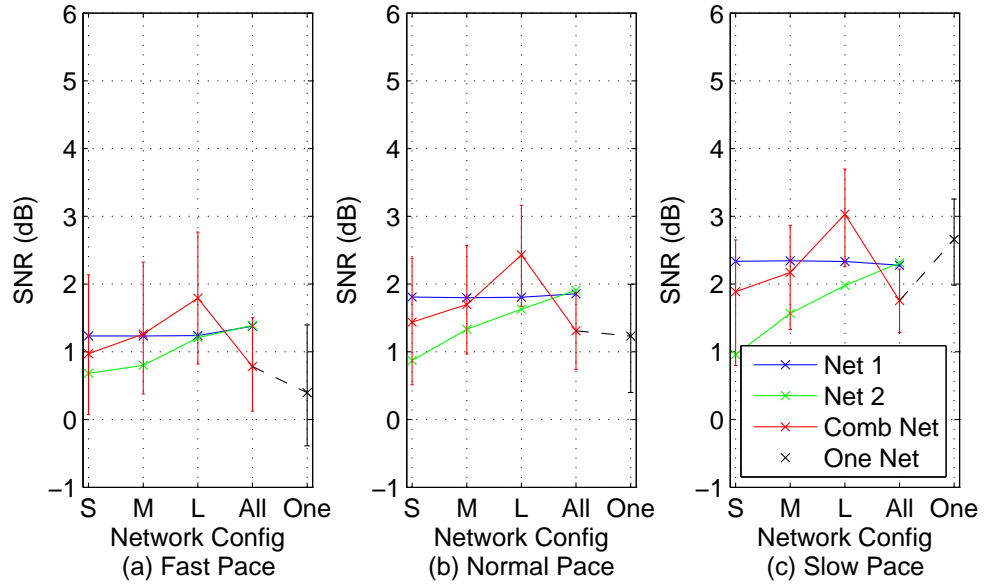
Figure 4.26: Median SNR of simulated moving target by pace. $R_T = 1.3$ ft and $\sigma_n = 6$ dB.
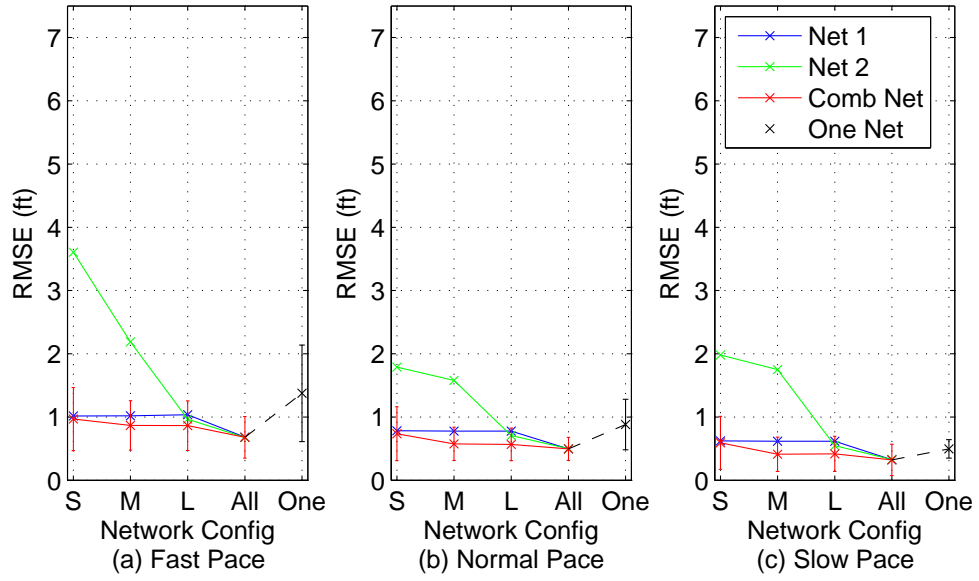
Figure 4.27: Average RMSE of simulated moving target for each pace using maximum intensity value estimation technique. $R_T = 1$ ft and $\sigma_n = 2$ dB.
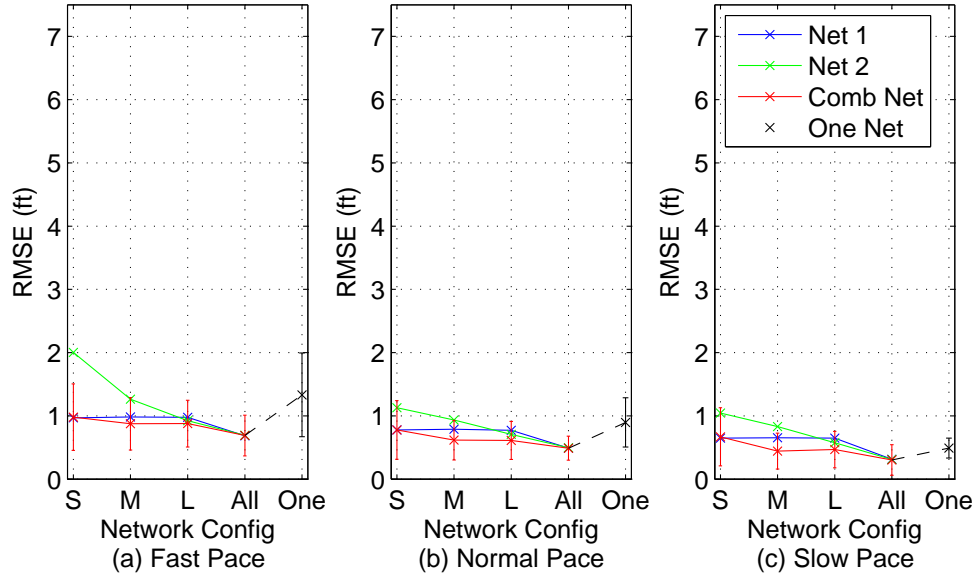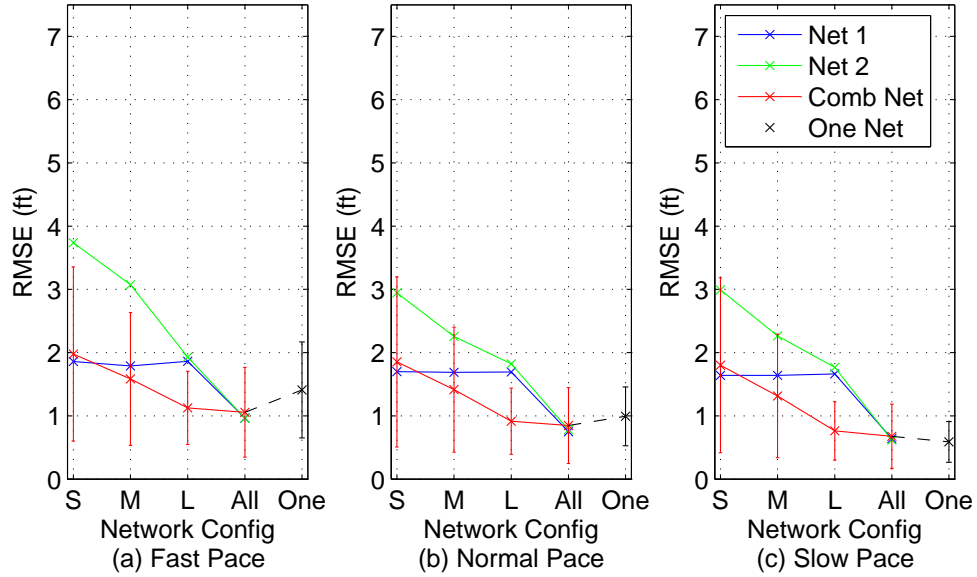

Figure 4.28: Average RMSE of simulated moving target for each pace using maximum intensity value estimation technique. $R_T = 1.3$ ft and $\sigma_n = 2$ dB.
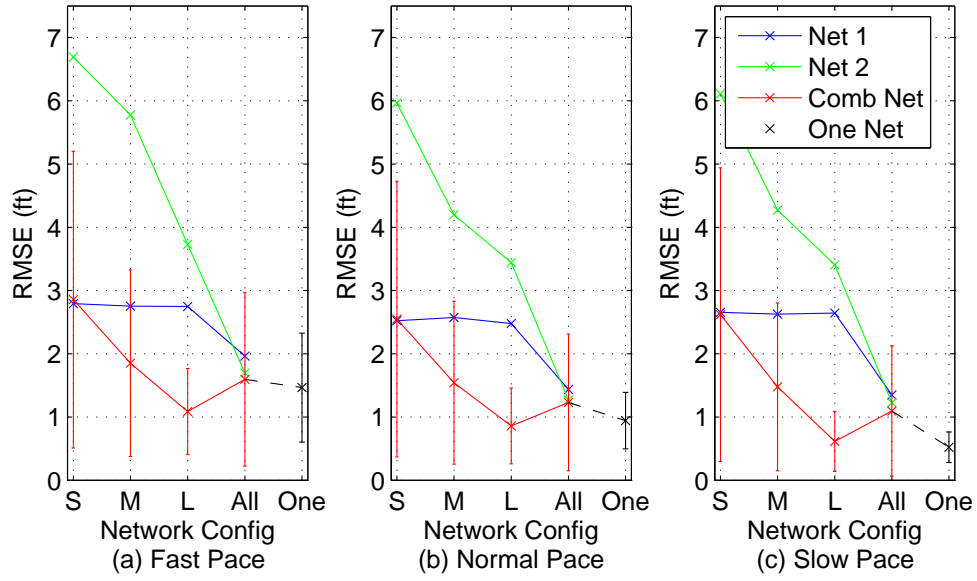
Figure 4.29: Average RMSE of simulated moving target for each pace using maximum intensity value estimation technique. $R_T = 1$ ft and $\sigma_n = 6$ dB.
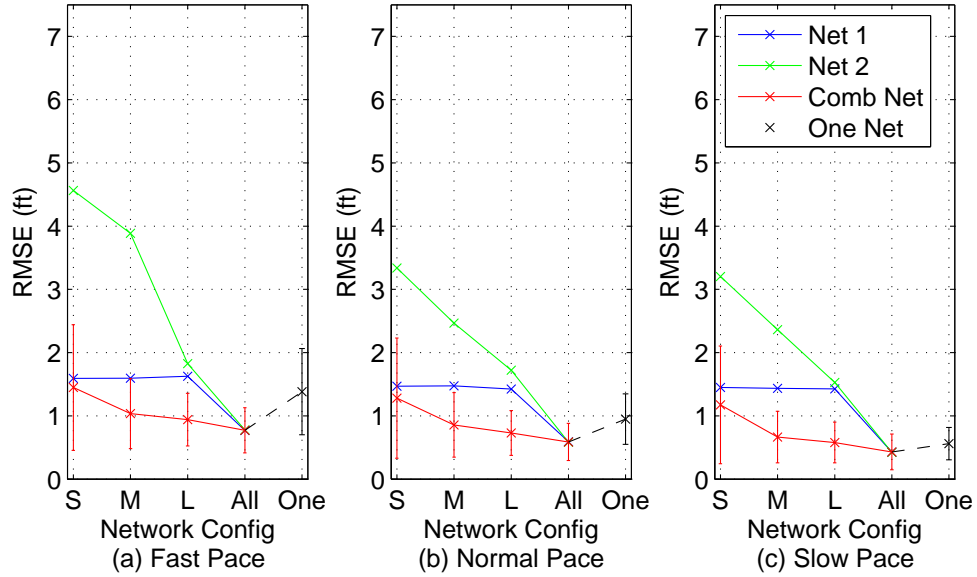
Figure 4.30: Average RMSE of simulated moving target for each pace using maximum intensity value estimation technique. $R_T = 1.3$ ft and $\sigma_n = 6$ dB.
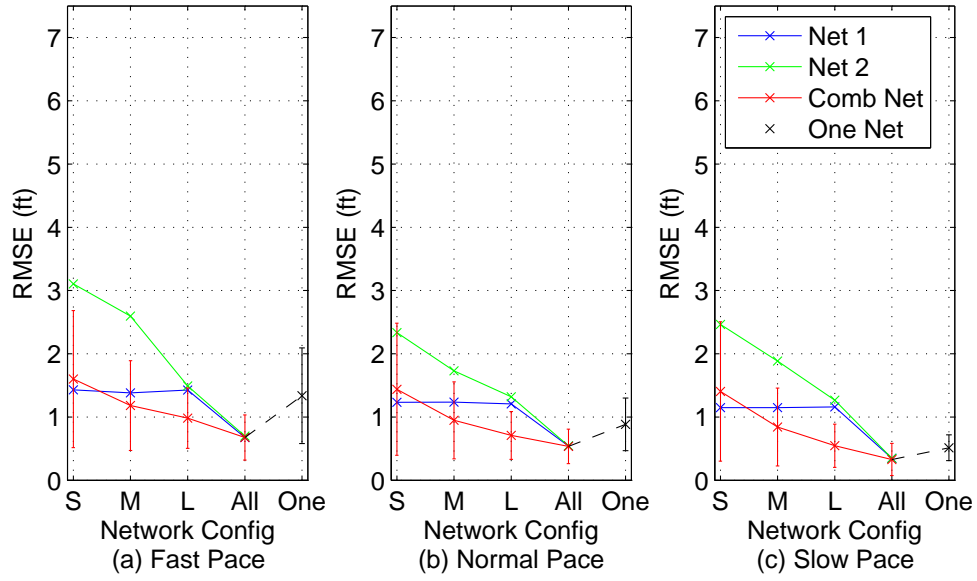
Figure 4.31: Average RMSE of simulated moving target for each pace using 1-D projection estimation technique. $R_T = 1$ ft and $\sigma_n = 2$ dB.
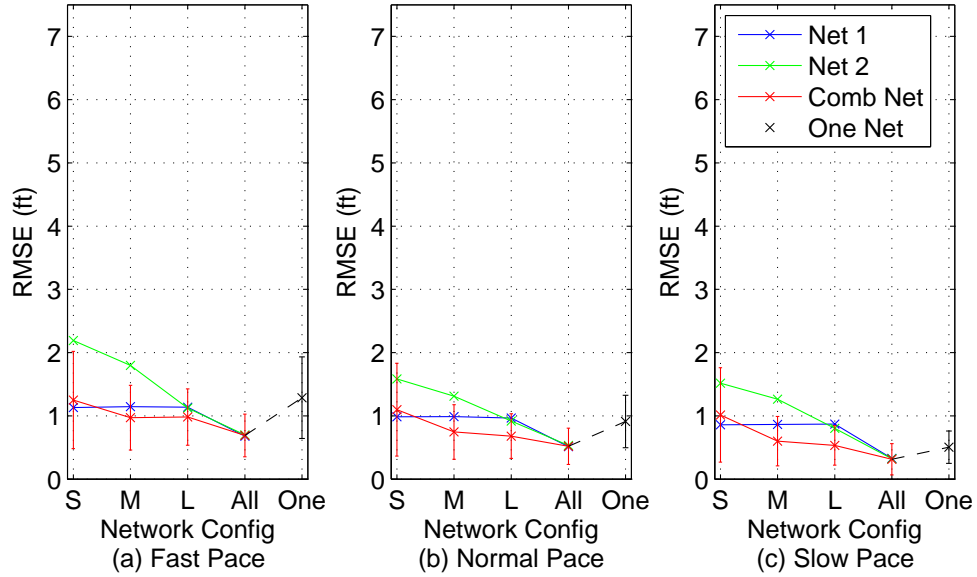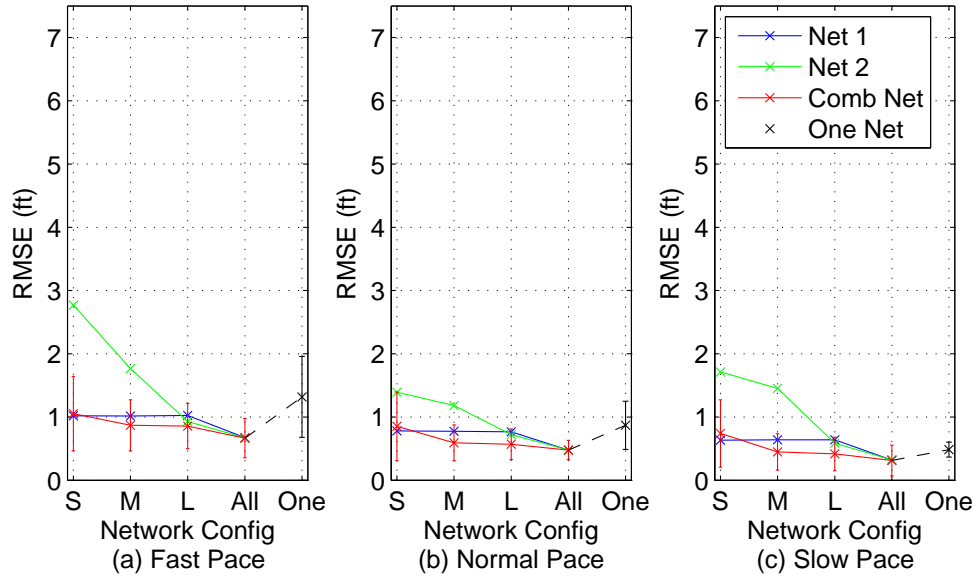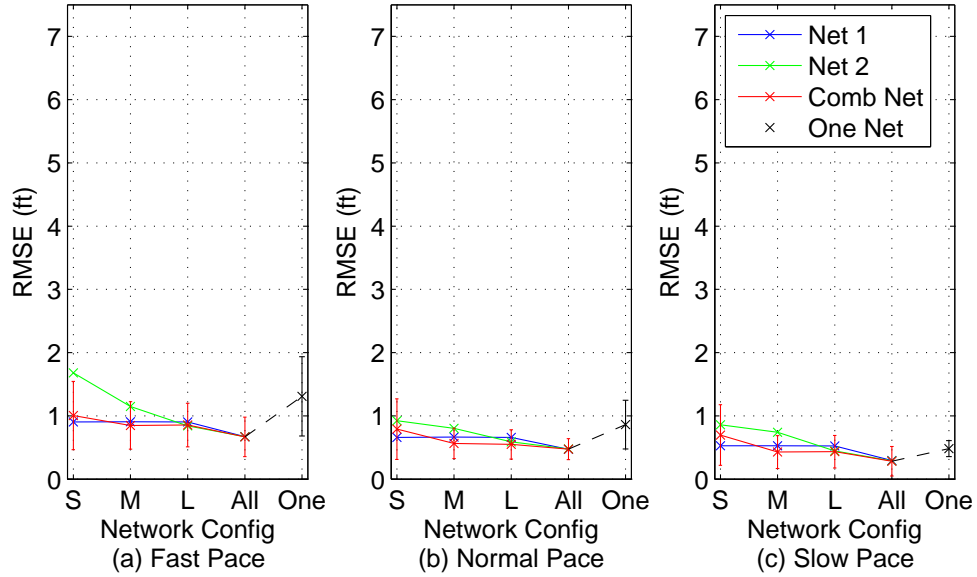

Figure 4.32: Average RMSE of simulated moving target for each pace using 1-D projection estimation technique. $R_T = 1.3$ ft and $\sigma_n = 2$ dB.
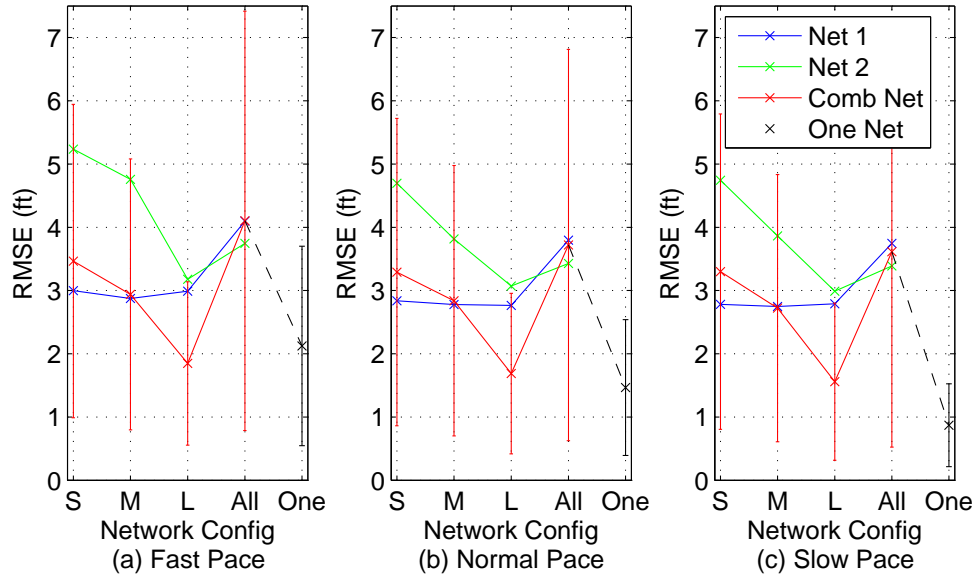
Figure 4.33: Average RMSE of simulated moving target for each pace using 1-D projection estimation technique. $R_T = 1$ ft and $\sigma_n = 6$ dB.

Figure 4.34: Average RMSE of simulated moving target for each pace using 1-D projection estimation technique. $R_T = 1.3$ ft and $\sigma_n = 6$ dB.
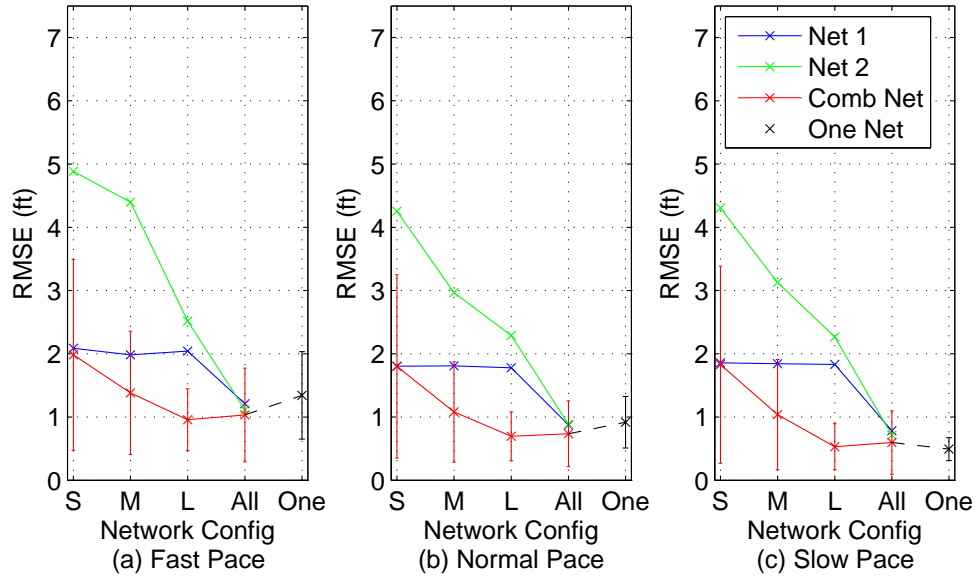
Figure 4.35: Average RMSE of simulated moving target for each pace using Gaussian kernel estimation technique. $R_T = 1$ ft and $\sigma_n = 2$ dB.
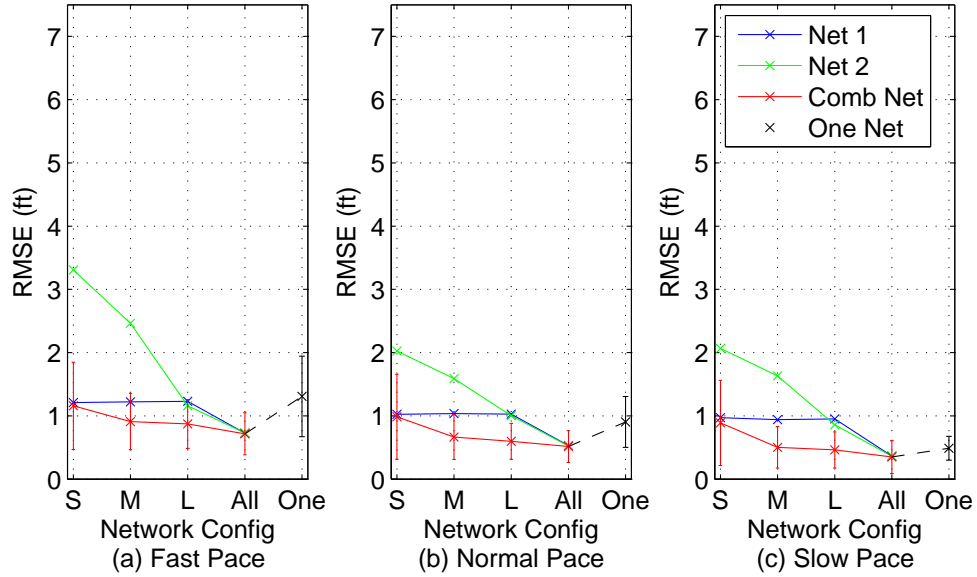

Figure 4.36: Average RMSE of simulated moving target for each pace using Gaussian kernel estimation technique. $R_T = 1.3$ ft and $\sigma_n = 2$ dB.

Figure 4.37: Average RMSE of simulated moving target for each pace using Gaussian kernel estimation technique. $R_T = 1$ ft and $\sigma_n = 6$ dB.

Figure 4.38: Average RMSE of simulated moving target for each pace using Gaussian kernel estimation technique. $R_T = 1.3$ ft and $\sigma_n = 6$ dB.

4.3.2.2 Experimental.

Fig. 4.39 shows the attenuation images of a moving target at a fast pace for each network configuration. The position of the target is at (2,8) ft for this data frame while the target is heading from (2,14) ft to (2,2) ft. Note that the dark oval-like shape in each attenuation image is slightly behind the true position of the target. Fig. 4.40 shows an example of the estimated $(\hat{x}, \hat{y})$ position for each pace using the Gaussian estimation technique. Note in Fig. 4.40 that as the pace of a target increases, the position estimate error also increases.

Fig. 4.41 shows the median PSNR of all experimental moving target data with respect to pace. Fig. 4.42 shows the median SNR of all experimental moving target data with respect to pace. Similar to simulated results, the median PSNR of the combined network image is always better than each individual network. The median PSNR is also higher as the pace of the target is slower. The *All* network configuration provides the best median PSNR values in comparison to the other network configurations. Looking at Fig. 4.42, the median SNR increases as the pace of the target decreases. However, the median SNR is fairly similar between each network configuration with a difference of less than 0.5 dB. The *One* network configuration has the lowest median SNR values, regardless of the pace.

Fig. 4.43 shows the average RMSE using the maximum intensity value estimation technique, Fig. 4.44 shows the average RMSE using the 1-D projection estimation technique, and Fig. 4.45 shows the average RMSE using the Gaussian kernel estimation technique for experimental moving target data with respect to pace. For Figs. 4.43–4.45, (a) is the average RMSE of all the experimental moving data for a fast pace, (b) is the average RMSE of all the experimental moving data for a normal pace, and (c) is the average RMSE of all the experimental moving data for a slow pace. For the *Medium*, *Large*, and *All* network configurations, the average RMSE for the combined network is always lower than each individual network. Position estimation accuracy increases as the pace of the

90

target is slower. With the maximum intensity value and Gaussian estimation techniques, the *All* network configuration has the lowest average RMSE, followed by the *Large* network configuration. In the 1-D projection estimation technique, the *Large*, *All*, and *One* network configurations yield similar results. The 1-D projection estimation technique provides the highest average RMSE between the three estimation techniques. The Gaussian estimation technique provides similar average RMSE as the maximum intensity value technique.
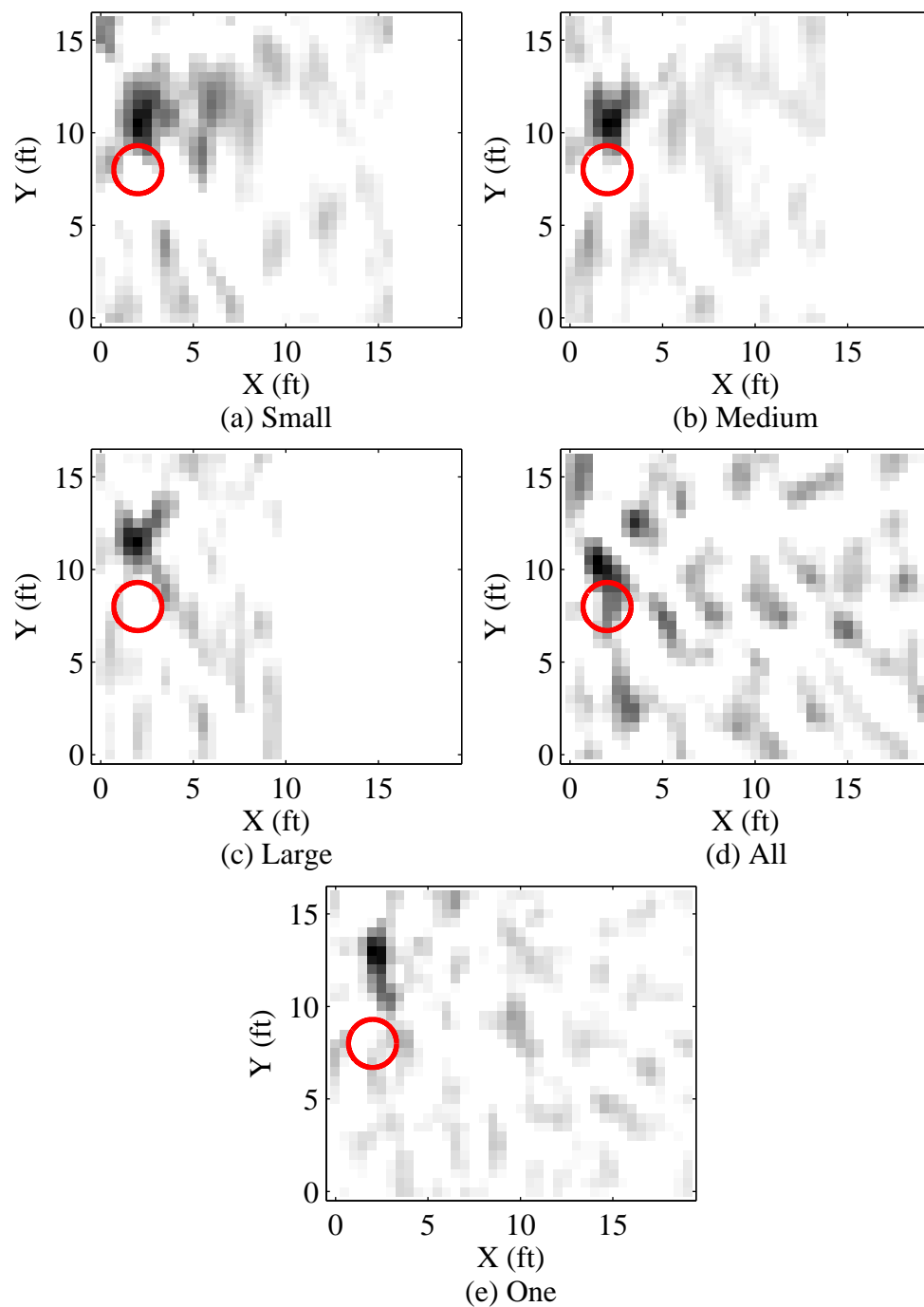
Figure 4.39: Attenuation images of an experimental moving target at a fast pace. Current position for target is (2,8) ft for this frame of data. The circle marks the true position of the target.
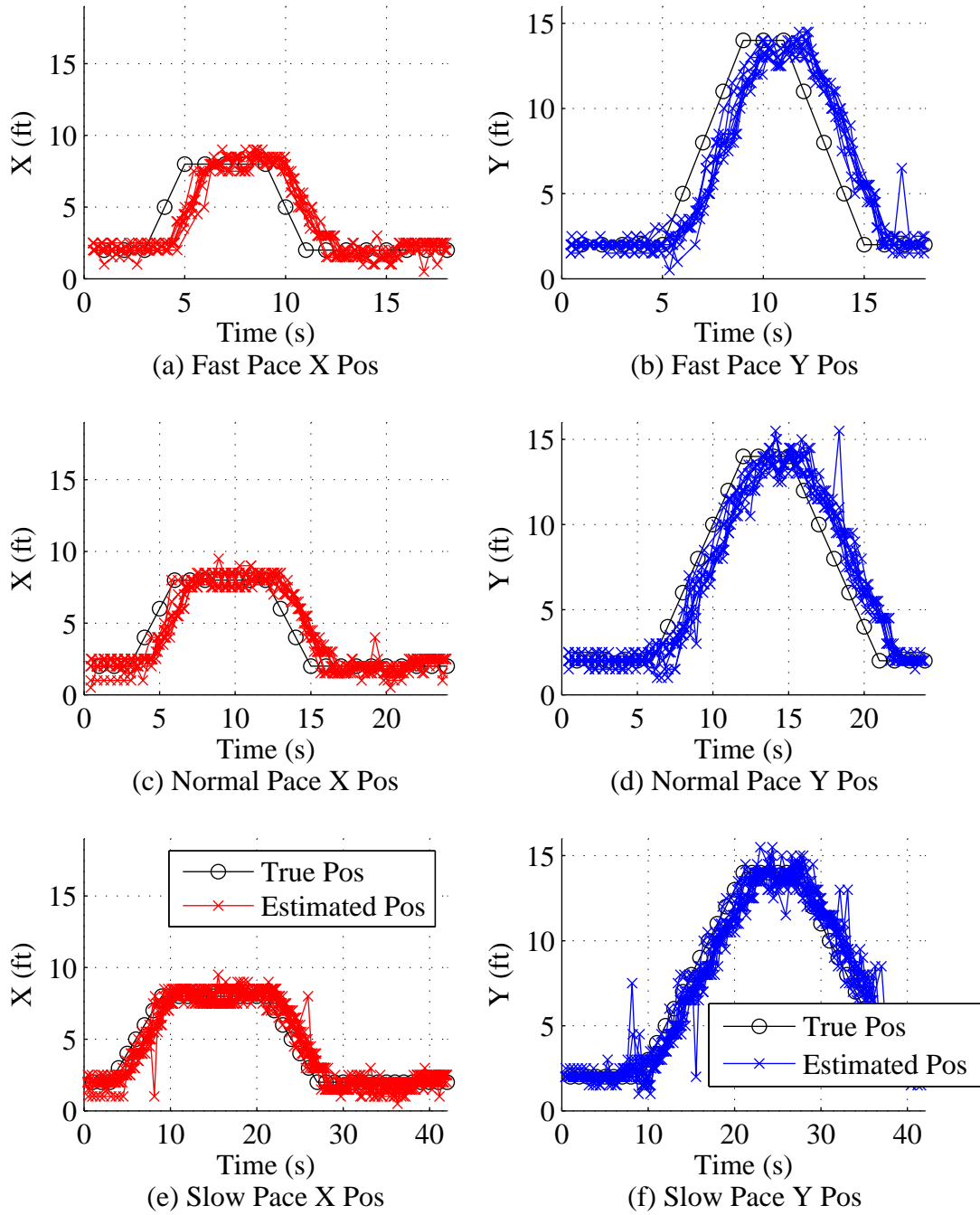
Figure 4.40: Example of a comparison between the true position of the target and experimental estimated position of the target in the *Large* network configuration.
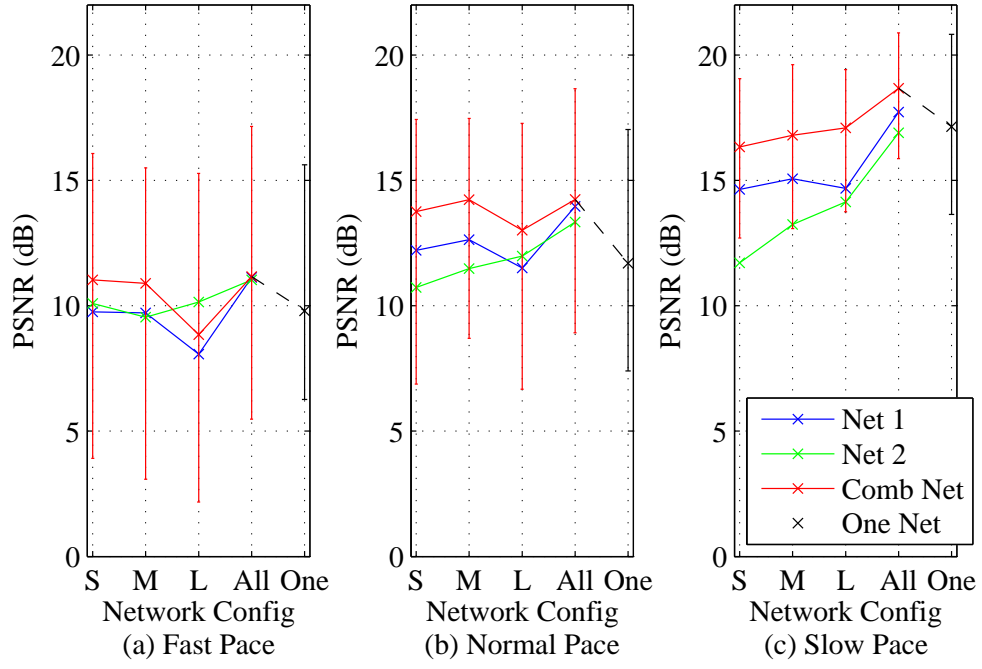
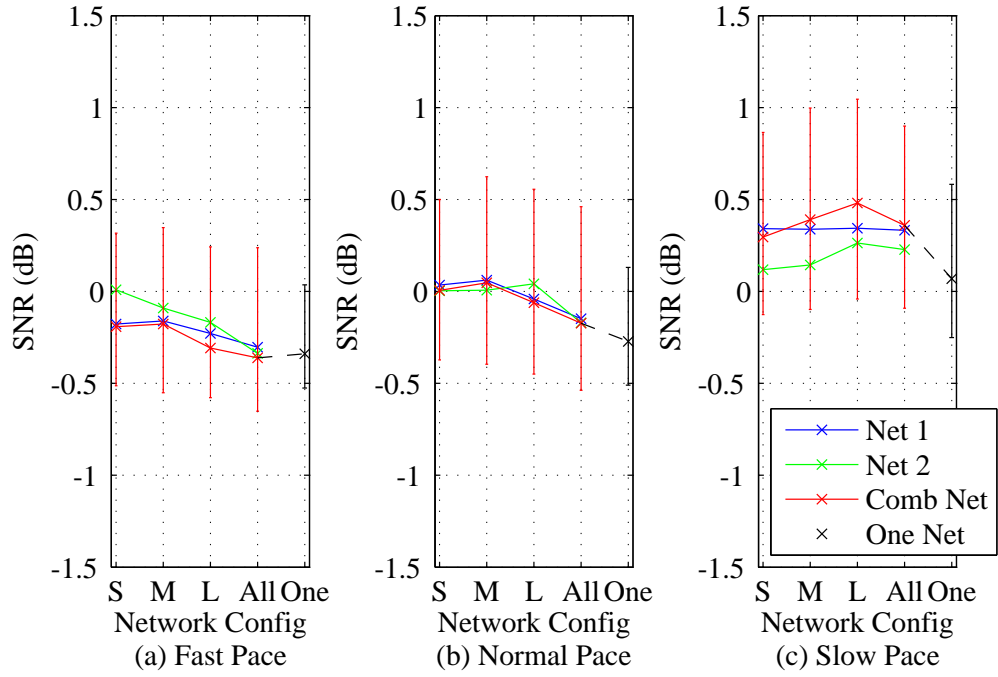Figure 4.41: Median PSNR of experimental moving target for each network configuration.

Figure 4.42: Median SNR of experimental moving target for each network configuration.
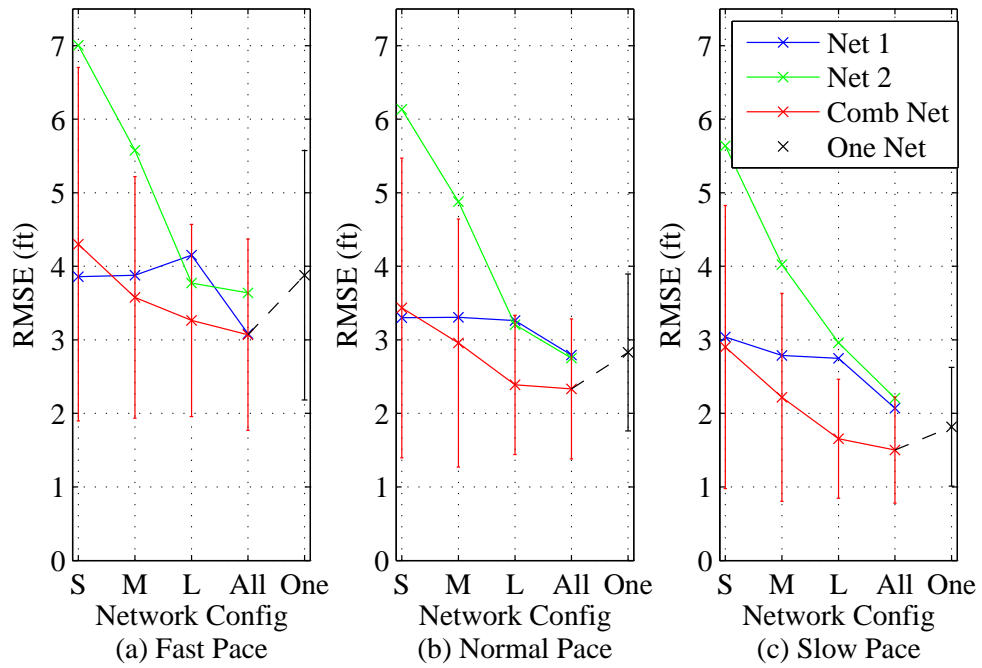
Figure 4.43: Average RMSE of experimental moving target for each network configuration using maximum intensity value estimation technique.
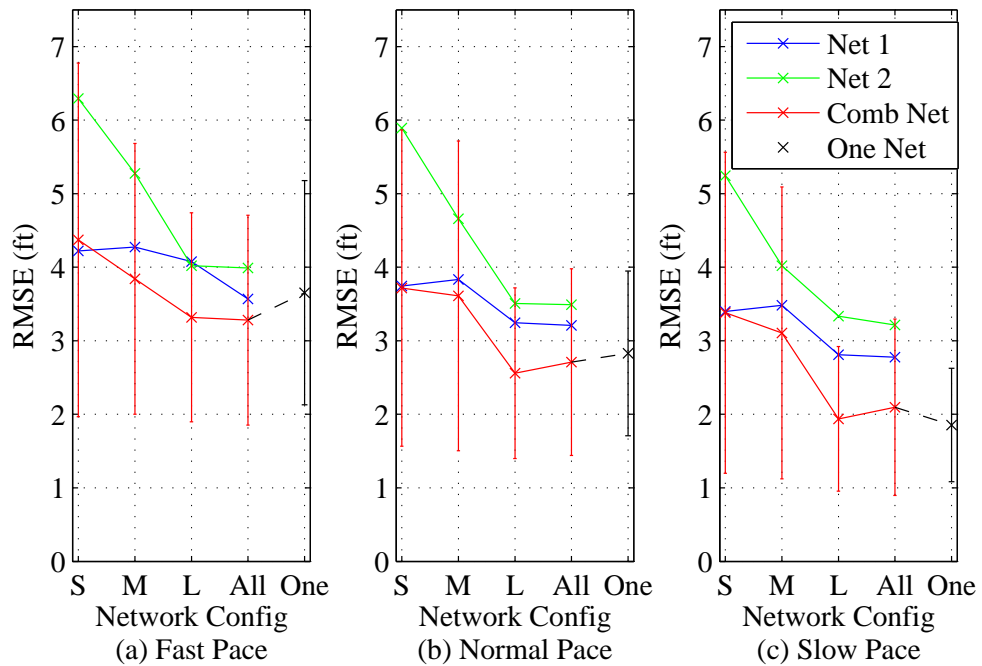

Figure 4.44: Average RMSE of experimental moving target for each network configuration using 1-D projection estimation technique.
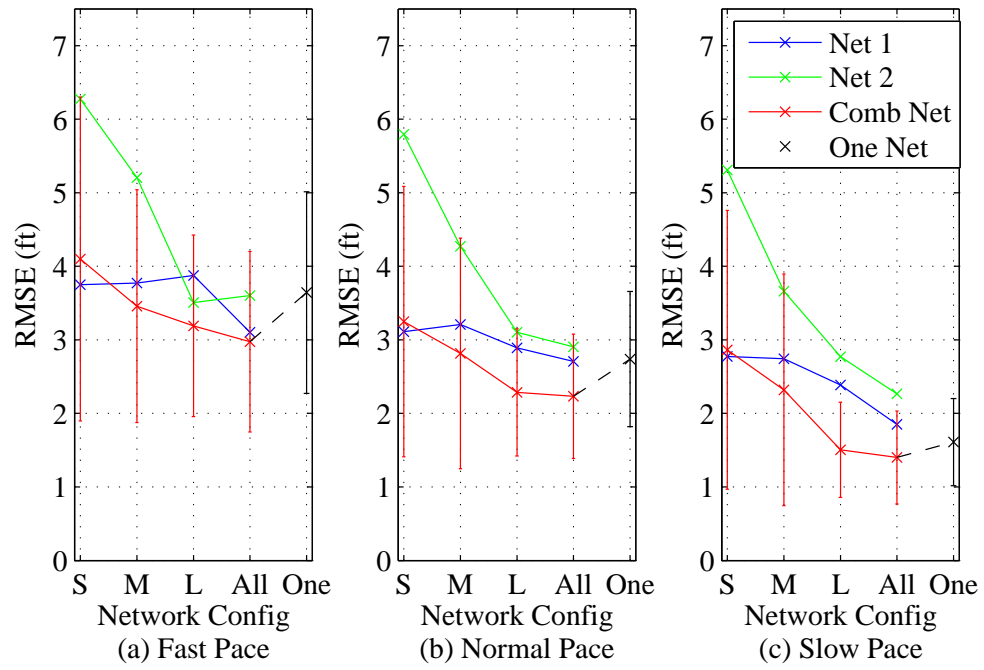
Figure 4.45: Average RMSE of experimental moving target for each network configuration using Gaussian kernel estimation technique.

4.3.3 Moving by Pattern.

This section presents the results of moving target data for each of the three different patterns mentioned in Section 3.6.2.2.

4.3.3.1 Simulations.

Figs. 4.46–4.49 show the median PSNR of a simulated moving target for all 900 realizations with respect to pattern. Similar to stationary results, the median PSNR of the combined network image is always higher than or the same as each individual network. The median PSNR decreases as σ_n increases. However, no one pattern consistently shows a significantly better median PSNR than the other patterns for each R_T and σ_n.

Figs. 4.50–4.53 show the median SNR of a simulated moving target for all 900 realizations with respect to pattern. The median SNR is also always better in a combined network than each individual network. When $\sigma_n = 2$ dB, median SNR increases as there is more overlap between two WSNs. Also, the *All* network configuration has the highest median SNR when $\sigma_n = 2$ dB. When $\sigma_n = 6$ dB, the *Large* network configuration has the highest median SNR and the *All* network configuration has one of the lowest median SNR. However, similar to Figs. 4.46–4.49, there is no one pattern that consistently shows a significantly better median SNR than the other patterns for each R_T and σ_n.

Figs. 4.54–4.57 show the average RMSE of a simulated moving target for all 900 realizations with respect to pattern using the maximum intensity value estimation technique. Figs. 4.58–4.61 show the average RMSE of a simulated moving target for all 900 realizations with respect to pattern using the 1-D projection estimation technique. Figs. 4.62–4.65 show the average RMSE of a simulated moving target for all 900 realizations with respect to pattern using the Gaussian kernel to smooth the attenuation image prior to finding the maximum intensity value. For the *Medium*, *Large*, and *All* network configurations, the average RMSE for the combined network is always lower than each individual network. The 1-D projection estimation technique provides the highest

average RMSE in comparison to the other estimation techniques. The Gaussian estimation technique provides similar or slightly lower average RMSE as the maximum intensity value estimation technique. When σ_n = 2 dB, the *All* network configuration provides the best position estimates with the lowest average RMSE. The *Large* and *Medium* network configurations provide the next best position estimations, followed by the *One* network configuration. When σ_n = 6 dB and R_T = 1 ft, the *Large* or *One* network configuration provides the lowest average RMSE. When σ_n = 6 dB and R_T = 1.3 ft, the *All* network configuration generally provides the lowest average RMSE, followed by a mix between the *One* and *Large* network configurations. Pattern 3 generally has a consistent average RMSE for each network configuration, but the average RMSE for the other two patterns is not significantly different.
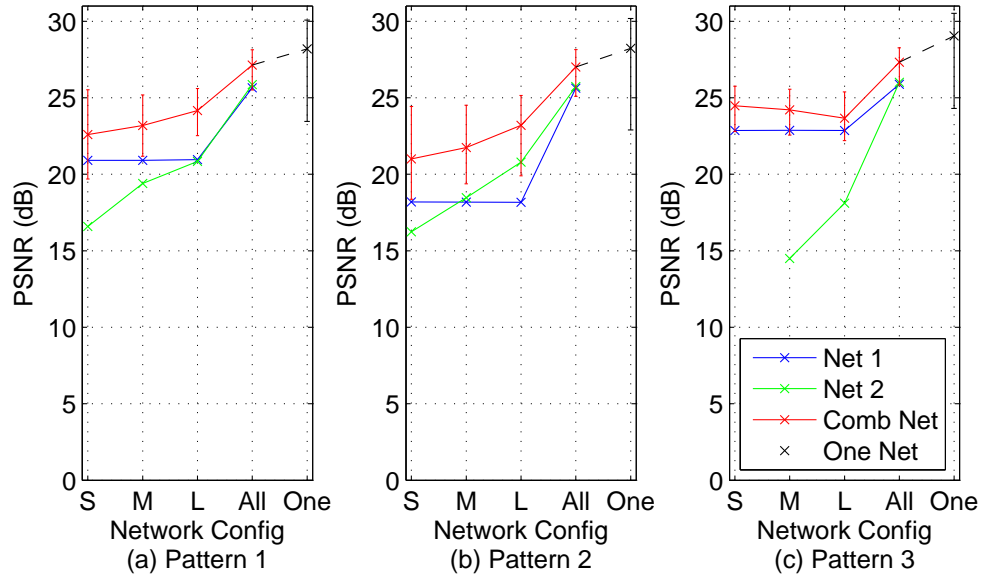
Figure 4.46: Median PSNR of simulated moving target by pattern. $R_T = 1$ ft and $\sigma_n = 2$ dB.
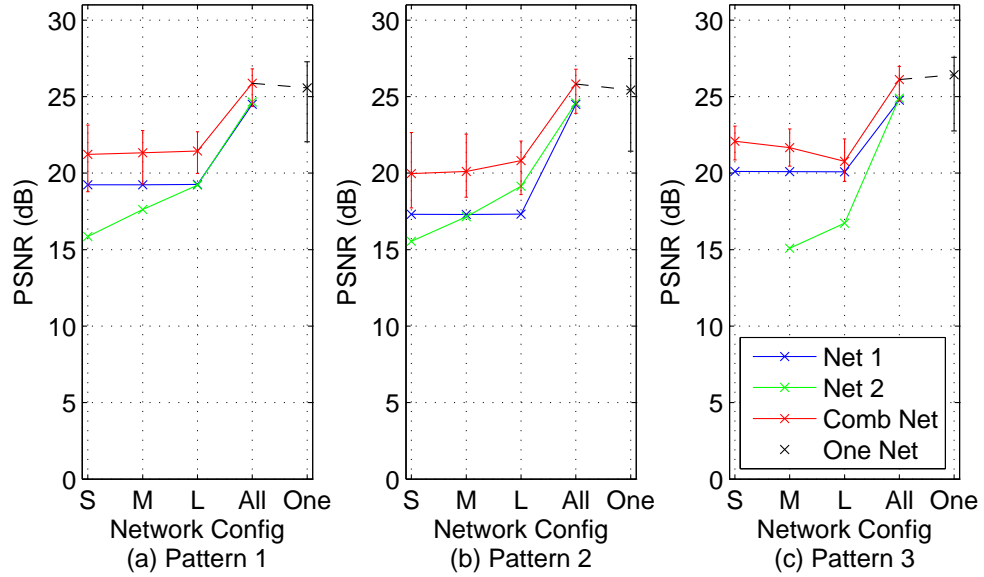

Figure 4.47: Median PSNR of simulated moving target by pattern. $R_T = 1.3$ ft and $\sigma_n = 2$ dB.
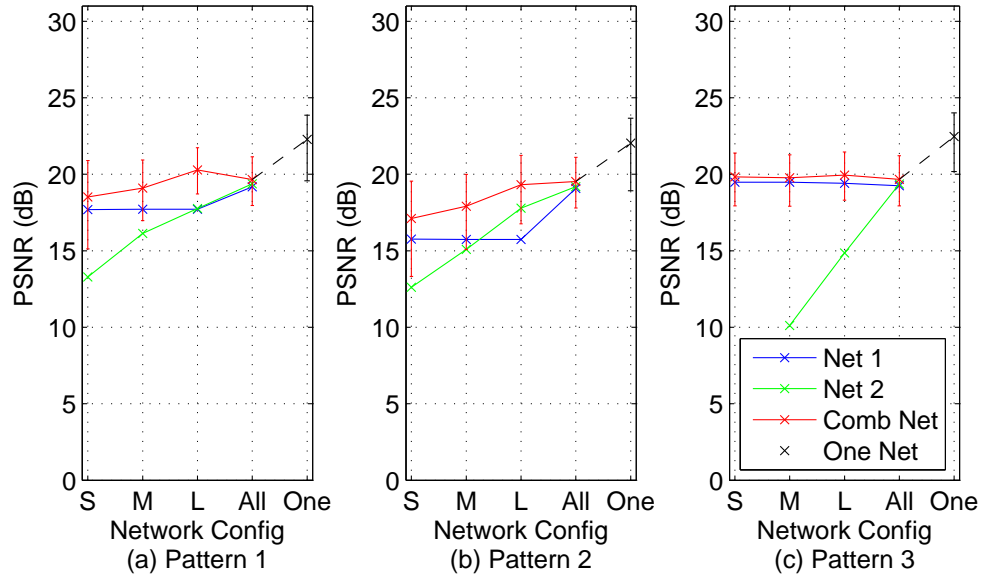
Figure 4.48: Median PSNR of simulated moving target by pattern. $R_T = 1$ ft and $\sigma_n = 6$ dB.
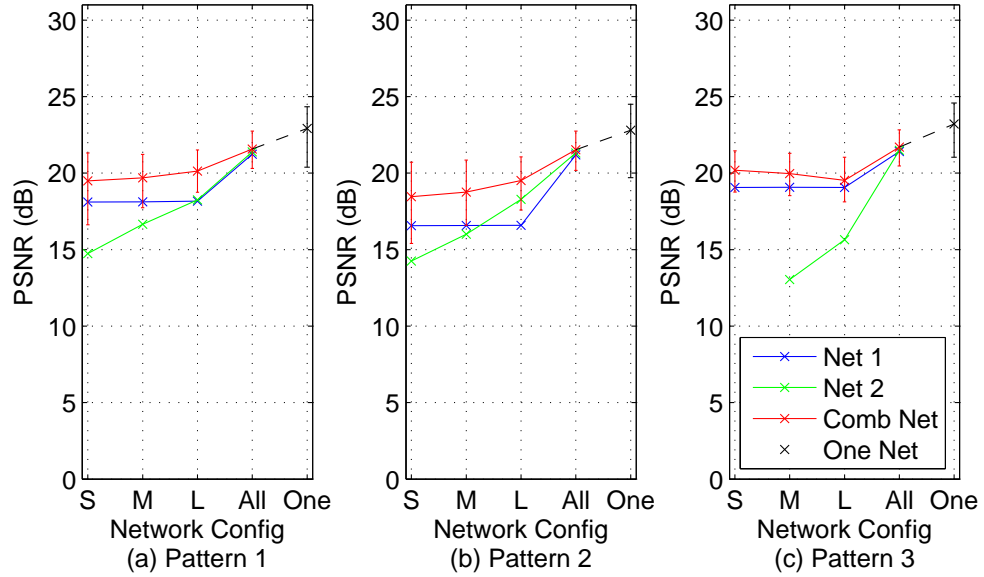

Figure 4.49: Median PSNR of simulated moving target by pattern. $R_T = 1.3$ ft and $\sigma_n = 6$ dB.
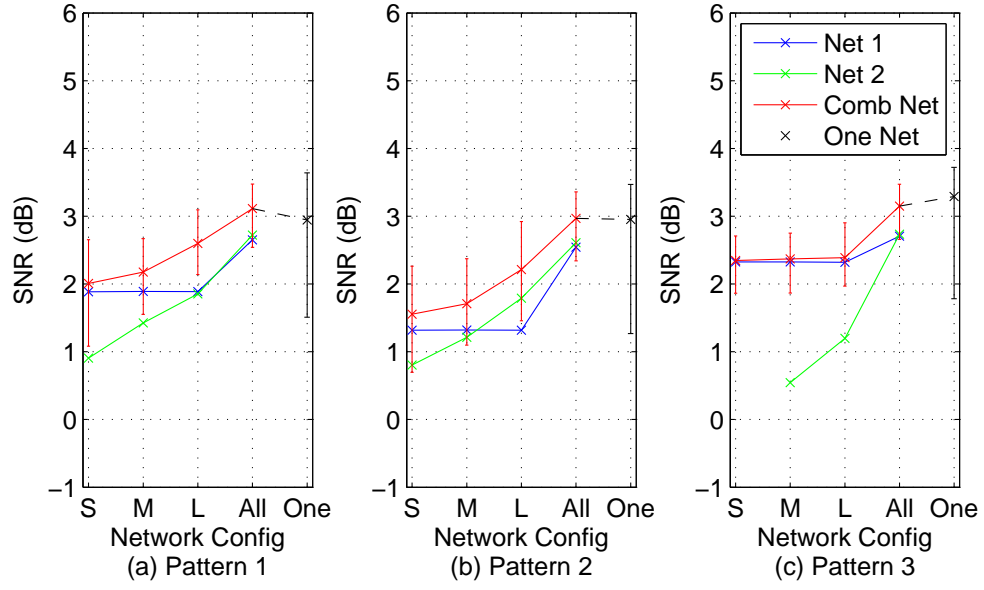
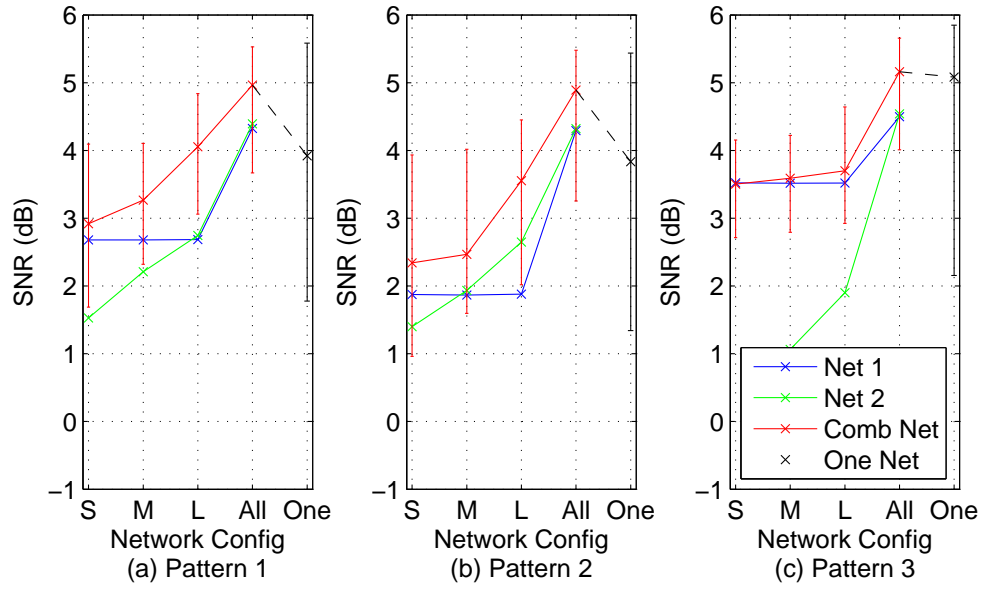Figure 4.50: Median SNR of simulated moving target by pattern. $R_T = 1$ ft and $\sigma_n = 2$ dB.

Figure 4.51: Median SNR of simulated moving target by pattern. $R_T = 1.3$ ft and $\sigma_n = 2$ dB.
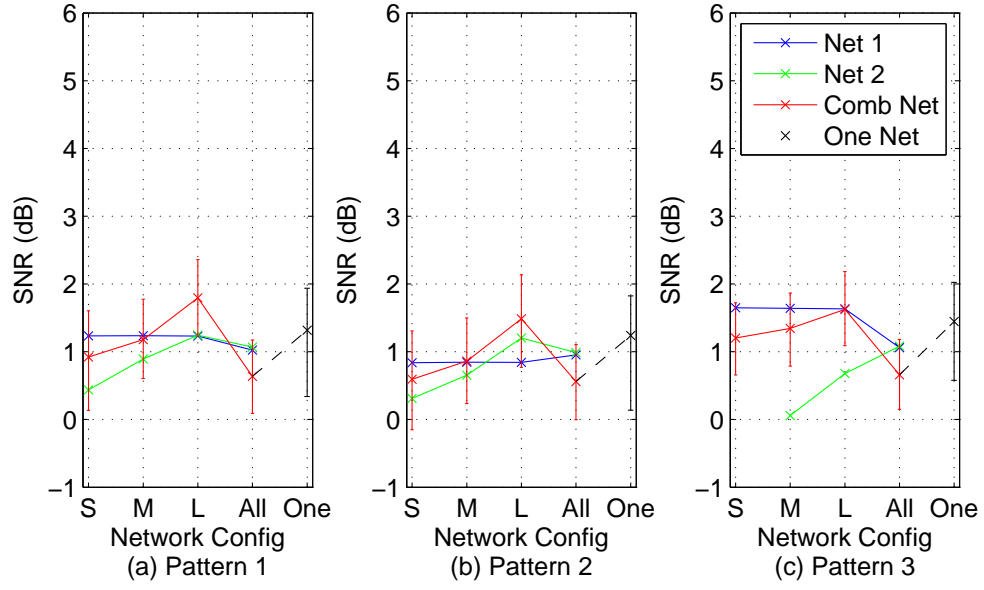
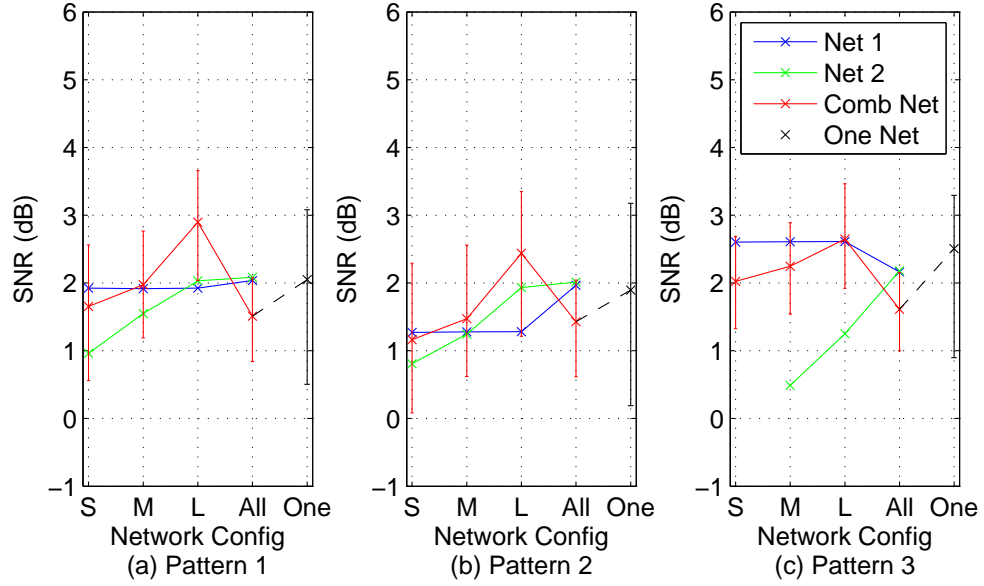Figure 4.52: Median SNR of simulated moving target by pattern. $R_T = 1$ ft and $\sigma_n = 6$ dB.

Figure 4.53: Median SNR of simulated moving target by pattern. $R_T = 1.3$ ft and $\sigma_n = 6$ dB.

Figure 4.54: Average RMSE of simulated moving target for each pattern using maximum intensity value estimation technique. $R_T = 1$ ft and $\sigma_n = 2$ dB.

Figure 4.55: Average RMSE of simulated moving target for each pattern using maximum intensity value estimation technique. $R_T = 1.3$ ft and $\sigma_n = 2$ dB.
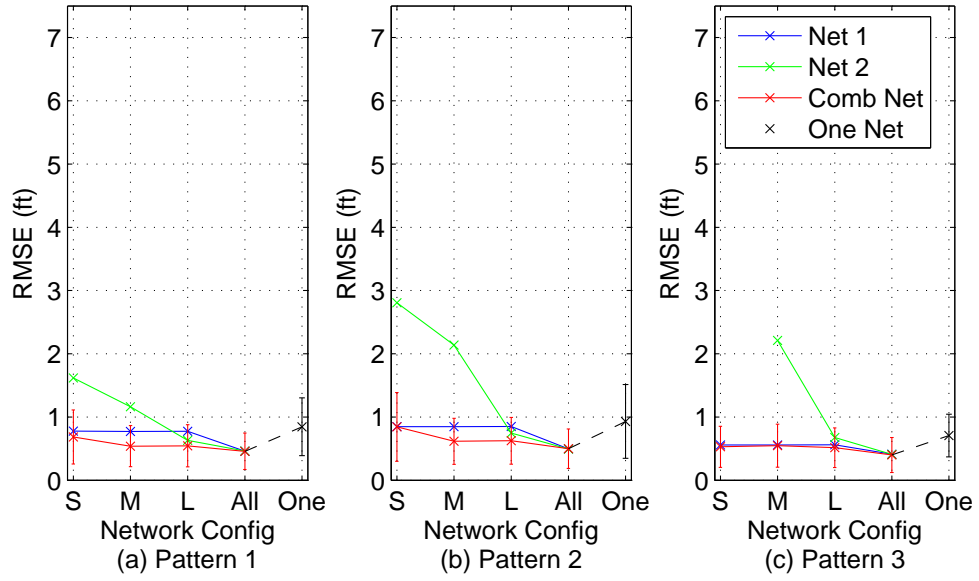
Figure 4.56: Average RMSE of simulated moving target for each pattern using maximum intensity value estimation technique. $R_T = 1$ ft and $\sigma_n = 6$ dB.
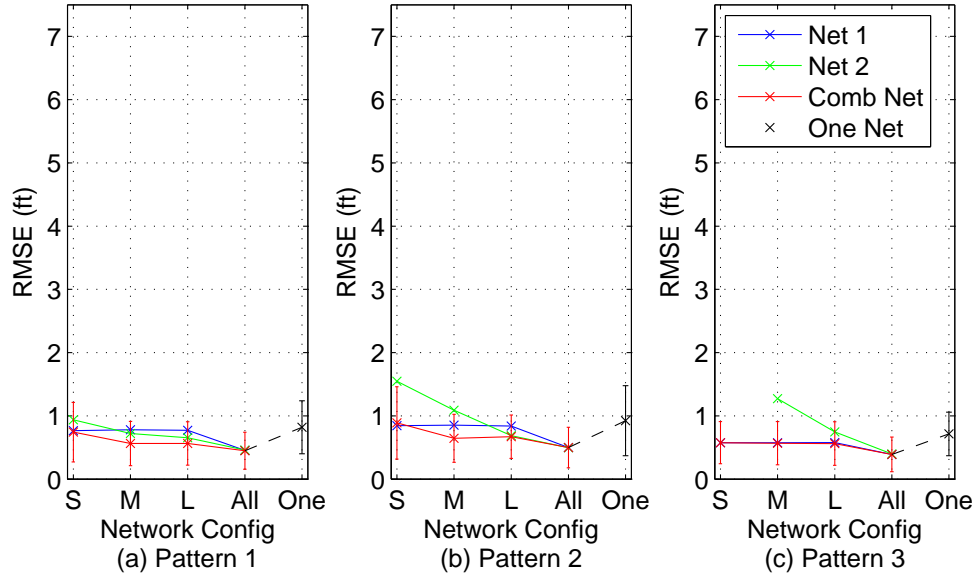

Figure 4.57: Average RMSE of simulated moving target for each pattern using maximum intensity value estimation technique. $R_T = 1.3$ ft and $\sigma_n = 6$ dB.
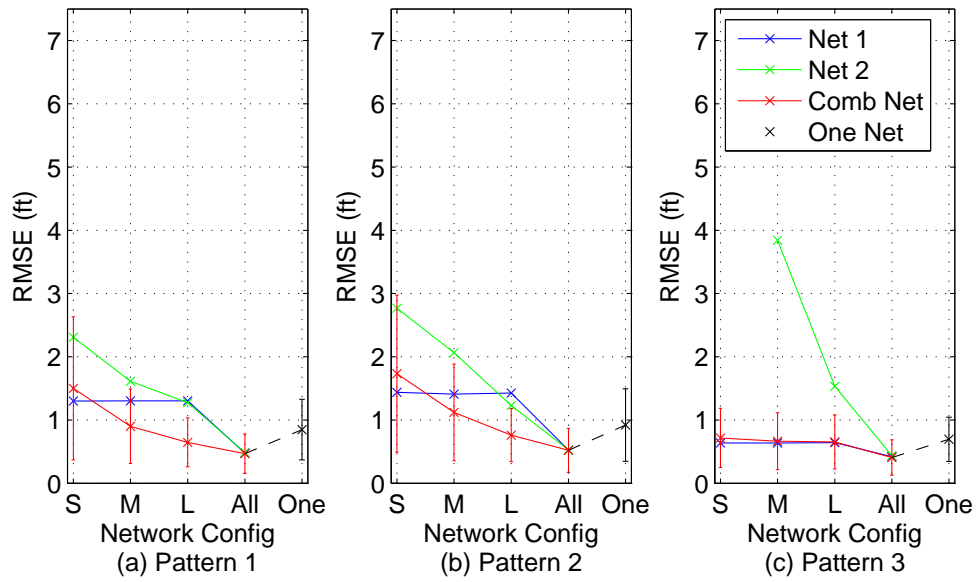
Figure 4.58: Average RMSE of simulated moving target for each pattern using 1-D projection estimation technique. $R_T = 1$ ft and $\sigma_n = 2$ dB.
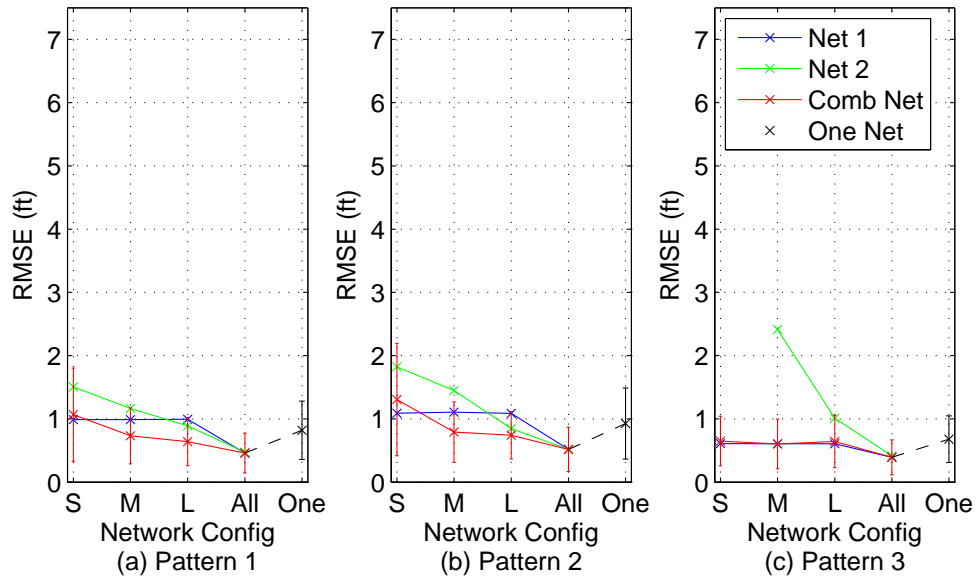
Figure 4.59: Average RMSE of simulated moving target for each pattern using 1-D projection estimation technique. $R_T = 1.3$ ft and $\sigma_n = 2$ dB.
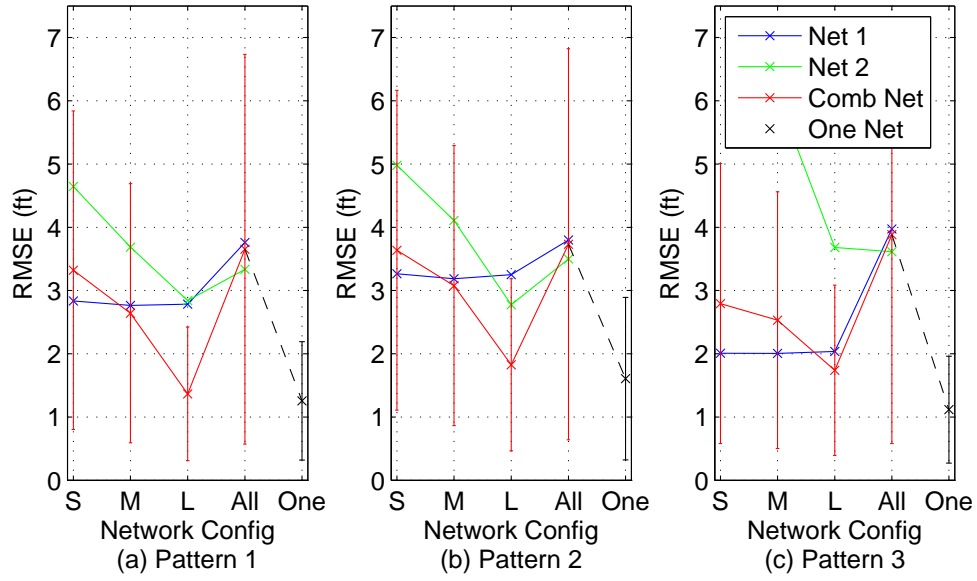
Figure 4.60: Average RMSE of simulated moving target for each pattern using 1-D projection estimation technique. $R_T = 1$ ft and $\sigma_n = 6$ dB.
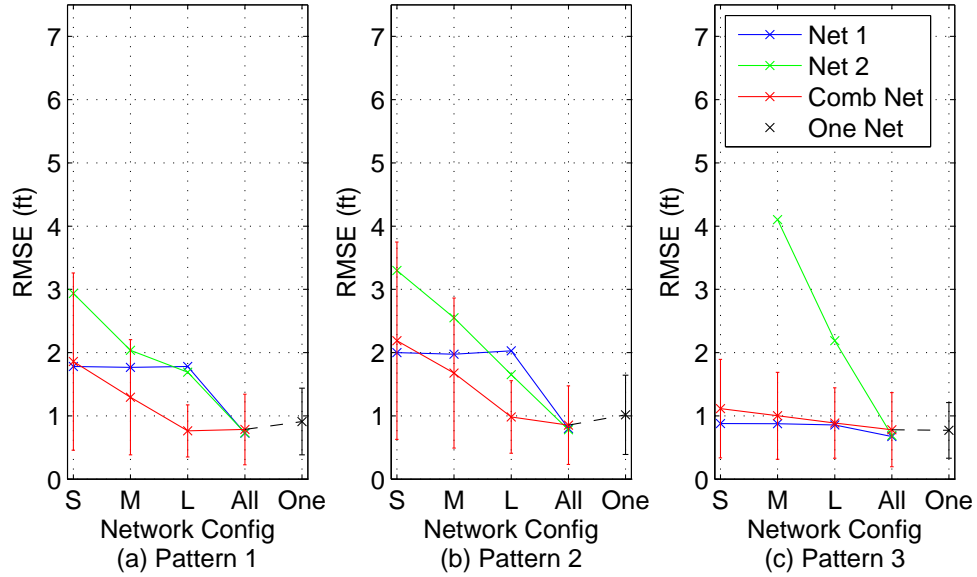
Figure 4.61: Average RMSE of simulated moving target for each pattern using 1-D projection estimation technique. $R_T = 1.3$ ft and $\sigma_n = 6$ dB.
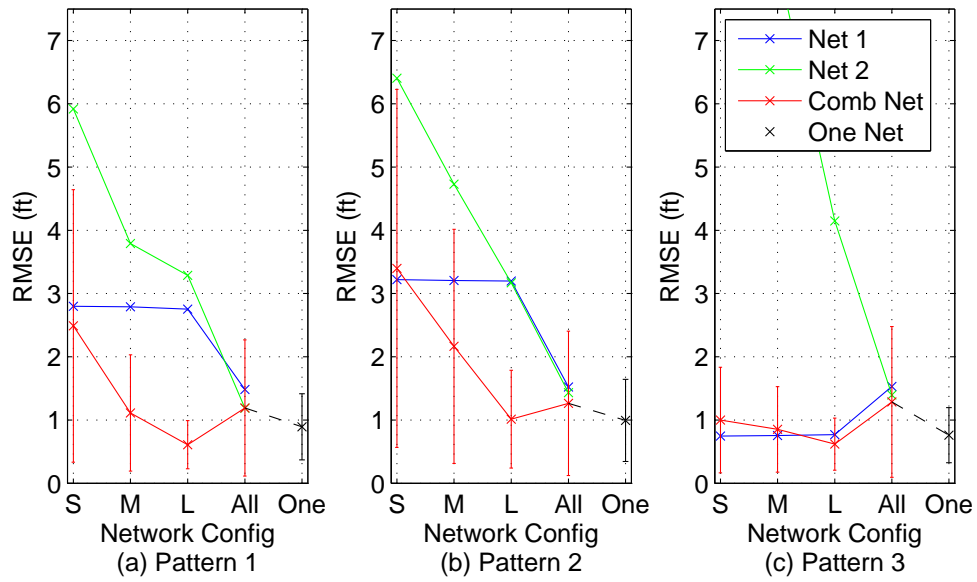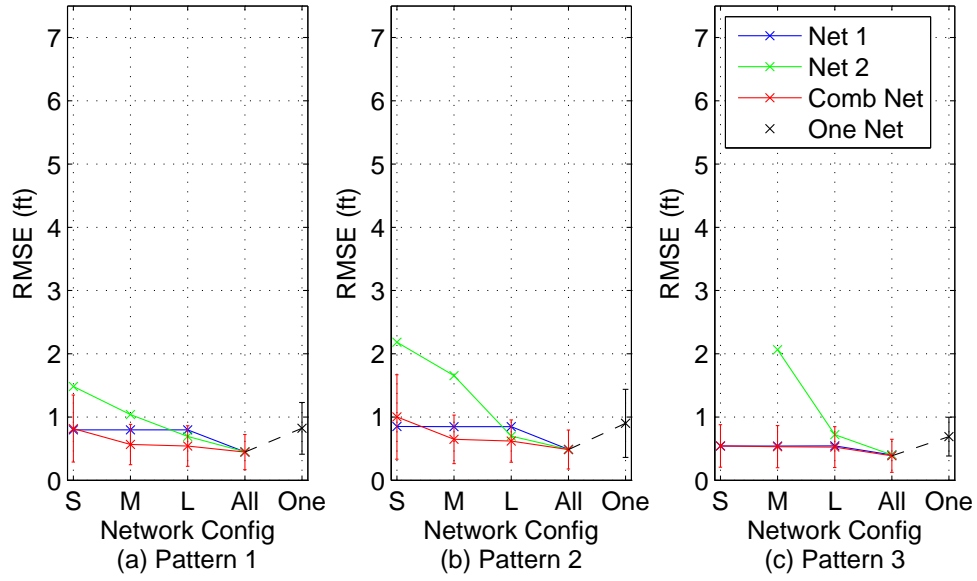
Figure 4.62: Average RMSE of simulated moving target for each pattern using Gaussian kernel estimation technique. $R_T = 1$ ft and $\sigma_n = 2$ dB.
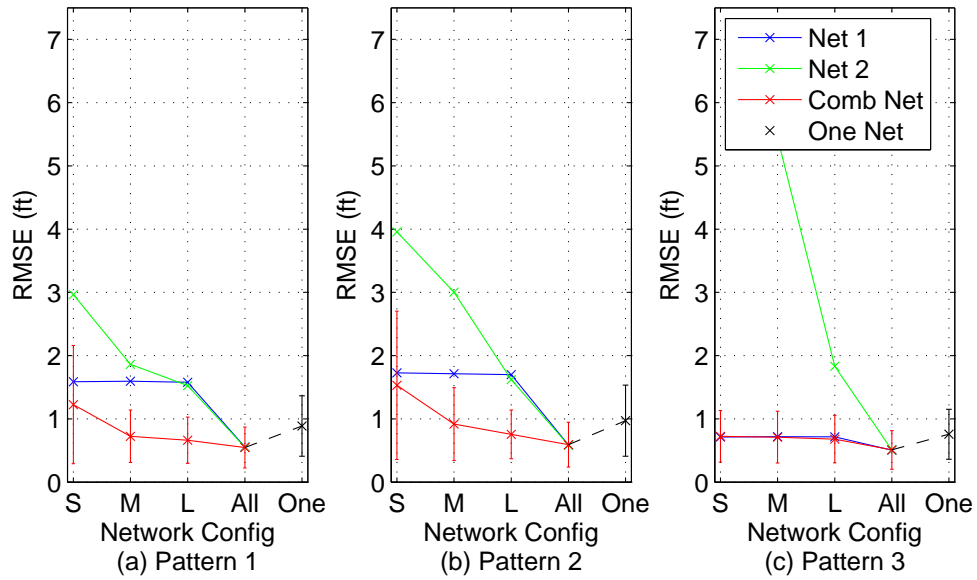

Figure 4.63: Average RMSE of simulated moving target for each pattern using Gaussian kernel estimation technique. $R_T = 1.3$ ft and $\sigma_n = 2$ dB.

Figure 4.64: Average RMSE of simulated moving target for each pattern using Gaussian kernel estimation technique. $R_T = 1$ ft and $\sigma_n = 6$ dB.
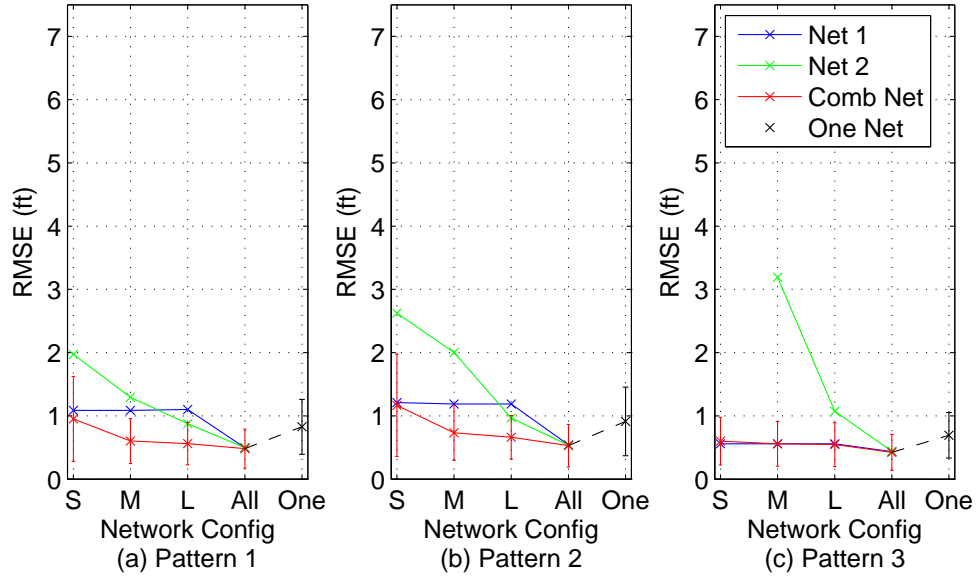
Figure 4.65: Average RMSE of simulated moving target for each pattern using Gaussian kernel estimation technique. $R_T = 1.3$ ft and $\sigma_n = 6$ dB.

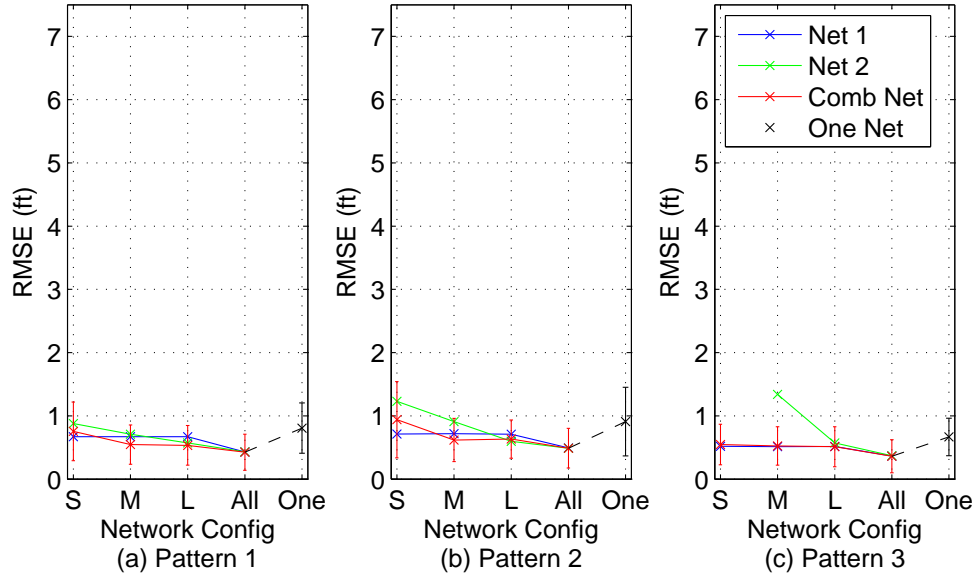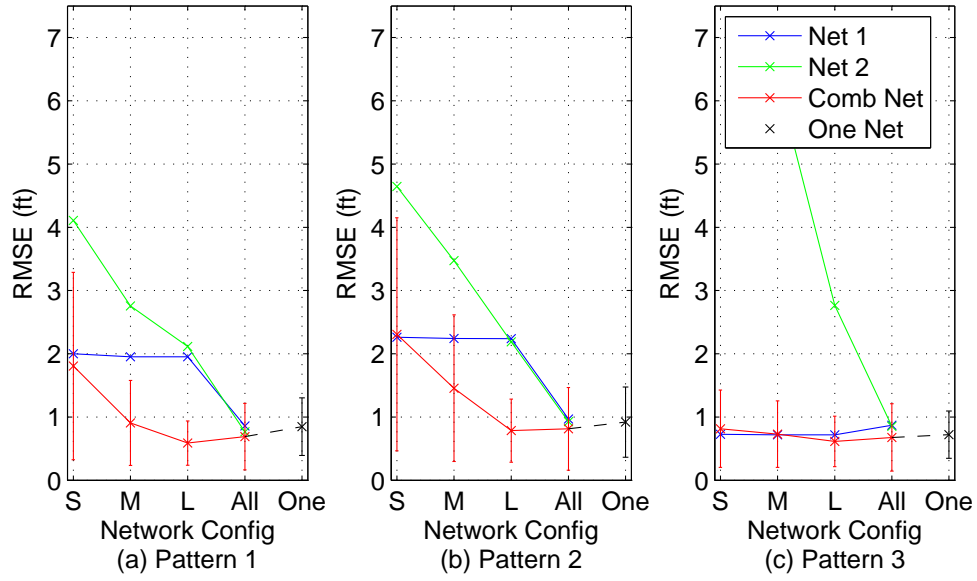### *4.3.3.2 Experimental.*

Fig. 4.66 shows the median PSNR of all experimental moving target data with respect to pattern. Fig. 4.67 shows the median SNR of all experimental moving target data with respect to pattern. For network configurations with two WSNs, the median PSNR is always higher in the combined network than each individual network. The *All* network configuration has the highest median PSNR, followed by a mix between the *One* and *Large* network configurations. However, the median PSNR is similar between each pattern for each network configuration. The median SNR is also fairly similar between each pattern and are all within 1 dB of each other, regardless of network configuration.

Fig. 4.68 shows the average RMSE using the maximum intensity value estimation technique, Fig. 4.69 shows the average RMSE using the 1-D projection estimation technique, and Fig. 4.70 shows the average RMSE using the Gaussian kernel estimation technique for experimental moving target data with respect to pattern. For Figs. 4.68–4.70, (a) is the average RMSE of all the experiments for Pattern 1, (b) is the average RMSE of all the experiments for Pattern 2, and (c) is the average RMSE of all the experiments for Pattern 3. The 1-D projection estimation technique provides the highest average RMSE out of the three position estimation techniques. The Gaussian estimation technique provides similar or slightly lower average RMSE results as the maximum intensity value estimation technique. Pattern 3 maintains a consistent average RMSE regardless of the network configuration.
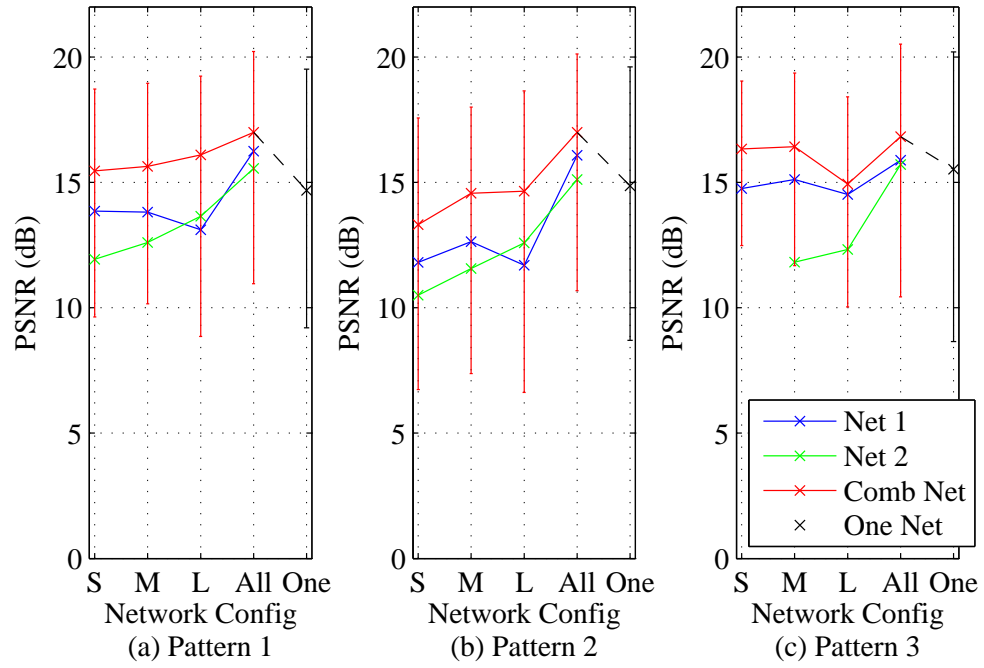
Figure 4.66: Median PSNR of experimental moving target for each network configuration.
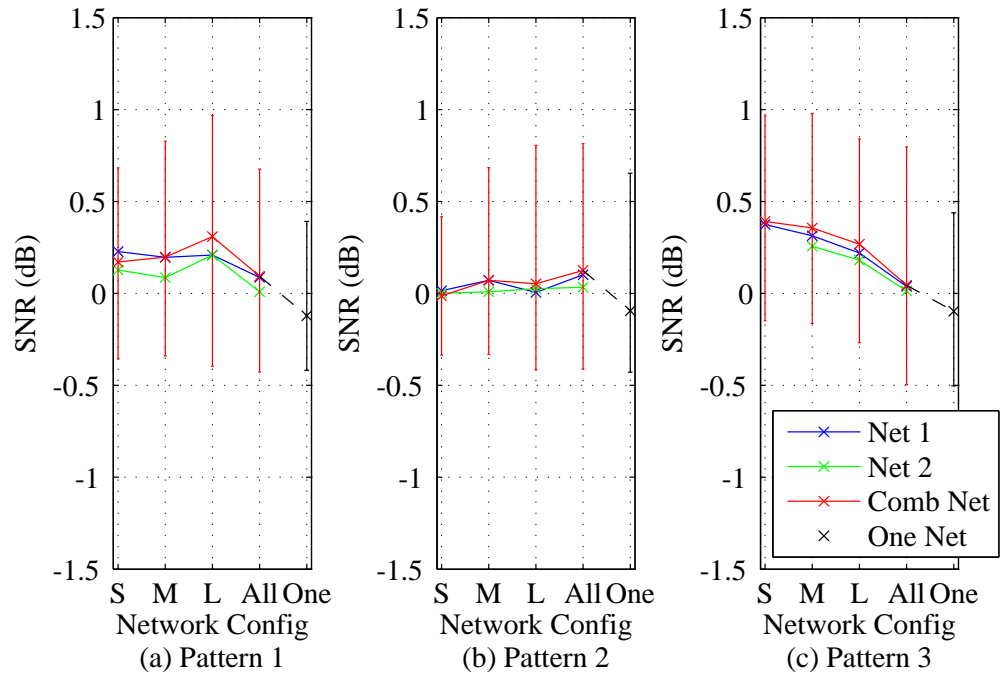
Figure 4.67: Median SNR of experimental moving target for each network configuration.

Figure 4.68: Average RMSE of experimental moving target for each network configuration using maximum intensity value estimation technique.

Figure 4.69: Average RMSE of experimental moving target for each network configuration using 1-D projection estimation technique.
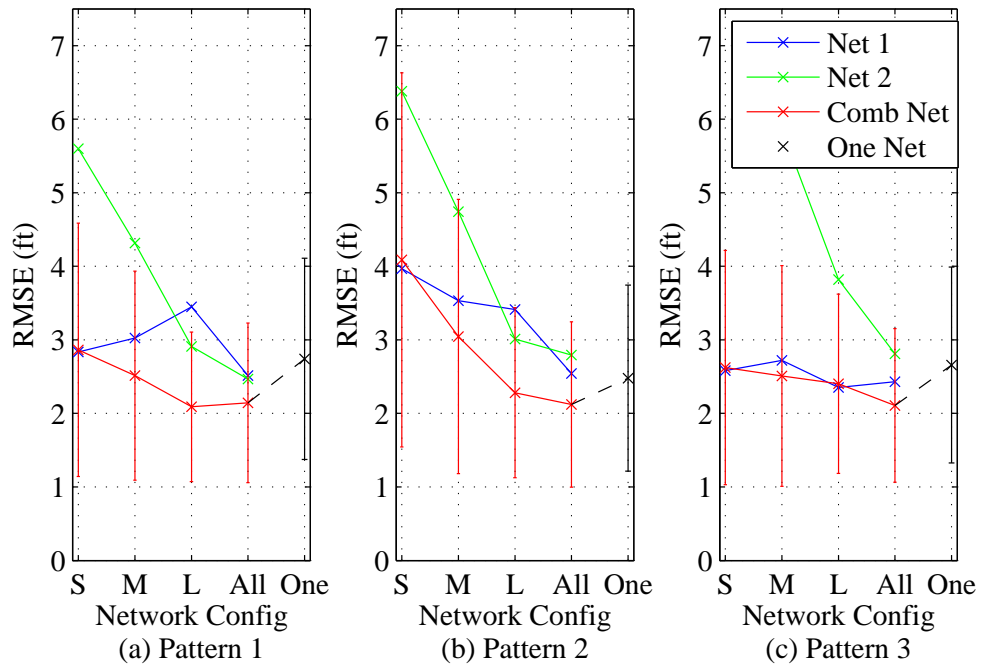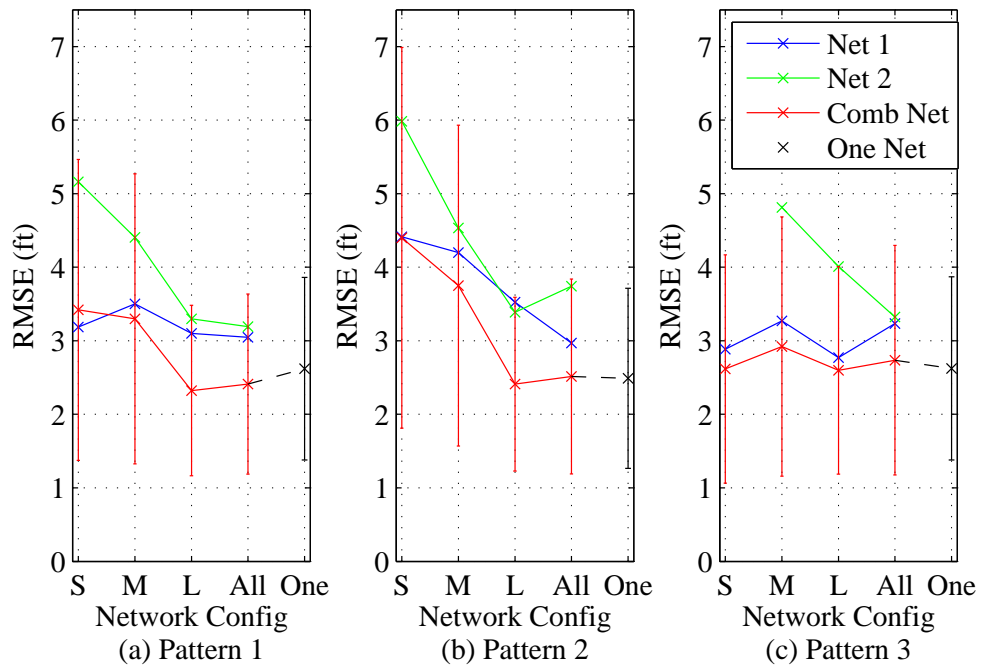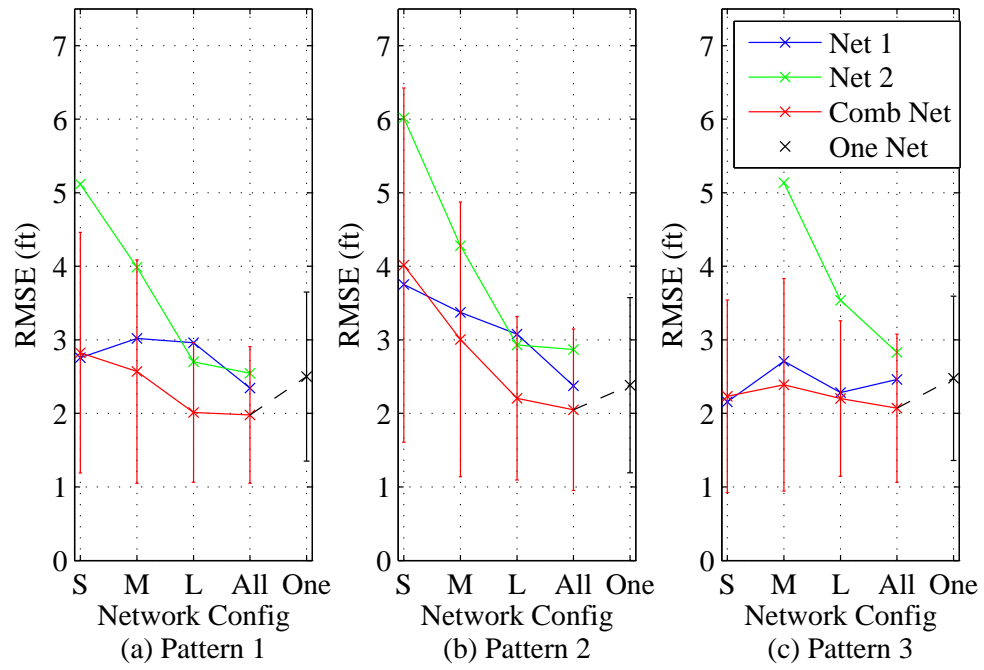
Figure 4.70: Average RMSE of experimental moving target for each network configuration using Gaussian kernel estimation technique.

4.3.4   Summary.

This section summarizes the image quality results for each network configuration.

4.3.4.1   PSNR/SNR.

PSNR generally provides results that are consistent with what is expected. The median PSNR generally increases as there is more overlap between two WSNs. This is expected since the greater the overlap, the more communication links there are crossing through the pixels of which the target is traversing through. The median PSNR also increases as the target moves slower. The results from SNR, however, are inconclusive. In simulations with $\sigma_n = 2$ dB, the median SNR increases as there is more overlap between two WSNs. However, the median SNR for simulations with $\sigma_n = 6$ dB and experimental results are inconsistent and fluctuates between each network configuration. The shadowing effects of a target depend on the size, shape, clothing, etc., of a target and using one standard truth attenuation image is probably not a good method to accurately compare estimated attenuation images with, although further research is required to say anything definitive.

4.3.4.2   Position Estimation Techniques.

Fig. 4.71 shows an example of position estimations for experiments where the target is walking at a slow pace for Pattern 2. Note that position estimates using the 1-D projection estimation technique in (b) display greater dispersion than the position estimates for maximum intensity value in (a) and Gaussian kernel in (c). Consistent with the results in all simulations and experiments, the 1-D projection estimation technique provides the highest error in comparison to the other position estimation techniques. The Gaussian kernel estimation technique generally provides the best estimation technique out of the three position estimation techniques. This is expected because the Gaussian kernel helps suppress the noise in an image, lowering random spikes in intensity within the attenuation image that might be mistaken as an obstruction. Fig. 4.72 shows a comparison between a

(a) Max Value

(b) 1-D Projection
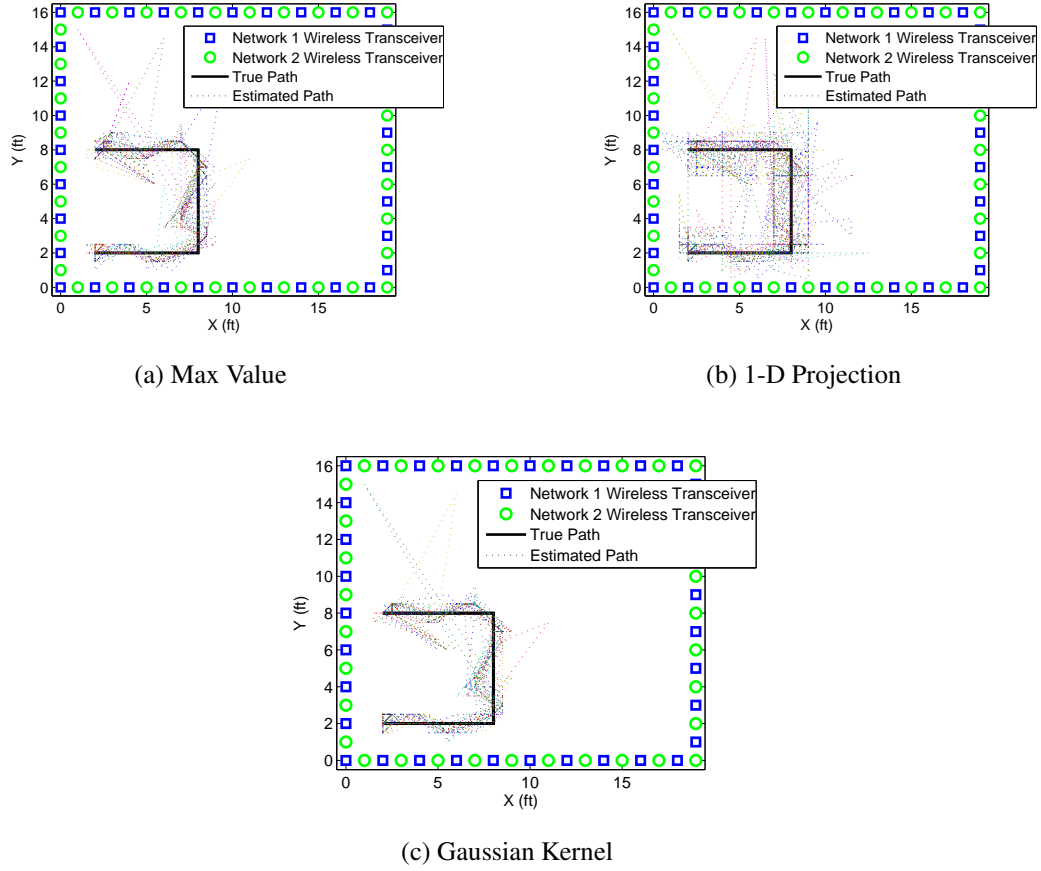
(c) Gaussian Kernel

Figure 4.71: Example of estimated positions for experimental moving target data with target walking in a slow pace for Pattern 2.

noisy attenuation image before and after the image has been filtered by the Gaussian kernel. Note that noisy spikes around the image have been smoothed and suppressed.

4.3.4.3   Network Configuration.

For any network configuration with two WSNs, the combined estimated attenuation image is almost always better than the attenuation image from each individual network. The only circumstances where one individual network performs better than the combined network is when the target rarely traverses through the area covered within the second

114

(a) Original Attenuation Image   (b) Gaussian Filtered Attenuation Image
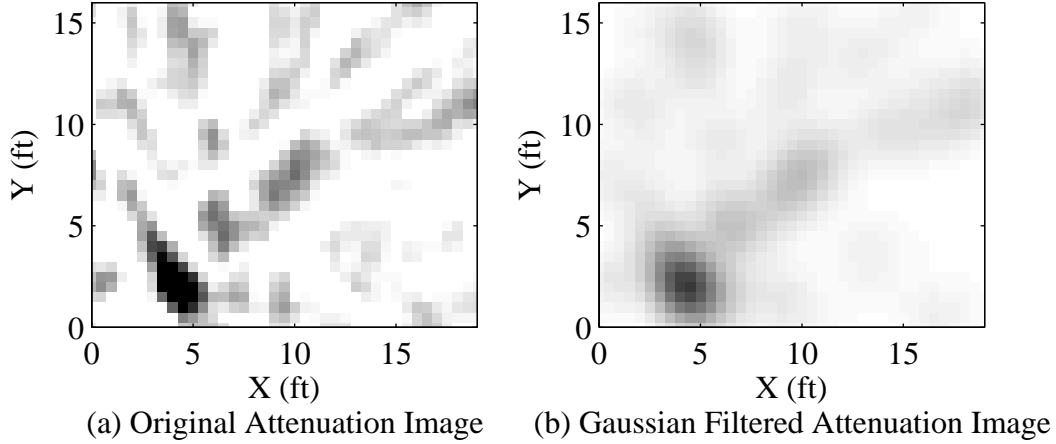
Figure 4.72: Attenuation images of an experimental moving target currently at (5,2) ft where (a) is the original attenuation image and (b) is the attenuation image after it has been filtered by the Gaussian kernel. The circle marks the true position of the target.

individual network. In this situation, the combined network provides a worse attenuation image because it is simply adding noise from the unused second individual network.

In simulations, noise does not have much of an effect on the outcome of the results when $R_T = 1.3$ ft. However, when $R_T = 1$ ft, noise has a much greater impact on the quality of the attenuation images. This is also expected because a smaller target will have less shadowing effects within the network and produce a smaller attenuation.

Stationary. For a stationary target, the *One* network configuration has the best image quality in terms of PSNR and RMSE, although the *All* and *Large* network configurations also yield very similar results. Since the target is not moving, this is expected since the *One* network configuration has the most number of links and, therefore, data to generate an attenuation image that is better than a network with less links. The *Large*, *All*, and *One* network configurations have an average RMSE of under 1 ft using the Gaussian estimation technique. The *Medium* network configuration has approximately a median PSNR of 2 dB lower than the *One* network configuration, but is also able to provide position estimates with an average RMSE of 1 ft.

115

Moving. For a moving target with respect to pattern or pace, the *All* network config-
uration generally provides the best image quality in terms of PSNR and RMSE, followed
by a mix between the *Large* network configuration and *One* network configuration. This is
due to the layout of the transceivers within the network configuration. For the *All* network
configuration, the transceivers surround the entire network area, allowing for a relatively
even distribution of links among the pixels within the area. The *Small*, *Medium*, and *Large*
network configurations have a high density of links along the edge of the network, but rel-
atively low density near the center of the two networks. The *Small* network configuration
has the lowest median PSNR and highest average RMSE. This is expected since the area
near the center of the *Small* network has very few links compared to the other network
configurations. The *Medium* network configuration, while does not perform as well at the
All network configuration, is still able to provide position estimations with no more than 1
extra ft average RMSE using the Gaussian estimation technique. The median PSNR for the
Medium network configuration is comparable with the *Large* network configuration, being
no more than 3 dB less than the *Large* network configuration and occasionally even having
higher PSNR values.

When comparing a moving target with respect to pace, the average RMSE generally
decreases and median PSNR increases as the target moves slower. This is expected since
the target covers less of an area while each transceiver transmits its RF signal for one frame
of data. The RMSE does increase as the target moves faster, but the difference on average
is less than 1.5 ft between the slow pace and the fast pace.

When comparing a moving target with respect to pattern, there is little difference
in image quality between each pattern. The median PSNR and RMSE are generally the
same for each pattern, regardless of the network configuration. Pattern 3 has slightly
a lower average RMSE than the other two patterns for the *Small* and *Medium* network

116

configurations. However, this is expected because the target does not traverse through the second individual network for Pattern 3 in the *Small* and *Medium* network configurations.

Fig. 4.73 and Fig. 4.74 show the median PSNR and median SNR from all simulated and experimental moving target data, respectively. In simulations, the *One* network configuration has the highest median PSNR. The *All* network configuration has the highest median PSNR for experimental data, although Fig. 4.74 shows that overall each network configuration has very similar median PSNR values. Fig. 4.75 and Fig. 4.76 show the average RMSE using each estimation technique from all simulated and experimental moving target data, respectively. The Gaussian estimation technique provides the lowest average RMSE out of the three position estimation techniques. Overall, the *All* network configuration provides the lowest average RMSE. However, the *Medium*, *Large*, *All*, and *One* network configurations all have an average RMSE within 1 ft of each other.
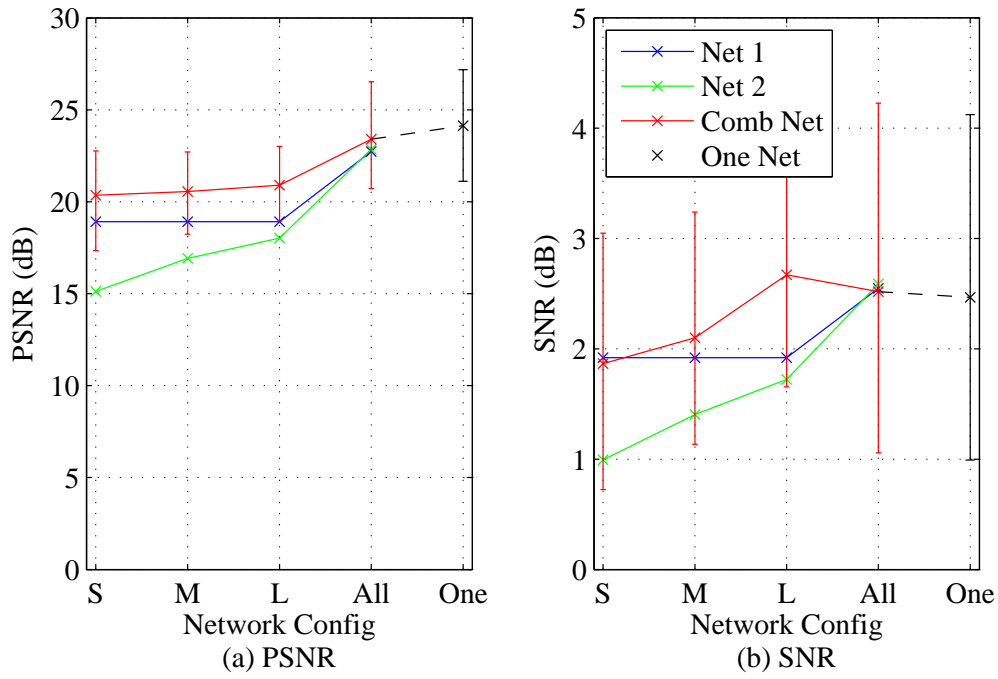
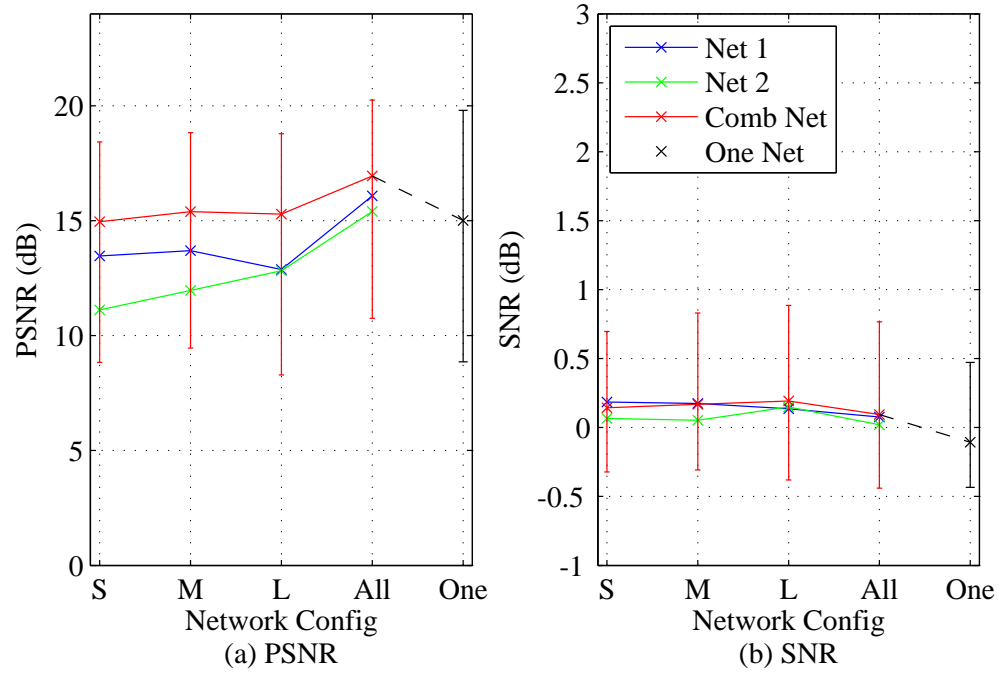Figure 4.73: Median PSNR and SNR of all simulated moving target for each network configuration.

Figure 4.74: Median PSNR and SNR of all experimental moving target for each network configuration.
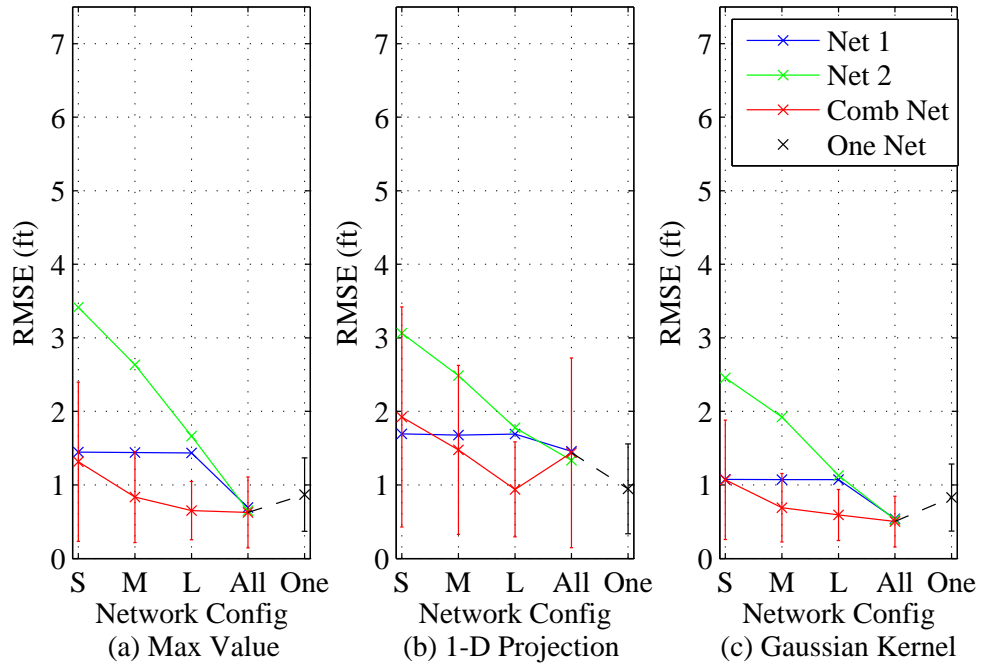
Figure 4.75: Average RMSE of all simulated moving target for each network configuration.
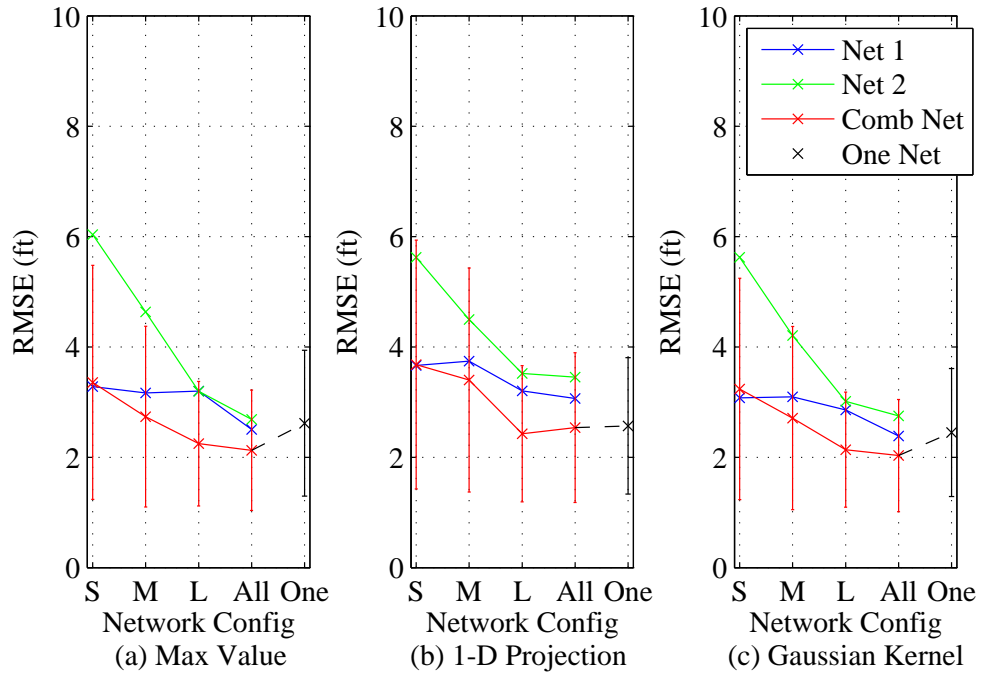
Figure 4.76: Average RMSE of all experimental moving target for each network configuration.

4.3.4.4   Higher Frame Rates.

While not thoroughly investigated in this research, the higher frame rates from having multiple WSNs compared to one WSN can also be used to improve image quality. Higher frame rates from a WSN allows for more data to be captured in the same amount of time. This higher rate may be required for real-time applications. However, higher frame rates can also help in situations when real-time applications are not required.

For example, suppose there is a situation that requires an update only every second. The traditional RTI network with one WSN presented in this research has an average frame rate of 0.86 frames per second. This is less than the one frame per second required. However, the RTI networks with two WSNs presented in this research have an average frame rate of 2.22 frames per second. Since the situation requires only updates every second, these RTI networks can stack multiple frames of RSS data together prior to computing an attenuation image. Results from stationary target data in Section 4.3.1 has shown the capabilities of reducing noise by stacking up to 60 frames of data together. These RTI networks may not be able to collect that many frames within a second, but Fig. 4.77 shows an example of experimental moving data where each frame of RSS data is rounded to the nearest second from which it is obtained. For every second, there are between 1 to 3 frames of RSS data that is averaged prior to generating an estimated attenuation image. The Gaussian kernel estimation technique is applied and target position is estimated. Note in Fig. 4.77 that averaging just 1 to 3 frames of data can help reduce and remove bad position estimates.

Figure 4.77: Comparison of standard position estimates and position estimates where all RSS data are rounded to the nearest second and averaged prior to generating an attenuation image.

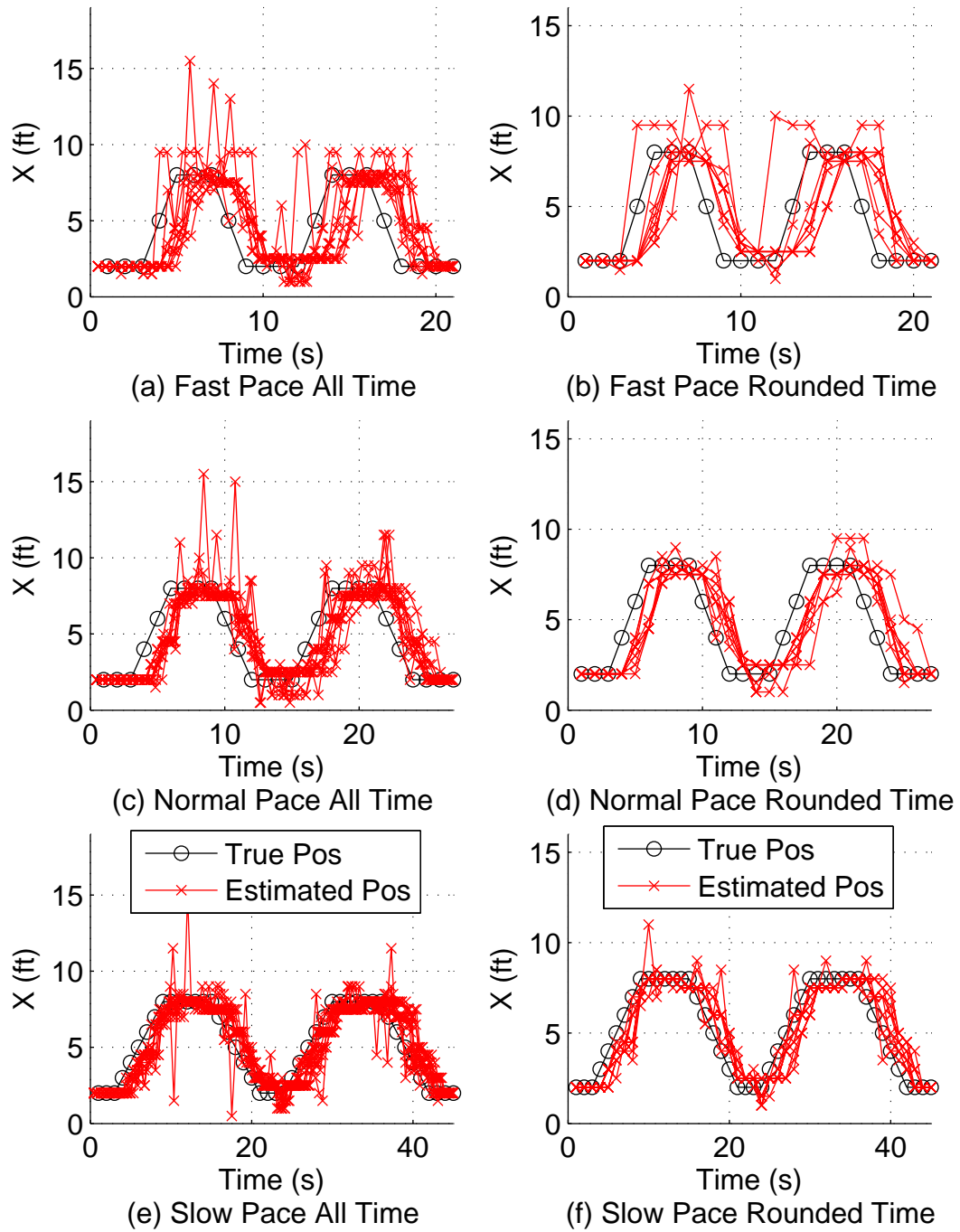# V.   Conclusion and Future Work

THIS chapter summarizes the research and presents the conclusion to this thesis. Recommendations for further research are also discussed.

5.1   Summary

RTI is a promising and emerging DFPL technology that has numerous potential applications in the areas of smart homes, health care, security, and emergency situations. The basic concept of RTI and how to utilize shadowing effects on RSS between transceivers in a WSN to map an attenuation image is discussed in Chapter II. Various measurement models, weight models, noise models, and regularization techniques have been proposed to create the most accurate attenuation image.

The goal of this research is to determine the applicability and characterize the capabilities of using multiple WSNs for RTI to address three major limitations with a large-scale RTI network. Using 70 wireless transceivers to cover an area no greater than 19 ft $\times$ 16 ft, Chapter III explains the metrics and methodology used to characterize and compare the traditional RTI network with one WSN to mnRTI that combines data from multiple WSNs. Five different network configurations are examined. 5000 simulations and 135 experiments are conducted for a stationary target. 4500 simulations and 405 experiments are conducted for a moving target. These simulations and experiments with real transceivers in different network configurations between one WSN and two WSNs are tested to compare with theoretical results. The three metrics used to compare the traditional RTI method with mnRTI are frame rate, computational complexity, and image quality.

Experimental results show that mnRTI with two WSNs and 35 transceivers in each network can provide an updated attenuation image on average of 2.22 frames per second. A traditional RTI network with one WSN and 70 transceivers provides an updated attenuation

image on average of 0.86 frames per second. This represents a 158% increase in attenuation image updates for mnRTI with two WSNs over the traditional RTI network. Using mnRTI with two WSNs is also computationally less complex than traditional RTI since there are less unique links to compute. Depending on the size and number of pixels within the network area, simulating two WSNs provide between 1.80 to 3.05 times less computational complexity than using one WSN. Using the same number of pixels, this represents a 44% reduction in computational complexity.

As for image quality, using SNR to compare image quality between each network configuration is inconclusive. The difference in SNR is small or inconsistent between each network. PSNR, however, is a good metric to quantify image quality. Higher PSNR corresponds with better position estimates and lower RMSE. In terms of position estimation techniques, the 1-D projection estimation technique yields the highest average RMSE in comparison to the other two position estimation techniques. The Gaussian kernel estimation technique helps smooth the attenuation image and suppress noisy spikes, providing the lowest average RMSE.

For a stationary target, the *One* network configuration always has the best median PSNR because the target is stationary and the network has the most links traversing through the target. However, the *Medium*, *Large*, and *All* network configurations generally produce similar position estimates as the *One* network configuration using the Gaussian estimation technique with an average of less than 0.5 ft RMSE for simulations and less than 1 ft RMSE for experiments. For a moving target, the highest median PSNR typically fluctuates between the *All* network configuration and *One* network configuration, depending on the pace, pattern, simulated target size, and noise level, although the difference is less than 3 dB. The *All* network configuration generally has the lowest average RMSE when using the Gaussian estimation technique compared to the other network configurations. However, the difference in average RMSE is less than 1 ft between the *Medium*, *Large*, *All*, and *One*

123

network configurations. With respect to pace, RMSE trends higher as the pace is faster. This is expected since the faster the pace, the more area a target covers within one frame of data. With respect to pattern, image quality is fairly consistent between each pattern. Overall, tests show that mnRTI can provide similar or better image quality than traditional RTI, as long as there is sufficient overlap between the two WSNs. The *Small* and *Medium* network configurations, which only has 2.5 ft and 4.5 ft of overlap between the two WSNs, respectively, have a median PSNR within 5 dB and average RMSE within 1 ft of the *Large*, *All*, and *One* network configurations.

The results from these preliminary experiments and simulations show that using multiple WSNs can provide higher frame rates, lower computational complexities, and similar or better image quality in terms of PSNR and position estimation accuracy. Also, even though the primary goal of this research is to address the limitations of a large-scale RTI network, the results in this research show that even small RTI networks can benefit from using multiple WSNs as opposed to the traditional RTI method.

5.2   Recommendations For Future Work

The experiments conducted in this research used two WSNs in a controlled lab environment with LOS transceivers. An attempt to apply this to a larger area can further validate and present limitations to mnRTI. Applying other advance techniques in RTI, such as KRTI [23], better transceivers, and cdRTI [16], will further explore the capabilities and limitations of using multiples WSNs and make it even more robust. Also, basic position estimation techniques are used in this research. Better algorithms and more sophisticated estimation techniques can be applied to provide even better position estimates. Advanced adaptive filters, such as the Kalman filter, can also be applied to detect and track multiple targets [34].

Even though the *All* network configuration, which increases the distance between each transceiver, generally provides the best image quality, there is a point when the distance

124

between each transceiver is too great and will not have enough unique communication links to accurately map each pixel within the network area. The number of transceivers in a WSN also affects the computational complexity and frame rate. Decreasing the number of transceivers and increasing the distance between each transceiver will increase the frame rate, lower the computational complexity, and allow for a bigger coverage area. However, lesser communication links also equate to lesser information of the area and potentially a decrease in localization accuracy. Further research to determine the maximum distance between transceivers and minimum number of transceivers in a WSN to still be able to produce an accurate attenuation image will be important parameters in creating an optimal WSN.

Finally, this research demonstrated the capabilities of using two WSNs, although the concept also applies to more than two WSNs. Testing mnRTI with more than two WSNs can further demonstrate the capabilities of mnRTI. This will become especially important for very large-scale RTI applications, such as border patrol or base surveillance.

Bibliography

[1] R. S. Bhuvaneswaran, J. L. Bordim, J. Cui, N. Ishii, and K. Nakano, "An Energy-Efficient Initialization Protocol for Wireless Sensor Networks," in *International Conference on Parallel Processing Workshops*, Valencia, Sept. 2001, pp. 423–428.

[2] S. Savazzi, M. Nicoli, F. Carminati, and M. Riva, "A Bayesian Approach to Device-Free Localization: Modeling and Experimental Assessment," *IEEE Journal of Selected Topics in Signal Processing*, vol. 8, no. 1, pp. 16–29, Feb. 2014.

[3] M. Youssef, M. Mah, and A. Agrawala, "Challenges: Device-Free Passive Localization for Wireless Environments," in *Proceedings of the 13th Annual ACM International Conference on Mobile Computing and Networking*, Montreal, Quebec, Sept. 2007, pp. 222–229.

[4] J. Wilson and N. Patwari, "Radio Tomographic Imaging with Wireless Networks," *IEEE Transactions on Mobile Computing*, vol. 9, no. 5, pp. 621–632, May 2010.

[5] C. R. Anderson, R. K. Martin, T. O. Walker, and R. W. Thomas, "Radio Tomography for Roadside Surveillance," *IEEE Journal of Selected Topics in Signal Processing: Special Issue on Non-Cooperative Localization Networks*, vol. 8, no. 1, Feb. 2014.

[6] R. K. Martin, C. Anderson, R. W. Thomas, and A. S. King, "Modelling and Analysis of Radio Tomography," in *2011 Fourth IEEE Int'l Workshop on Computational Advances in Multi-Sensor Adaptive Processing (CAMSAP)*, San Juan, Puerto Rico, Dec. 2011, pp. 377–380.

[7] R. K. Martin, A. Folkerts, and T. Heinl, "Accuracy vs. Resolution in Radio Tomography," *IEEE Transactions on Signal Processing*, vol. 62, no. 10, pp. 2480–2491, May 2014.

[8] K. Woyach, D. Puccinelli, and M. Haenggi, "Sensorless Sensing in Wireless Networks: Implementation and Measurements," in *2006 4th International Symposium on Modeling and Optimization in Mobile, Ad Hoc and Wireless Networks*, Apr. 2006, pp. 1–8.

[9] O. Kaltiokallio, M. Bocca, and N. Patwari, "Follow @grandma: Long-Term Device-Free Localization for Residential Monitoring," in *IEEE Proc. Thiry-Seventh Conf. on Local Computer Networks Workshops (LCN Workshops)*, Oct. 2012, pp. 991–998.

[10] B. Mager, N. Patwari, and M. Bocca, "Fall Detection using RF Sensor Networks," in *2013 IEEE 24th International Symposium on Personal Indoor and Mobile Radio Communications (PIMRC)*, Sept. 2013, pp. 3472–3476.

[11] N. Patwari, L. Brewer, Q. Tate, O. Kaltiokallio, and M. Bocca, "Breathfinding: A Wireless Network That Monitors and Locates Breathing in a Home," *IEEE Journal of Selected Topics in Signal Processing*, vol. 8, no. 1, pp. 30–42, Feb. 2014.

[12] M. E. Brak and M. Essaaidi, "Wireless Sensor Network in Home Automation Network and Smart Grid," in *2012 International Conference on Complex Systems*, Agadir, Morocco, Nov. 2012, pp. 1–6.

[13] D. Maas, J. Wilson, and N. Patwari, "Toward a Rapidly Deployable RTI System for Tactical Operations," in *2013 IEEE 38th Conference on Local Computer Networks Workshops (LCN Workshops)*, Sydney, Australia, Oct. 2013, pp. 203–210.

[14] R. K. Martin, J. Nishida, and T. Van, "Complexity Reduction in Large Scale Radio Tomography Networks," *Submitted to IEEE Transactions on Computational Imaging*, Dec. 2014.

[15] D. Zhang, J. Ma, Q. Chen, and L. M. Ni, "An RF-Based System for Tracking Transceiver-Free Objects," in *Proc. Fifth Annual IEEE Int'l Conf. on Pervasive Computing and Communications (PerCom)*, Mar. 2007, pp. 135–144.

[16] O. Kaltiokallio, M. Bocca, and N. Patwari, "Enhancing the Accuracy of Radio Tomographic Imaging Using Channel Diversity," in *IEEE 9th International Conference on Mobile Adhoc and Sensor Systems (MASS)*, Oct. 2012, pp. 254–262.

[17] O. Katircioglu, H. Isel, O. Ceylan, F. Taraktas, and H. B. Yagci, "Comparing Ray Tracing, Free Space Path Loss and Logarithmic Distance Path Loss Models in Success of Indoor Localization with RSSI," in *19th Telecommunications Forum (TELFOR)*, Nov. 2011, pp. 313–316.

[18] B. Sklar, *Digital Communications: Fundamentals and Applications*, Prentice-Hall, Upper Saddle River, NJ, 2nd edition, 2001.

[19] M. Kieffer and E. Walter, "Centralized and Distributed Source Localization by a Network of Sensors Using Guaranteed Set Estimation," in *2006 IEEE International Conference on Acoustics, Speech and Signal Processing*, Toulouse, France, May 2006, vol. 4, pp. 977–980.

[20] A. J. Weiss, "On the Accuracy of a Cellular Location System Based on RSS Measurements," *IEEE Transactions on Vehicular Technology*, vol. 52, no. 6, pp. 1508–1518, Nov. 2003.

[21] J. Wilson, N. Patwari, and F. G. Vasquez, "Regularization Methods for Radio Tomographic Imaging," in *Proc. Virginia Tech Symposium on Wireless Personal Communications*, June 2009.

[22] J. Wilson and N. Patwari, "See-Through Walls: Motion Tracking Using Variance-Based Radio Tomography Networks," *IEEE Transactions on Mobile Computing*, vol. 10, no. 5, pp. 612–621, May 2011.

[23] Y. Zhao, N. Patwari, J. M. Phillips, and S. Venkatasubramanian, "Radio Tomographic Imaging and Tracking of Stationary and Moving People via Kernel Distance," in *2013 ACM/IEEE International Conference on Information Processing in Sensor Networks (IPSN)*, Apr. 2013, pp. 229–240.

[24] Y. Zhao and N. Patwari, "Robust Estimators for Variance-Based Device-Free Localization and Tracking," *IEEE Transactions on Mobile Computing*, vol. PP, no. 99, Dec. 2014.

[25] L. Heng, W. Zheng-huan, B. Xiang-yuan, and A. Jian-ping, "Image Reconstruction Algorithms for Radio Tomographic Imaging," in *2012 IEEE International Conference on Cyber Technology in Automation, Control, and Intelligent Systems*, Bangkok, Thailand, May 2012, pp. 48–53.

[26] B. Wei, A. Varshney, W. Hu, N. Patwari, T. Voigt, and C. T. Chou, "dRTI: Directional Radio Tomographic Imaging," *Computing Research Repository*, Feb. 2014.

[27] V. Koster, A. Lewandowski, and C. Wietfeld, "A Segmentation-Based Radio Tomographic Imaging Approach for Interference Reduction in Hostile Industrial Environments," in *2012 IEEE/ION Position Location and Navigation Symposium (PLANS)*, Apr. 2012, pp. 1074–1081.

[28] M. Khaledi, S. K. Kasera, N. Patwari, and M. Bocca, "Energy Efficient Radio Tomographic Imaging," in *2014 Eleventh Annual IEEE International Conference on Sensing, Communication, and Networking (SECON)*, June 2014, pp. 609–617.

[29] T. S. Danella, "Identifying High-Traffic Patterns in the Workplace with Radio Tomographic Imaging in 3D Wireless Sensor Networks," M.S. thesis, Air Force Institute of Technology, Mar. 2014.

[30] M. A. Kanso and M. G. Rabbat, "Compressed RF Tomography for Wireless Sensor Networks: Centralized and Decentralized Approaches," in *IEEE Proc. Fifth Int'l Conf. on Distributed Computing in Sensor Systems (DCOSS)*, pp. 173–186. Springer, 2009.

[31] M. Kanso and M. G. Rabbat, "Efficient Detection and Localization of Assets in Emergency Situations," *Proc. Thirty-Seventh Int'l Sym. Medical Info. Commun. Tech.*, vol. 1, pp. 1–5, 2009.

[32] Y. Li, X. Chen, M. Coates, and B. Yang, "Sequential Monte Carlo Radio-Frequency Tomographic Tracking," in *2011 IEEE International Conference on Acoustics, Speech and Signal Processing (ICASSP)*, May 2011, pp. 3976–3979.

[33] B. R. Hamilton, X. Ma, B. J. Baxley, and S. M. Matechik, "Propagation Modeling for Radio Frequency Tomography in Wireless Networks," *IEEE Journal of Selected Topics in Signal Processing: Special Issue on Non-Cooperative Localization Networks*, vol. 8, no. 1, pp. 55–65, Feb. 2014.

[34] M. Bocca, O. Kaltiokallio, N. Patwari, and S. Venkatasubramanian, "Multiple Target Tracking with RF Sensor Networks," *IEEE Transactions on Mobile Computing*, vol. 13, no. 8, pp. 1787–1800, Aug. 2014.

[35] C. Alippi, M. Bocca, G. Boracchi, N. Patwari, and M. Roveri, "RTI Goes Wild: Radio Tomographic Imaging for Outdoor People Detection and Localization," *Computing Research Repository*, July 2014.

[36] M. Bocca, A. Luong, N. Patwari, and T. Schmid, "Dial It In: Rotating RF Sensors to Enhance Radio Tomography," in *2014 Eleventh Annual IEEE International Conference on Sensing, Communication, and Networking (SECON)*, June 2014, pp. 600–608.

[37] S. Miller and D. Childers, *Probability and Random Processes*, Academic Press, Boston, MA, 2nd edition, 2012.

[38] S. Nannuru, L. Yunpeng, Y. Zeng, M. Coates, and B. Yang, "Radio-Frequency Tomography for Passive Indoor Multitarget Tracking," *IEEE Transactions on Mobile Computing*, vol. 12, no. 12, pp. 2322–2333, Dec. 2013.

[39] B. R. Hamilton, X. Ma, R. J. Baxley, and S. M. Matechik, "Radio frequency tomography in mobile networks," in *2012 IEEE Statistical Signal Processing Workshop (SSP)*, Ann Arbor, MI, Aug. 2012, pp. 508–511.

[40] G. Demoment, "Image Reconstruction and Restoration: Overview of Common Estimation Structures and Problems," *IEEE Transactions on Acoustics, Speech and Signal Processing*, vol. 37, no. 12, pp. 2024–2036, Dec. 1989.

[41] M. Bocca, O. Kaltiokallio, and N. Patwari, "Radio Tomographic Imaging for Ambient Assisted Living," in *Evaluating AAL Systems Through Competitive Benchmarking*, pp. 108–130. 2013.

[42] R. C. Aster, B. Borchers, and C. H. Thurber, *Parameter Estimation and Inverse Problems*, Academic Press, 2013.

[43] N. Patwari and J. Wilson, "RF Sensor Networks for Device-Free Localization: Measurements, Models, and Algorithms," *Proceedings of the IEEE*, vol. 98, no. 11, pp. 1961–1973, Nov. 2010.

[44] W Yuanji, L. Jianhua, L. Yi, F. Yao, and J. Qinzhong, "Image Quality Evaluation Based on Image Weighted Separating Block Peak Signal to Noise Ratio," in *Proceedings of the 2003 International Conference on Neural Networks and Signal Processing*, Nanjing, Dec. 2003, vol. 2, pp. 994–997.

[45] J. Korhonen and J. You, "Peak Signal-to-Noise Ratio Revisited: Is Simple Beautiful?," in *2012 Fourth International Workshop on Quality of Multimedia Experience (QoMEX)*, Yarra Valley, VIC, July 2012, pp. 37–38.

[46] J.-C. Yoo and C. W. Ahn, "Image Matching Using Peak Signal-to-Noise Ratio-Based Occlusion Detection," *IET Image Processing*, vol. 6, no. 5, pp. 483–495, July 2012.

[47] S. C. Cain, M. M. Hayat, and E. E. Armstrong, "Projection-Based Image Registration in the Presence of Fixed-Pattern Noise," *IEEE Transactions on Image Processing*, vol. 10, no. 12, pp. 1860–1872, Dec. 2001.

[48] M. D. Sambora and R. K. Martin, "Improving the Performance of Projection-Based Image Registration," in *2008 IEEE Aerospace Conference*, Big Sky, MT, Mar. 2008, pp. 1–8.

[49] R. C. Gonzalez and R. E. Woods, *Digital Image Processing*, Prentice-Hall, Inc., Upper Saddle River, NJ, 3rd edition, 2006.

[50] Crossbow Technologies, "TelosB Mote Platform Datasheet," Webpage, https://www.willow.co.uk/TelosB_Datasheet.pdf, 2013.

[51] Texas Instruments, "CC2420 Inverted F Antenna Design Note DN0007," Webpage, http://www.ti.com/lit/an/swru120b/swru120b.pdf, 2008.

[52] H. Lee and I. Moon, "A study on IEEE 802.15.4 Based Factory Automation System in Wireless Network," in *11th International Conference on Advanced Communication Technology*, Feb. 2009, vol. 1, pp. 851–854.

[53] N. T. Le, S. W. Choi, and Y. M. Jang, "Approximate Queuing Analysis for IEEE 802.15.4 Sensor Network," in *2010 Second International Conference on Ubiquitous and Future Networks (ICUFN)*, June 2010, pp. 193–198.

[54] Stanford Research Community, "TinyOS Home Page," Webpage, http://www.tinyos.net, 2007-2013.

[55] Neal Patwari; University of Utah, "SPAN Home Page," Webpage, http://span.ece.utah.edu, 2013.

130

REPORT DOCUMENTATION PAGE

Form Approved
OMB No. 0704–0188

1. REPORT DATE *(DD–MM–YYYY)*	2. REPORT TYPE	3. DATES COVERED *(From — To)*
26–03–2015	Master's Thesis	Oct 2013–Mar 2015

4. TITLE AND SUBTITLE

Characterizing Multiple Wireless Sensor Networks for Large-Scale Radio Tomography

5a. CONTRACT NUMBER

5b. GRANT NUMBER

5c. PROGRAM ELEMENT NUMBER

6. AUTHOR(S)

Van, Tan, Captain, USAF

5d. PROJECT NUMBER

15G451I

5e. TASK NUMBER

5f. WORK UNIT NUMBER

7. PERFORMING ORGANIZATION NAME(S) AND ADDRESS(ES)

Air Force Institute of Technology
Graduate School of Engineering and Management (AFIT/EN)
2950 Hobson Way
WPAFB, OH 45433-7765

8. PERFORMING ORGANIZATION REPORT NUMBER

AFIT-ENG-MS-15-M-057

9. SPONSORING / MONITORING AGENCY NAME(S) AND ADDRESS(ES)

AFOSR (Attn: Dr. Tristan Nguyen, AFOSR/RTC)
Comm. Phone: (703) 696-7796 / DSN: 426-7796 / Fax: (703) 696-7360
Email: tristan.nguyen@afosr.af.mil
875 North Randolph Street, Suite 325, Room 3112, Arlington, VA 22203-1768

10. SPONSOR/MONITOR'S ACRONYM(S)

Air Force Office of Scientific Research (AFOSR)/RTC

11. SPONSOR/MONITOR'S REPORT NUMBER(S)

12. DISTRIBUTION / AVAILABILITY STATEMENT

DISTRIBUTION STATEMENT A:
APPROVED FOR PUBLIC RELEASE; DISTRIBUTION UNLIMITED

13. SUPPLEMENTARY NOTES

This work is declared a work of the U.S. Government and is not subject to copyright protection in the United States.

14. ABSTRACT

Radio Tomographic Imaging (RTI) is an emerging Device-Free Passive Localization (DFPL) technology that uses a collection of cheap wireless transceivers to form a Wireless Sensor Network (WSN). Unlike device-based active localization, DFPL does not require a target of interest to be wearing any kind of device. The basic concept of RTI utilizes the changes in Received Signal Strength (RSS) between the links of each transceiver to create an attenuation image of the area. This image can then be used for target detection, tracking, and localization. Each transceiver in the WSN must transmit sequentially to prevent collisions. This is not a problem when the number of transceivers in the WSN are small. However, large-scale RTI with a large number of transceivers suffer from high computational complexity, low frame rates, and physical distance limitations on the range of the transceivers.

The goal of this research is to determine the applicability and characterize the feasibility of using multiple WSNs to address the limitations with a large-scale RTI network. The concept to this new variant of RTI, called Multiple-Networks RTI (mnRTI), is to divide the transceivers into multiple WSNs as opposed to using one WSN. Analytical, simulated, and experimental data are computed, collected, and compared between a RTI network with one WSN to a mnRTI network with two WSNs. The WSN(s) comprise a total of 70 wireless transceivers covering an area of no more than 19 ft × 16 ft. Simulated and experimental results are presented from a series of stationary and moving target data collection. Preliminary results demonstrate multiple WSNs can potentially provide similar or better results than the traditional RTI method with one WSN. Multiple WSNs have higher frame rates and lower computational complexity. Also, position estimation accuracy are comparable, if not better, than the traditional RTI method with one WSN.

15. SUBJECT TERMS

Radio Tomographic Imaging, RTI, multiple wireless sensor networks, WSN, device free localization, RSS, RF, passive

16. SECURITY CLASSIFICATION OF:

a. REPORT	b. ABSTRACT	c. THIS PAGE
U	U	U

17. LIMITATION OF ABSTRACT

UU

18. NUMBER OF PAGES

153

19a. NAME OF RESPONSIBLE PERSON

Dr. Richard K. Martin (ENG)

19b. TELEPHONE NUMBER *(include area code)*
(937) 255-3636 x4625 richard.martin@afit.edu

Standard Form 298 (Rev. 8–98)
Prescribed by ANSI Std. Z39.18